Observatoire de Paris

École Doctorale 127 A&A
Astronomie et Astrophysique d'Ile de France

Habilitation à diriger des recherches

Discipline : Astrophysique

présentée par

Olga Alexandrova

Solar Wind Turbulence: *in-situ* observations from magneto-fluid to kinetic plasma scales

---

Soutenance prévue le 28 septembre 2020 devant le jury composé de :

M. Marco Velli	Professor, UCLA
M. Thierry Passot	CNRS, Observatoire de la Côte d'Azur
M. Sébastien Galtier	Professor, Université Paris-Saclay
M. Roland Grappin	Astronome, LPP
Mme. Édith Falgarone	CNRS, ENS de Paris
M. Vincenzo Carbone	Professor, Università della Calabria
M. David Burgess	Professor, Queen Mary University of London

après avis des rapporteurs :

M. Marco Velli	Professor, UCLA
M. Thierry Passot	CNRS, Observatoire de la Côte d'Azur
M. Sébastien Galtier	Professor, Université Paris-Saclay

Laboratoire d'Études Spatiales et d'Instrumentation en Astrophysique, Observatoire de Paris, 5 Place Jules Janssen 92195 Meudon Cedex

Observatoire de Paris
École doctorale 127 A&A
5 Place Jules Janssen
92195 Meudon Cedex

Solar Wind Turbulence: *in-situ* observations from magneto-fluid to kinetic plasma scales

Olga Alexandrova

September 1, 2020

Contents

Chapter 1

Introduction

1 Space plasma

Natural plasmas are frequently in a turbulent state characterized by large and irregular fluctuations of the physical parameters. The spatial and temporal scales of these fluctuations cover a large range, usually extending down to the smallest scales resolved by the observations. Plasma turbulence appears to be present throughout the universe, like, e.g., in galaxy clusters, accretion disks, supernova remnants, the interstellar medium, stars, stellar winds and planetary magnetospheres.

The Heliosphere with the solar wind and planetary magnetospheres represent excellent laboratories for the observations of collisionless astrophysical plasmas and in particular of plasma turbulence. Instruments on board more and more sophisticated spacecraft can obtain high quality *in situ* measurements of electromagnetic fields and of particle distribution functions with their moments (density, velocity, temperature, etc.), in a wide range of scales and frequencies, and under different plasma and boundary conditions.

In particular, since the beginning of the exploration of the interplanetary space in the sixties, it has been observed that the solar wind plasma flow is far from being laminar and exhibits large magnetic and velocity fluctuations at all accessible scales, qualitatively similar to what is observed in high Reynolds number neutral flows. This apparently fluid behavior is puzzling in a very rarified plasma such as the solar wind. Indeed, at the Earth's orbit, the solar wind density is of the order of 5 particles per cm^3 and the mean free path ℓ_{mfp} of the order of 1 AU. Thus, one may expect that the fluid approximation may not be valid (for scales smaller than 1 AU).

In agreement with the very low degree of collisionality, the solar wind particle distribution functions are far from being isotropic Maxwellians. The distribution functions of ions (mostly protons, and 5% of α particles) and of electrons are not isotropic with respect to the mean magnetic field $\mathbf{B}_0$ direction, i.e, their temperatures in the plane perpendicular to the mean field $T_\perp$ is different from the parallel temperature $T_\parallel$[1]. When

---

[1] All over the manuscript, symbols $\perp$ and $\parallel$ mean perpendicular and parallel to the mean magnetic field $\mathbf{B}_0$.

the ion (electron) distribution functions have a strong anisotropy, electromagnetic waves at ion (electron) scales are generated, bringing the plasma to a marginal stability state. In addition to the temperature anisotropy, the distribution function of parallel electron velocities $f(V_{e,\parallel})$ is not symmetric but has an important skewness: there exists a broad electron beam coming from the Sun (called Strahl), that results in an outward electron heat flux.

All these features can throw a doubt on the fact that the solar wind plasma can behave as a fluid. Nevertheless, the presence of turbulence at scales ℓ smaller than the mean collisional scale ℓ_{mfp} and also of magnetohydrodynamic (MHD) discontinuities, like shocks in front of the planetary magnetospheres and of Coronal Mass Ejections, are signatures that space plasmas behave like a fluid (or, to be more precise, like a *magneto-fluid*) at scales $\ell < \ell_{\mathrm{mfp}}$. Fluid behavior ceases in the vicinity of ion and electron characteristic scales, the so-called *kinetic plasma scales*. This manuscript is devoted to the space plasma turbulence covering fluid and kinetic scales.

2 Fluid turbulence in brief

Turbulence is a non-resolved problem of classical mechanics. In the case when convection dominates viscosity, an external source of energy produces turbulence in a fluid. In other words, this happens when the energy injection scale L is much larger than the dissipation scale ℓ_d. The ratio between convective and dissipative terms at the injection scale L defines the Reynolds number $R_e = LV_L/\nu$ (where V_L is the typical value of velocity fluctuations at scale L and ν the kinematic viscosity). Turbulence is well developed in a fluid when $R_e \gg 1$.

Thanks to a number of observations, numerical simulations and theoretical works, the following universal properties of a turbulent system have been firmly established:

- In Fourier space, at intermediate scales $L^{-1} \ll k \ll \ell_d^{-1}$ (k being a wave-number), within the so-called *inertial range*, the power spectrum of the velocity fluctuations is observed to follow a $k^{-5/3}$ law, independently of how energy is injected in the system, and of how it is dissipated at small scales. This suggests scale invariance: at each scale the same physical description is valid (the Navier-Stokes equation for fluids and the MHD equations for magnetised plasmas are scale invariant and describe well self-similar turbulent fluctuations).

- Intermittency, due to spatial non-uniformity of the energy transfer across scales, manifests itself as a scale dependent departure from Gaussian distributions of the probability distribution functions (PDF's) of the turbulent fluctuations.

To date, three-dimensional fluid turbulence is far from being understood, and there is no satisfactory theory that fully describes it in a sufficiently general frame: we still don't know how to arrive from the fundamental Navier-Stokes equation (with or without magnetic field) to the statistical description which admits solutions in the form of the observed stationary spectra independent of the energy injection and its dissipation.

Therefore one has to rely on "phenomenologies" which attempt to provide a framework for the interpretation of experimental results. For example the empirical $k^{-5/3}$ law is well described by the Kolomogorov's phenomenology (hereafter K41) (Kolmogorov, 1941; Frisch, 1995). In this simple model of incompressible turbulence, kinetic energy E_c is supposed to cascade from large scales to small scales and the *cascade rate ε* (energy per unit time) is constant over the inertial range $\varepsilon = \partial E_c / \partial t = const$. Since the only timescale that appears in the system is the time of the energy exchange between the fluctuations (the *eddies*), also called the *non-linear time* or *eddie turnover time* $\tau_{NL} = \ell/\delta v$, the cascade rate for incompressible velocity field fluctuations δv can be approximated by $\varepsilon \sim (\delta v)^2 / \tau_{NL} = const$. It follows that the fluctuations verify the following scaling $\delta v \sim (\varepsilon \ell)^{1/3}$, so that the power spectrum $\delta v^2 / k$ goes like $\ell^{5/3}$ or $k^{-5/3}$.

Intermittency is beyond the K41 phenomenology. It has been observed that in neutral fluids it appears in the form of coherent structures as filaments of vorticity (She et al., 1990). Their characteristic length can be of the order of the energy injection scale L but their cross-section is of the order of the dissipation scale ℓ_d (see the references of Section 8.9 in Frisch (1995)). Thus, in Fourier space, these filaments occupy all scales including the edges of the inertial range.

As we have said, in the phenomenological framework of turbulence, the majority of the results are based on the interpretation of experimental results. However, one important theoretical result was obtained from the first principles, independently of K41 phenomenology: it is known as Kolmogorov's 4/5 law (hereafter K4/5). The K4/5 law prescribes that, for fully developed incompressible Navier-Stokes turbulence in condition of isotropy, local homogeneity, and vanishing dissipation (i.e., in the inertial range), the third moment of the longitudinal (i.e., along the bulk flow) velocity fluctuations δv scales linearly with the separation ℓ:

$$Y(\ell) = \langle \delta v^3 \rangle = -\frac{4}{5} \varepsilon \ell, \tag{1.1}$$

see (Frisch, 1995), Section 6.2, and references therein. This law has been indeed observed in neutral fluid turbulence (e.g., Danaila et al., 2001).

At scales around ℓ_d (*dissipation range*), the viscosity converts turbulent energy into heat. The fluctuations are not self-similar anymore and the spectrum does not follow a power-law but has an exponential cut-off $\sim k^3 \exp(-Ck\ell_d)$, with $C \simeq 7$, see (Chen et al., 1993). The dissipation range is described in fluid approximation: ℓ_d is much larger than the collisional mean free path.

The dissipation scale ℓ_d, also called the Kolmogorov micro-scale, is defined as the scale where the Reynolds number is one, where the dissipation and convection are equally important. It can be expressed as a function of the kinematic viscosity ν and the energy dissipation rate ε_d:

$$\ell_d = \left(\frac{\nu^3}{\varepsilon_d} \right)^{\frac{1}{4}}. \tag{1.2}$$

For a stationary turbulence system, the energy dissipation rate ε_d is the same as the energy injection and energy transfert rates ε. As one can see from Equation (1.2), the stronger the energy dissipation rate (and so the injection rate), the smaller ℓ_d.

3   Turbulence in collisionless magnetized plasmas

Does turbulence in magnetised astrophysical plasmas share the above universal characteristics of neutral flows? Are plasma fluctuations self-similar at different scales and what is the nature of these fluctuations? What is the nature of the intermittency? How does dissipation set in? at which scale? and is dissipation spectrum universal?

To answer these questions, we shall mainly consider solar wind turbulence, which is perhaps our best laboratory for studying astrophysical plasma turbulence (Tu and Marsch, 1995; Horbury et al., 2005; Matthaeus and Velli, 2011; Bruno and Carbone, 2013; Alexandrova et al., 2013). Then we will give several examples of the solar wind downstream of planetary bow-shocks (of Earth and Saturn), called planetary magnetosheath.

Let us summarize now the differences between astrophysical plasmas and usual neutral fluids. In natural plasmas:

- there is a mean magnetic field $\mathbf{B}_0$, which introduces a privileged direction and imposes an anisotropy of turbulent fluctuations. It allows waves to propagate, even in the incompressible limit (Alfvén waves);

- the collision frequency is very low, thus the dissipation process at work and the dissipation scale ℓ_d are not known precisely;

- there is a number of plasma kinetic scales, namely, Larmor radius and cyclotron frequency of charged particles, their inertial length, the Debye length;

- there is a wave dispersion: beside Alfvén waves, one may also expect fast and/or slow magnetosonic waves at MHD scales, and, at kinetic scales, kinetic Alfvén, whistler or slow/ion-acoustic waves, etc.

As we will show below, notwithstanding this complexity, there is a certain degree of generality in space plasma turbulence, and there are similarities with incompressible neutral fluids.

Turbulent spectrum in the solar wind at $R \geq 0.3$ AU

Solar wind is the coronal plasma in spherical expansion. It is inhomogeneous, with a dense slow wind blowing at low heliographic latitudes and a fast and more tenuous wind at high latitudes. Observations at $R \geq 0.3$ AU indicate that the following picture can be valid. The large scale magnetic field of the Sun forms an Archimedean spiral in the Heliosphere, with a step of ~ 6 AU (for the solar wind speed $V = 400$ km/s), also called *the Parker spiral* (Parker, 1958). At smaller scales, the solar wind is filled with flux ropes more or less aligned with the Parker spiral: the scale of these flux tubes correspond to the size of granules on the solar surface and is of the order of the largest scale of the turbulent cascade; the mean diameter of a flux tube at 1 AU is estimated to be $\sim 10^6$ km (Borovsky, 2008). At smaller scales, a turbulent cascade is observed.

Figure 1.1: (Top) Combined magnetic spectrum from different time intervals and different space missions (Kiyani et al., 2015). (Bottom) Magnetic spectrum $P_\perp = \mathrm{PSD}(k_\perp)$ is the power spectral density (PSD) of the $k_\perp$ fluctuations, measured while the flow-to-field angle Θ_{BV} is quasi-perpendicular ($\Theta_{BV} \in [80, 90]^\circ$), shown by blue open squares. Magnetic spectrum of $k_\parallel$ fluctuations, $P_\parallel = \mathrm{PSD}(k_\parallel)$, is measured while $\Theta_{BV} \in [0, 10]^\circ$ (blue dots). The total Fourier spectrum is shown in gray. $P_\perp$ is more intense within the inertial range; it follows a power-law with the spectral index $-5/3$. $P_\parallel$ has a lower intensity, is steeper and has a spectral slope -2. At the energy injection scales $f < 5 \cdot 10^{-4}$ Hz (which correspond to spatial scales $k\rho_i < 2 \cdot 10^{-3}$) the fluctuations are isotropic and their spectrum follows a law $\sim f^{-1}$. Courtesy of R. Wicks. The same figure as a function of $k\rho_i$ can be found in (Wicks et al., 2010).
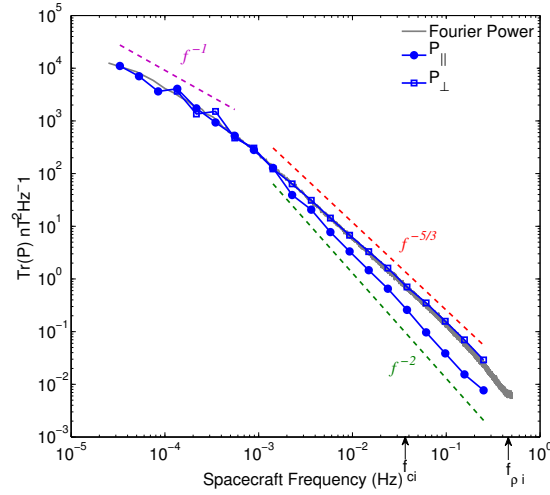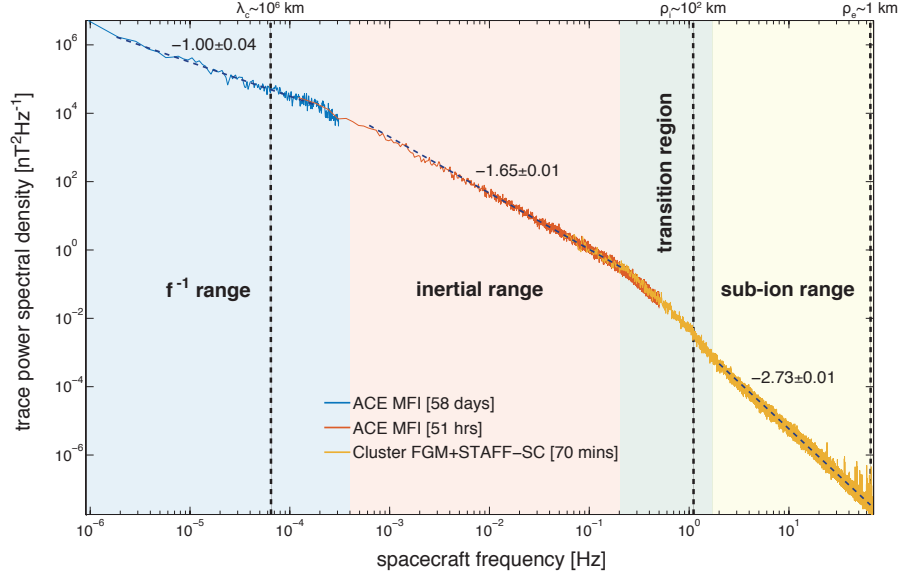
7

Figure 1.1(Top) shows a combined magnetic spectrum from different time intervals and different space missions (Kiyani et al., 2015). Is there a meaning in combining different solar wind streams and satellites? It seems so because all these spectra overlap perfectly (K. Kiyani, private communication, 2017). The observed spectral behaviour is typical for any other solar wind measurements and then can be used as a representative example. One observes here magnetic fluctuations $\delta\mathbf{B}$ covering nearly 8 decades in frequencies and more than 14 decades in power spectral density. At very large scales (low frequencies), the spectrum follows a law f^{-1}. The fluctuations are Alfvénic in nature with $\delta\mathbf{B}$ aligned (or anti-aligned) with velocity fluctuations $\delta\mathbf{V}$ (e.g., Belcher and Davis, 1971; Gosling et al., 2009). However, these Alfvénic fluctuations are not classical linear Alfvén waves as their relative amplitude $\delta B/B_0$ is of order 1 (e.g., Horbury et al., 2005; Tsurutani et al., 2011b; Chen, 2016; Matteini et al., 2018). The wave vectors are isotropic at such large scales, see Figure 1.1 (Bottom) from (Wicks et al., 2010), where we observe the same energy in $k_\parallel$ and $k_\perp$ fluctuations. The separation in $k_\parallel$ and $k_\perp$ fluctuations was done by varying the sampling direction with respect to the local $\mathbf{B}_0$ (Horbury et al., 2008; Wicks et al., 2010). Indeed, when the angle Θ_{BV} between the flow and the field is close to zero, the satellite measures $k_\parallel$ fluctuations; when $\Theta_{BV} \simeq 90°$, the $k_\perp$ fluctuations are observed.

At large scales, where the mean field $\mathbf{B}_0$ is of the same order as the fluctuations, the $\mathbf{B}_0/|\mathbf{B}_0|$ direction is ill-defined. That explains the observed isotropy of the $\mathbf{k}$ distribution at large scale. This low frequency range corresponds to scales between 10^6 km (that is just larger than the radius of the Sun $R_{\mathrm{Sun}} \simeq 0.7 \cdot 10^6$ km) and up to 10^8 km ~ 1 AU (Veltri, 1994). It is usually called the *energy-containing scales* (Bruno and Carbone, 2013). However, the exact physical process which generates the f^{-1} spectrum is still under debates (e.g., Horbury et al., 2005; Verdini et al., 2012).

At 1 AU, the MHD inertial range is observed between 10^{-3} Hz and 10^{-1} Hz (corresponding to 10^6 km $> \ell > 10^3$ km), see both panels of Figure 1.1. Here, the spectrum follows the Kolmogorov scaling for the $k_\perp$ fluctuations, $P_\perp \sim k_\perp^{-5/3}$, and a steeper one for the $k_\parallel$ fluctuations, $P_\parallel \sim k_\parallel^{-2}$, which reminds the spectrum of any kind of magnetic discontinuity along $\mathbf{B}_0$ (bottom panel). Note that the spectrum in the top panel shows the Kolmogorov scaling, as far as the $k_\perp$ fluctuations dominate turbulence within the inertial range[2].

The observed anisotropic scaling in the inertial range is in agreement with the critically balanced Alfvénic turbulence model of Goldreich and Sridhar (1995). This model is based on the assumption that in incompressible MHD turbulence, the non-linear time $\tau_{NL} = 1/(\delta z^\pm k_\perp)$ (with Elsässer variables $\delta z^\pm = \delta V \pm \delta B$, where δB is in velocity units) is of the same order as the Alfvén time $\tau_A = 1/(V_A k_\parallel)$ (the linear time of the parallel propagating Alfvén waves). An experimental verification of this assumption was done by Chen (2016) using the simplified definition of the non-linear time: $\tau_{NL} = 1/(\delta B k_\perp)$. Then, the ratio $\tau_A/\tau_{NL} = (k_\perp/k_\parallel)(\delta B/B_0)$ turns out to be constant within the inertial range and close to unity. This result seems to indicate that critical balance is indeed

---

[2]In fact, it is natural that the $k_\perp$ spectrum dominates: both spectra start at the same level at large scales, but the $k_\parallel$ spectrum is steeper.

at work within the inertial range. However, pure Alfvénicity is not observed (Grappin et al., 1983; Salem, 2000; Podesta et al., 2006; Boldyrev, 2006; Salem et al., 2009; Alexandrova et al., 2013; Grappin et al., 2016; Verdini et al., 2018, 2019): the parallel velocity spectrum follows the $k_\parallel^{-2}$ scaling, like the magnetic field (Wicks et al., 2011), but the perpendicular and dominant one is flatter, $k_\perp^{-3/2}$. Moreover, density fluctuations are ubiquitous in the solar wind and follow the Kolmogorov scaling within the inertial range (Celnikier et al., 1983; Issautier et al., 2010; Howes et al., 2012; Chen et al., 2012a,b, 2013; Šafránková et al., 2013).

If the spectral shape of different fluctuating quantities is more or less well established for radial distances $R \geq 0.3$ AU, the energy injection, transfer and dissipation rates are matters of debates (e.g., Sorriso-Valvo et al., 2007; Marino et al., 2008; Carbone et al., 2009; Alexandrova et al., 2013; Banerjee and Galtier, 2014; Banerjee et al., 2016; Sorriso-Valvo et al., 2018a,b; Kuzzay et al., 2019; Yang et al., 2019). These rates are closely related to the amplitude of the turbulent spectrum. In this manuscript, we will adress the turbulence level within the inertial range and its relation to the plasma parameters in the solar wind (see Chapter 2, Section 1).

The inertial range stops at frequencies (and scales) around ion characteristic scales, such as the ion cyclotron frequency $f_{ci} = eB_0/2\pi m_i$ (where e is the elementary charge and m_i is the ion mass), the ion inertial length $\lambda_i = c/\omega_{pi}$ (where ω_{pi} is the ion plasma frequency) and the ion Larmor radius $\rho_i = V_{i\perp}/\omega_{ci}$ (where $V_{i\perp} = \sqrt{2kT_{i\perp}/m_i}$ is the ion thermal speed in the plane perpendicular to $\mathbf{B}_0$, $T_{i\perp}$ is the perpendicular ion temperature and $\omega_{ci} = 2\pi f_{ci}$). At these scales, the MHD approximation is no more valid, ions and (light) electrons behave separately (e.g., Matthaeus et al., 2008; Stawarz et al., 2016; Chen and Boldyrev, 2017; Hellinger et al., 2018; Papini et al., 2019). In Fourier space, at 1 AU, ion scales cover approximately one decade, from 0.1 to 1 Hz (corresponding to $\ell \in [10^2, 10^3]$ km), see *transition range* in Figure 1.1 (Top). Here, the turbulent spectrum undergoes a steepening (Leamon et al., 1998b; Bale et al., 2005; Alexandrova et al., 2007; Chen et al., 2012b; Šafránková et al., 2013) and the spectral shape is variable (e.g., Smith et al., 2006; Bruno et al., 2014; Lion, 2016; Lion et al., 2016)[3].

The physical nature of the range around ion scales is strongly debated: is it the beginning of the dissipation range? or does the turbulent cascade just change its nature? Or both phenomena take place? What is the physical scale responsible for the spectral change? We will discuss these questions in more details in Chapter 2, Section 2.

What happens with turbulence at scales smaller than the ion scales? The first solar wind observations at sub-ion scales were reported by Denskat et al. (1983), using Helios/SCM at radial distances $R \in [0.3, 0.9]$ AU. From this pioneering work we know that between ion and electron scales, the magnetic spectrum follows the $\sim f^{-3}$ power law. That is close to the spectrum shown in Figure 1.1 (Top).

Thanks to the Cluster/STAFF instrument (Escoubet et al., 1997; Cornilleau-Wehrlin et al., 1997), which is the most sensitive Search Coil Magnetometer by today, the small scale tail of the electromagnetic cascade at 1 AU could be explored down to a fraction of

---

[3]This is normal: in the presence of characteristic scales no one expects to observe a general self-similar behaviour.

electron scales[4] $\sim 0.2-1$ km (Mangeney et al., 2006; Lacombe et al., 2006; Alexandrova et al., 2008b, 2009, 2012, 2013; Sahraoui et al., 2010, 2013; Lacombe et al., 2017; Matteini et al., 2017).

The Cluster observations at electron scales seem confusing at first glance: the spectral shape of the magnetic fluctuations vary from event to event suggesting that the spectrum is not universal at kinetic scales (Mangeney et al., 2006; Sahraoui et al., 2010, 2013). However, as we show in (Lacombe et al., 2014; Roberts et al., 2017; Matteini et al., 2017), most of these spectral variations are due to the presence or absence of whistler waves with frequencies of a fraction of f_{ce} and wave vectors $\mathbf{k}$ quasi-parallel to $\mathbf{B_0}$. These waves may result from the development of some instabilities associated to an increase of the electron heat flux and/or an increase of the electron temperature anisotropy, in some regions of the solar wind (Štverák et al., 2008).

Are whistler waves part of the background turbulence at kinetic scales? Our analysis of the anisotropy (in amplitudes of the fluctuations and in the distribution of wave vectors) shows that turbulent fluctuations at sub-ion and up to sub-electron scales have low frequencies in the plasma frame ($f \simeq 0$) and wave vectors mostly perpendicular to the mean field $\mathbf{k} \perp \mathbf{B_0}$ (Lacombe et al., 2017). This background turbulence is convected by the solar wind (with the bulk speed $\mathbf{V}$) across the spacecraft and appears in the satellite frame at frequencies $f = k_\perp V/2\pi$. It happens that these frequencies are below but close to f_{ce}, exactly in the range where whistler waves (with $\mathbf{k}\|\mathbf{B_0}$ and $f_{lh} \leq f \leq f_{ce}$, where $f_{lh} = \sqrt{f_{ce}f_{ci}}$ is the low hybrid frequency) may appear locally. Therefore, the superposition of turbulence and whistlers at the same frequencies is incidental. If we could do measurements directly in the plasma frame, these two phenomena would be completely separated in $\mathbf{k}$ and f. We discuss our observations of whistlers in the solar wind (Lacombe et al., 2014; Kajdič et al., 2016; Krishna Jagarlamudi et al., 2020) in Chapter 2, Section 6.

Chapter 2, Section 3 describes the spectral shape of the background turbulence at sub-ion scales, i.e., in the absence of parallel whistler waves. We show that the magnetic spectrum has a general shape, independently of plasma conditions and of radial distances, for $R \in [0.3, 1]$ AU. This general spectrum is similar to what is observed in the dissipation range of neutral fluids.

Which plasma scale plays the role of the dissipation scale ℓ_d in a nearly collisionless medium? Using different independent tests, we could show that in the solar wind, it is the electron Larmor radius ρ_e, which plays the role of ℓ_d for the electromagnetic turbulence. This result seems to be valid at different radial distances from the Sun. See Chapter 2, Section 4, for more details.

Intermittency in space plasmas?

As we have discussed in Section 2 of this chapter, intermittency is the second universal property of any turbulent system. In hydrodynamic turbulence, it is manifested by non-

---

[4]The electron scales, namely f_{ce}, λ_e and ρ_e, are defined in equivalent way as the corresponding ion scales.
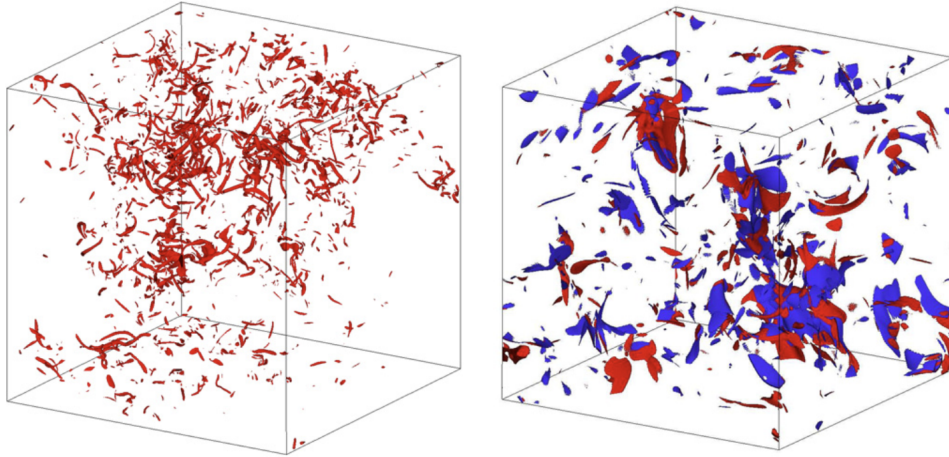
Figure 1.2: Intermittent structures in turbulent flows. Left: vortex filaments in 3D incompressible Navier–Stokes turbulence. Shown are iso-surfaces of high vorticity. Right: current filaments and current sheets in 3D incompressible MHD turbulence. Shown are iso-surfaces of high vorticity (red) and high current density (blue). The form of the structures and their dimension is believed to have major impact on turbulent statistics. Figure from (Grafke et al., 2015).

Gaussian statistics of velocity increments. Intermittency is believed to be responsible for a non-homogenous energy transfer and dissipation. It is due to coherent structures in the form of filaments of vorticity, as can be observed in 3D incompressible hydrodynamic numerical simulations, Figure 1.2 (Left).

What do we know about intermittency and coherent structures in space plasmas? Signatures of intermittency, such as departure from Gaussianity of the PDFs of the fluctuating quantities (e.g., components of the magnetic field and velocity) and increases of Kurtosis toward small scales, are widely observed in the solar wind (e.g., Veltri, 1994; Sorriso-Valvo et al., 1999; Salem et al., 2009; Bruno and Carbone, 2013).

Figure 1.2 (Right) shows isosurfaces of high current density in 3D incompressible MHD simulations. We can recognise here current filaments (similar to the high vorticity regions in hydrodynamic simulations), but as well, planar structures, which can be interpreted as current sheets.

Starting with the first *in-situ* measurements, planar discontinuities in the interplanetary magnetic field have been detected (Burlaga, 1969; Burlaga and Ness, 1969). Since then, there has been debate on their nature, origin and role in solar wind heating (e.g., Burlaga, 1971; Burlaga et al., 1977; Vasquez and Hollweg, 1996, 2001; Horbury et al., 2001; Söding et al., 2001; Knetter et al., 2004; Neugebauer, 2006; Tsurutani et al., 2007, 2011a; Gosling, 2012; Artemyev et al., 2018, 2019). And what if the planar discontinuities at scales $\ell < 10^6$ km (i.e., within the inertial range and at smaller scales) are the result of developed turbulent cascade in the solar wind?

Turbulence analysis of Veltri and Mangeney (1999), Veltri (1999) and Mangeney et al. (2001) showed that intermittency in the solar wind inertial range is due to planar coherent structures in the form of shocks and current sheets. This analysis, where

11

turbulent fluctuations are defined via Haar wavelets, detects high amplitude events which are responsible for non-Gaussian statistics.

Greco et al. (2009, 2010, 2012) compared *in-situ* observations and MHD numerical simulations. In these studies, the *Partial Variance of Increments* (PVI) method is used to detect strong changes in the field components within the inertial range. The authors showed a nice agreement between statistical properties of intermittency in the solar wind and in the simulations. The shape of magnetic structures is very similar and looks like current sheets. Within the kinetic range of scales, again using the PVI method, Perri et al. (2012a) and Greco et al. (2016) have detected current sheets as well.

Indeed, current sheets are good candidates for a local dissipation by magnetic reconnection (e.g., Velli, 2003; Retinò et al., 2007; Sundkvist et al., 2007; Servidio et al., 2009; Osman et al., 2011). Thus, as in hydrodynamic turbulence, these intermittent structures can be the origin of a non-homogenous energy transfer and dissipation in space.

Are there other types of structures? Does their topology change across the cascade? In Chapter 3, we first attempt to give a definition of *a coherent structure*. One of the most important properties of a coherent structure is its phase coupling across a wide range of scales (like in a shock wave, where phases of each Fourier component are fixed to the same value). Second, we show a way to detect signatures of phase coupling in the data. We find that these signatures start at the break point between the f^{-1} and $f^{-5/3}$ ranges, and go through the cascade up to the smallest resolved scales. See Chapter 3, Section 1 for more details. Chapter 3, Section 2 shows the relation between the phase coupling and non-Gaussianity of turbulent fluctuations.

Regarding the topology of structures (Chapter 3, Section 3), we find magnetic holes, solitons, small-scale shocks, current sheets, but mostly, magnetic vortices (Lion et al., 2016; Roberts et al., 2016; Perrone et al., 2016, 2017). Indeed, unlike previous works, where to detect structures the threshold was applied on the amplitudes of PVI, here we apply it on the amplitudes of (i) the Morlet wavelet coefficients and (ii) fluctuations in physical space. This explains why we detect not only planar discontinuities.

Magnetic vortices are cylindrical structures with a field aligned current. We detect them within the inertial range and at ion scales. Recently, we find them at sub-ion scales as well (Alexandrova et al., 2020). These structures are much more energetic than the background and are thus responsible for the observed general spectrum at kinetic scales.

Our results indicate that magnetic vortices are important features of the space plasma turbulence. We focus on Alfvén vortices in Chapter 4. First, we remind the basic equations of MHD Alfvén vortices. Second, we discuss the spectral properties (Alexandrova, 2008) and apparent polarisation of the vortex signal passed by a spacecraft (Alexandrova and Saur, 2008), which is important for *in-situ* data interpretation. Then, we show our observations of the plasma behaviour within an Alfvén vortex detected by the MMS mission in the Earth's magnetosheath (Wang et al., 2019). Finally, we discuss recently developed models of fluid vortices in high-β plasma[5] ($\beta \sim 1$) and at ion, and electron

---

[5]Plasma parameter β is the ratio between the ion (electron) thermal pressure and magnetic pressure: $\beta_{i,e} = nkT_{i,e}/(B_0^2/2\mu_0)$, where n is the plasma density, $T_{i,e}$ is the ion (electron) temperatures, k – the Boltzmann constant and μ_0 is the magnetic constant.

scales (Jovanović et al., 2015; Jovanovic et al., 2020).

4 Concluding remarks

When I started working on solar wind turbulence after my PHD (November 2005), the kinetic range of turbulence was not well known, and it was thought to be characterised by a significant variability, depending on details of its formation.

I spent some time trying to clarify this situation. With my colleagues, we were able to show that this variability was mostly an effect of the way data are treated. More or less general spectrum is always present at kinetic scales. Indeed the variability of the exponents of the power-law spectra appears if the analysis is done at scales which include ion scales (as was usually done in the past, including by ourselves in the first studies (Alexandrova et al., 2007, 2008a) of the solar wind kinetic turbulence). This is due to the fact that at ion scales, different physical processes can be active including partial energy transfer from electromagnetic fluctuations to ions. At these scales (covering one decade) there is no reason to expect that a scale-free turbulence approach is valid. Similarly, variability at electron scales appears when parallel whistler waves are superimposed on the background turbulence in the satellite frame. At scales smaller than ion scales and in the absence of parallel whistlers, the spectrum follows indeed a universal shape.

Actually, beyond the question of methodology, our results answer to one of the open questions in space plasma turbulence: (1) what are the properties of kinetic plasma turbulence? and (2) are they universal, with a spectral shape independent of local plasma parameters? The answers to the second question is definitely yes.

The first question is directly related to intermittency. Before 2005, it was studied mostly within the inertial range and it was thought to be due to planar discontinuities, essentially current layers, most probably related to reconnection, as we have discussed above. My main contribution, together with my colleagues, students and post-docs, has been to show that planar discontinuities are not the only intermittent structures in space plasma turbulence. Cylindrical magnetic vortices play an important role in the cascade and they cover a wide range of scales, from fluid to kinetic.

Our results give new insights to physics of space plasma turbulence and we discuss theoretical interpretations of our findings in Chapter 5.

Chapter 2

Turbulent spectrum from MHD to electron scales

In this chapter, we focus on the turbulent spectrum of magnetic fluctuations in the solar wind from the MHD scales up to the plasma kinetic scales. Regarding the inertial range, we show that the turbulent energy is well correlated with the magnetic and ion thermal pressures for a wide range of radial distances from the Sun (between 0.5 and 5 AU). Regarding the kinetic scales, we show that for the perpendicular wave numbers $k_\perp$ the magnetic turbulent spectrum follows a universal shape, independent of the plasma conditions and of the solar wind type. The level of the kinetic spectrum correlates with the magnetic and ion thermal pressures as well. Using several independent approaches, we show that the Kolmogorov (or dissipation) scale in a collisionless plasma is the electron Larmor radius ρ_e. We propose a general description of the magnetic turbulent spectrum from ion to sub-electron scales. These results, established at 1 AU up to $200 - 400$ Hz (Alexandrova et al., 2009, 2012), have been recently verified at 0.9, 0.6 and 0.3 AU with the Helios measurements up to $\sim 500 - 700$ Hz (Alexandrova et al., 2020). Finally, we discuss observations of Alfvén-Ion-Cyclotron waves and whistler waves, generated by quasi-linear plasma instabilities, which modify the general spectral shape in the satellite frame, around ion and electron scales, respectively.

1 Amplitude of turbulence within the inertial range

Figure 2.1 shows turbulent spectra measured on Cluster by the FGM and STAFF(SC and SA) instruments, for seven time intervals in slow and fast wind with different β_i (see the caption of the left panel for the exact values of the solar wind speed V and proton plasma β_i values). Variations of the ion and electron scales among the intervals are indicated by horizontal black lines.

The Cluster mission being a magnetospheric mission is not going far in the solar wind; therefore (i) the time intervals in the solar wind are relatively short (i.e., the f^{-1} range is not resolved) and (ii) while being in the solar wind, the satellites are very often magnetically connected to the Earth's bow shock. The only way to avoid this connection
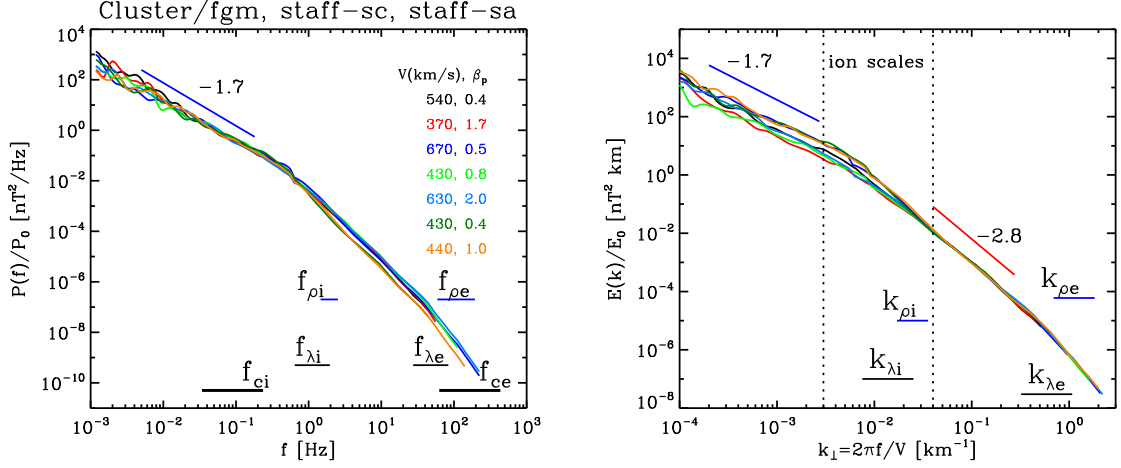
Figure 2.1: Seven solar wind turbulence spectra from MHD to electron scales for different solar wind conditions. Left: superimposition of the spectra within the inertial range. Right (will be commented in Section 3): superimposition of the same spectra within the sub-ion range; here, the variability of the spectra around ion scales is particularly well visible. The data are from (Alexandrova et al., 2009).

is to consider time intervals when the solar wind magnetic field is quasi-perpendicular to the wind flow. It appears that Cluster can be in the free solar wind only when the flow-to-field angle Θ_{BV} is greater then $60°$ (Alexandrova et al., 2012). This means that with Cluster we mostly resolve the $k_\perp$ turbulent fluctuations in the solar wind.

To underline the general shape of the spectra within the inertial range, we superimpose in Figure 2.1 (Left) all the spectra within the low frequency range, i.e., corresponding to scales larger than the ion spatial scales, ρ_i and λ_i. All the spectra follow a power law close to $\sim f^{-5/3}$. The factor P_0, which allows to superimpose the spectra, is the relative amplitude of each spectrum with respect to the most intense one[1]. Thus, P_0 is proportional to the absolute amplitude of the spectrum A_0, i.e., turbulence level. It is well correlated with the magnetic pressure $P_m = B_0^2/2\mu$ and with the wave number corresponding to the electron Larmor radius $k_{\rho_e} = 1/\rho_e$, see Figure 3(d) in (Alexandrova et al., 2009).

In the hydrodynamic turbulence, the amplitude of the spectrum is directly related to the energy injection rate ε

$$P(k) = A_0(\varepsilon)k^{-5/3}. \tag{2.1}$$

At the same time, as ε is supposed to be the same as the energy dissipation rate ε_d, A_0 is related to the dissipation scale ℓ_d:

$$A_0 \sim \varepsilon^{2/3} \sim \ell_d^{-8/3}, \tag{2.2}$$

i.e., the larger the energy injected in the cascade, the higher the spectrum and the smaller the dissipation scale.

---

[1]We take the most intense spectrum as a reference. For a given spectrum, the factor P_0 is the ratio between that spectrum and the reference one, averaged over frequencies of the inertial range.
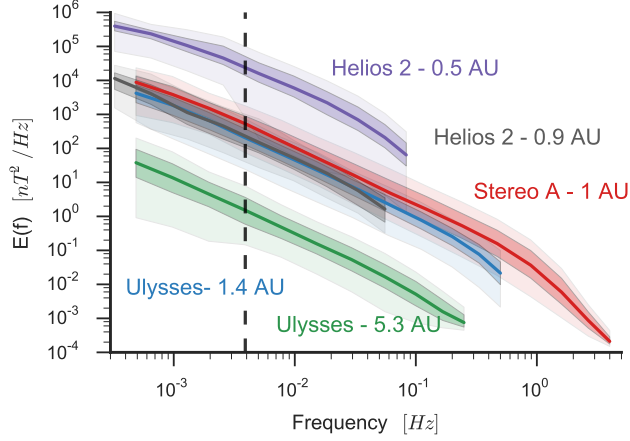
Figure 2.2: Magnetic field measurements by different satellites at different radial distances: the thick solid lines of different colours give the median $\mathrm{PSD}(f)$ at different R, the filled deep-coloured areas around represent 50% of the spectra around the median, the light areas show the extreme PSD levels. The vertical dashed line is at $3.9 \cdot 10^{-3}$ Hz, a common frequency within the inertial range for all R. Figure from the PHD thesis of Lion (2016).

The anticorrelation between P_0 and ρ_e observed in the solar wind (Alexandrova et al., 2009) makes us think that the electron Larmor radius ρ_e may play the role of the dissipation scale ℓ_d in a nearly collisionless solar wind. We will go back to this point below. Now we focus on the turbulence level in the solar wind and its relation to different plasma parameters.

In Figure 2.1 we have only considered 7 spectra. Let us now perform a larger statistical study of the solar wind spectral level within the inertial range and for various radial distances R. Figure 2.2, from the PHD thesis of Lion (2016), shows the distribution of magnetic power spectral density (PSD) as observed by different satellites at $R = 0.5$ and 0.9 AU (Helios), 1 AU (STEREO A), 1.4 and 5.3 AU (Ulysses). Each spectrum is integrated over 24 h. The vertical dashed line indicates $f_1 = 3.9 \cdot 10^{-3}$ Hz (which corresponds to a time scale $\tau \simeq 4$ min). It is a common frequency within the inertial range for all R and its PSD will be used as a reference for the turbulence level, $E_B = \mathrm{PSD}(f_1)^2$.

For any radial distance R, we find that (i) the turbulence level E_B is correlated with magnetic pressure P_m, as was observed for the 7 intervals of Cluster, and (ii) it correlates even better with the ion (or proton) thermal pressure $P_{th} = nkT_i$, see Figure 2.3 (Left, a-c). Indeed, a dependence between the amplitude of the frequency spectrum, within the inertial range, and the ion thermal pressure has been already measured by Helios spacecraft in the inner Heliosphere (Grappin et al., 1990). Here, we

---

[2]Note that E_B here is an absolute turbulence level at a fixed frequency within the inertial range and P_0 in Figure 2.1 is a relative turbulence level for the inertial range frequencies. Both have similar physical meaning.

confirm this correlation for a much wider range of radial distances[3].

For both pressures, P_m and P_{th}, we find the following relations:

$$\log\left(E_B(R)\right) = a_{m,th}\log(P_{m,th}) + b_{m,th}(R) \tag{2.3}$$

The radial evolution of the fitting parameters is shown in Figure 2.3 (Right, a-b). The factors of proportionality $a_m = a_{th} = a = 1$ for any R.

The intercepts $b_{m,th}$ varies with R, as expected in the expanding solar wind for the observed radial evolution of the solar wind plasma parameters (Lion, 2016). Indeed, if H is a physical quantity such as ion temperature T, plasma density n, magnetic field energy B^2 and turbulence level E_B, then one can write the following scaling with the radial distance:

$$H(R) = H(R_0)\left[\frac{R_0}{R}\right]^{\gamma_H}, \ H = T, n, B^2, E_B. \tag{2.4}$$

Combining equations (2.3) and (2.4), Lion (2016) has shown that

$$b_{th}(R) = b_{th}(R_0) + [a(\gamma_T + \gamma_n) - \gamma_{E_B}]\cdot\log\left[\frac{R_0}{R}\right], \tag{2.5}$$

$$b_m(R) = b_m(R_0) + [a\gamma_{B2} - \gamma_{E_B}]\cdot\log\left[\frac{R_0}{R}\right]. \tag{2.6}$$

From Helios observations, it is known that $\gamma_T \simeq -0.9$, $\gamma_n \simeq -2$, $\gamma_{B2} \simeq -3.2$ (Totten et al., 1995; Hellinger et al., 2013; Perrone et al., 2019a).

Taking radial evolution of the turbulence level at the energy injection scales as R^{-3} (Bavassano et al., 1982; Bruno and Carbone, 2013), and assuming that at the correlation scale (or the break scale between f^{-1} and $f^{-5/3}$ frequency ranges) the solar wind expansion time $\tau_{exp} = R/V$ is equal to the non-linear time τ_{NL}, it is possible to show that the radial evolution of the turbulence level within the inertial range has $\gamma_{E_B} = -4$ (Lion, 2016)[4]. Thus, we get the radial evolution of the intercepts $b_{th,m}(R)$, shown by dashed lines in Figure 2.3 (Right, a-b).

Figure 2.3 (Right, c-d) show the observed correlations between E_B and nT (c), and between E_B and B^2 (d) as a function of R: it seems that they improve with radial distance, and the correlations within the fast wind (in red) are better than within the slow wind (in green).

The correlations observed in Figure 2.3 mean that the energy injection and dissipation rates are mainly determined by P_m and P_{th}, see Equation (2.2), and this situations seems to improve with R. These results are puzzling. Indeed, in the solar wind, all the plasma parameters are more or less intercorrelated. For example, for the data set of STEREO analysed here, the correlation between the magnetic and thermal pressures

---

[3]We observe the same correlation for the kinetic range spectrum at 1 AU with Cluster in the solar wind (Alexandrova et al., 2013; Lacombe et al., 2017) and at 9.6 AU within the Saturn's magnetosphere (von Papen et al., 2014).

[4]This radial evolution was indeed observed *in-situ* by Bavassano et al. (1982)
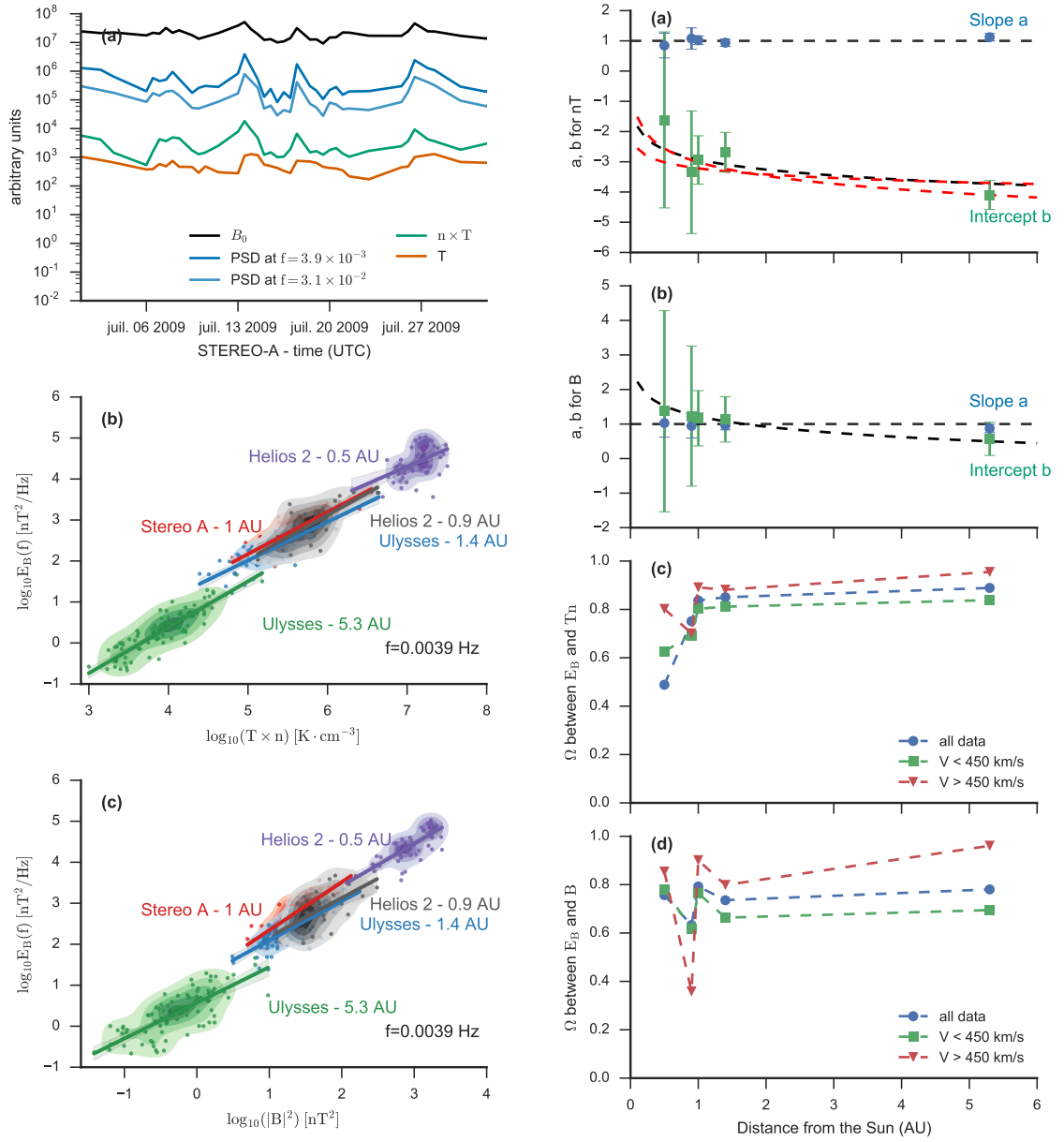
Figure 2.3: Left: (a) $B_0(t)$, $T_i(t)$, $nT_i(t)$ and $PSD(f_j,t)$, with $j = 1, 2$, at $f_1 = 3.9 \cdot 10^{-3}$ Hz and $f_2 = 3.1 \cdot 10^{-2}$ Hz, over one month of STEREO data (July 2009); (b) $\log(E_B)$ as a function of $\log(nT_i)$ for different R, with $E_B = PSD(f_1)$; (c) $\log(E_B)$ as a function of $\log(B^2)$. The solid lines in (b) and (c) give the linear fittings for each satellite.

Right: Radial evolution of the fitting parameters and correlations between E_B and P_{th} (a) & (c); and between E_B and P_m (b) & (d). The correlations are shown for the total data set (blue dots connected by the blue dashed lines), and separately, for the fast (red) and slow (green) solar wind subintervals. Correlations within the fast wind are higher. It seems that all correlations increases with R: for the total data set, the correlation coefficient $\Omega(E_B, nT)$ goes from 0.5 to 0.9 and $\Omega(E_B, B_0^2)$ goes from 0.4 to 0.8 with R. Is it an indication of a local process?

18

is $\Omega(B_0^2, nT) \simeq 0.5$ (not shown). The fact that both correlate with E_B with a higher correlation coefficient (especially for $R \geq 1$ AU, see Figure 2.3 (Right, c-d)) makes us think that independently both pressures are important for the energy injection and dissipation rates of the turbulent cascade. However, with our observations, we are not able to answer the fundamental questions, like:

- Why does a stronger magnetic field B_0 imply a higher level of turbulent fluctuations?

- Why is the plasma hotter within the regions with a stronger turbulence level?

- Is it turbulence, which heats the plasma, so that the ion thermal pressure increases? Or, is there a kind of a *fossil balanced energy allocation* between different degrees of freedom in the solar wind? In other words, in each flux tube starting at the Sun surface, is there a certain partition between the magnetic, kinetic, thermal and turbulent forms of the energy, that is maintained during the solar wind expansion? Thus crossing different flux tubes, a satellite will automatically measure correlations between the different forms of the energy and, particularly, the stronger turbulence level within the hotter plasma regions.

Recently, Matteini et al. (2018) have shown that the break scale between the f^{-1} and $f^{-5/3}$ ranges is characterised by $\delta B / B_0 \simeq 1$. This result together with our findings make us think that the following scenario is possible: a stronger magnetic field B_0 allows stronger fluctuations δB, while keeping $\delta B / B_0 \simeq$ const at the injection scale. Therefore, the mean field defines the energy injection in turbulent cascade, $\varepsilon(P_m)$. The turbulent cascade heats ions and their thermal pressure increases, i.e., $\varepsilon_d(P_{th})$. The fact that $\varepsilon = \varepsilon_d$ explains why we observe similar correlations of E_B with both, P_m and P_{th}. This scenario is compatible as well with the idea of a balanced energy allocation between different degrees of freedom in the solar wind and it can even explain the observed balance.

2 Ion transition scales

As we have already seen, at large scales all spectra are well superimposed in Figure 2.1 (Left). However, arriving to ion spatial scales, they start to diverge. The divergence of the spectra around ion scales, in a transition range (see the two vertical dotted lines in the right panel of Figure 2.1) is the manifestation of a deviation from self-similarity.

Physics of the ion transition range is a topic of debates. At these scales, different ion temperature anisotropy instabilities may take place, and there is thus a possible injection or dissipation of turbulent energy (see Section 6 of this chapter and Section 3.2 in the review by Alexandrova et al. (2013) for a more detailed discussion). Is it the beginning of the dissipation range or the starting point of another inertial range, where the characteristic eddy-turnover time is different thus the slope changes (e.g., Biskamp et al., 1996, 1999; Ghosh et al., 1996; Leamon et al., 1998b; Stawicki et al., 2001; Galtier, 2006; Galtier and Buchlin, 2007; Alexandrova et al., 2008a; Meyrand and Galtier, 2013)?

As was discussed in the Introduction, the characteristic plasma scale responsible for this spectral steepening, usually called the ion spectral break frequency f_b, is also under debates. If the MHD scale cascade was filled with parallel propagating Alfvén waves, the spectrum would show changes at the ion cyclotron frequency f_{ci}, where the parallel Alfvén waves undergo the cyclotron damping, or/and at the Doppler shifted resonant parallel wave number $k_r = 2\pi f_{ci}/(V_A + V_{th,i})$ (e.g., Bruno et al., 2014). The oblique kinetic Alfvén wave (KAW) turbulence is sensitive to the ion gyroradius ρ_i (e.g., Schekochihin et al., 2009; Boldyrev and Perez, 2012). The Hall MHD regime starts in the vicinity of the ion inertial length λ_i (e.g., Galtier, 2006; Servidio et al., 2007; Matthaeus et al., 2008, 2010).

In fact, the ion plasma parameter β_i can be written as ρ_i^2/λ_i^2. This means that for low β_i, the ion inertial length λ_i is the first plasma scale which the cascade 'meets' at the end of the MHD inertial range, and it can thus be responsible for the spectral steepening (Spangler and Gwinn, 1990; Alexandrova et al., 2013). For high β_i, it can be the ion Larmor radius ρ_i. Indeed, for extreme values of β_i, Chen et al. (2014) have shown that the break frequency f_b corresponds to λ_i for $\beta_i \ll 1$ and to ρ_i for $\beta_i \gg 1$. Based on Helios observations in the inner Heliosphere, where $\beta_i < 1$, we have shown that the $f_b(R)$ follows the $\lambda_i(R)$ scale under the assumption that turbulence develops mostly in the plane perpendicular to $\mathbf{B_0}$, i.e., the 2D turbulence with $\mathbf{k}_\perp \gg \mathbf{k}_\parallel$ (Bourouaine et al., 2012).

Later, we tried to approach the problem of the plasma scale responsible for the spectral steepening using 6 years of STEREO data (Lion, 2016). Figure 2.4 shows the dependences between the break frequency f_b, as it is usually defined[5], and four characteristic frequencies: (a) the Doppler shifted ion inertial length $f_{\lambda_i} = V/2\pi\lambda_i$, (b) the ion cyclotron frequency f_{ci}, (c) the Doppler shifted ion Larmor radius $f_{\rho_i} = V/2\pi\rho_i$, and (d) the Doppler shifted ion resonant scale $f_r = k_r V/2\pi$ of parallel Alfvén waves. Taking into account a possible β_i dependence, we show the data using different color codes: the whole dataset is shown in black, then the points corresponding to $\beta_i < 0.2$ are over-plotted in blue, and with $\beta_i > 1$ in red. One observes nice correlations of f_b with all the considered ion scales, and for any dataset: the correlation coefficient Ω is always higher than 0.5. For $\beta_i > 1$, all the correlations are close to 0.7 and for $\beta_i < 0.2$, they are of the order of 0.6. No particular scale stands out. This can be explained by the fact that different physical phenomena are at work at ion scales and all of them are important for the turbulence spectrum steepening. In a study by Lion et al. (2016), we illustrate this statement: for a rare case published by Leamon et al. (1998b) when the spectrum shows indeed a clear spectral break (in the fast wind with $\beta_i < 1$), we identify at the break scale (i) quasi-parallel AIC waves, which cover 20% of time, (ii) oblique coherent structures such as current sheets and Alfvén vortices, which cover 40% of time, and (iii) in the remaining 40% of time non-coherent noise. Any other combination or duration of the observed phenomena, and any other solar wind speed, would lead to another spectral shape at ion scales.

---

[5]Indeed, typically we do not observe a sharp spectral break, but a smooth transition. Thus f_b is defined as the frequency where the power-law fittings in the inertial and in the transition range intersect.
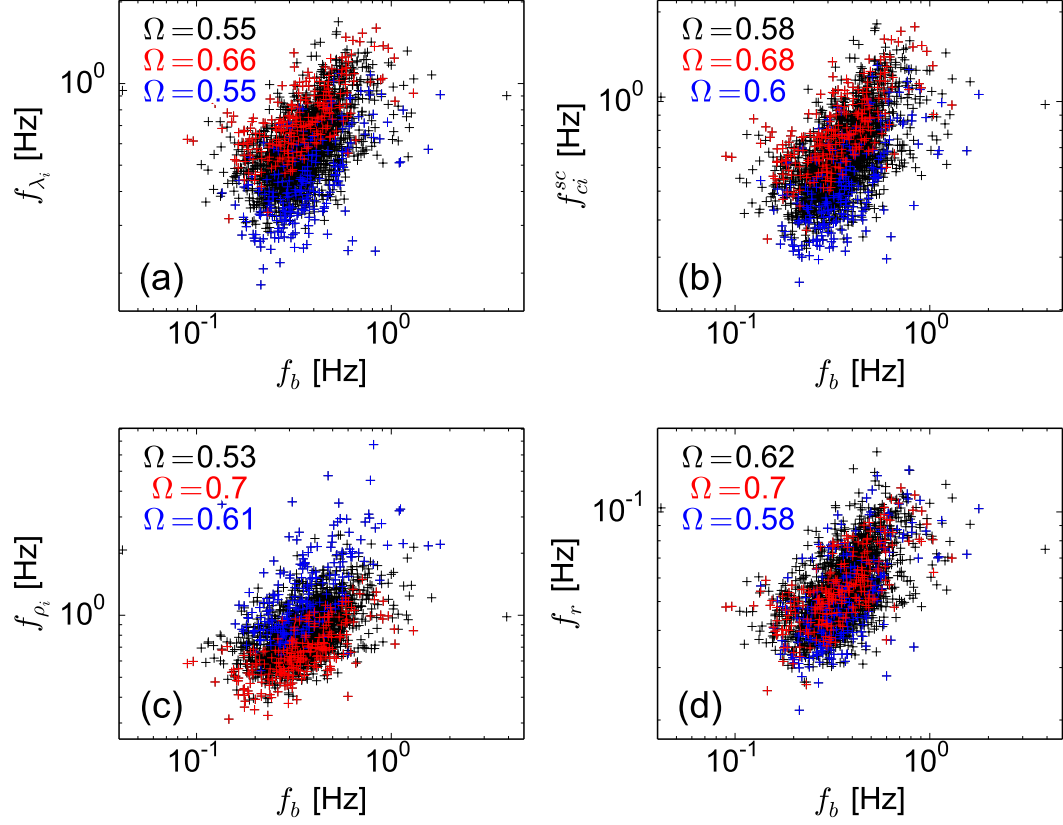
Figure 2.4: Dependences between the spectral break frequency f_b and ion plasma scales. Magnetic spectra are calculated from STEREO/MAG measurements between 2008 and 2014. Integration time of each spectrum is 9 hours, two spectra per day, for 6 years continuously ($\simeq 4380$ spectra/time intervals). f_b is defined as the frequency where power-law fittings in the inertial and kinetic ranges intersect. We show separately low and high β_p time intervals: $\beta_p < 0.2$ (blue), $\beta_p > 1$ (red), all data are shown in black. Figure from (Lion, 2016).
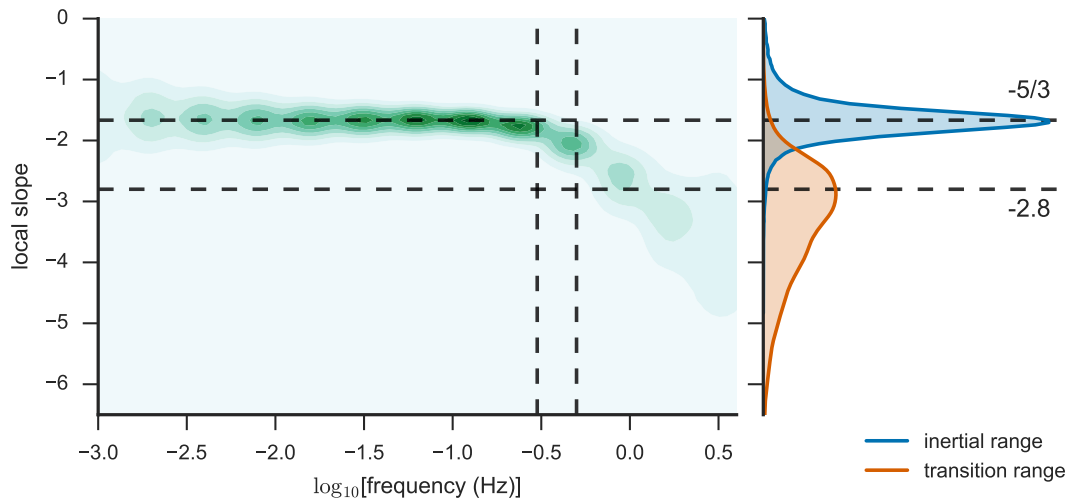
Figure 2.5: The same dataset of about 4380 spectra as in Figure 2.4. (Left) 2D–histogram of the local spectral slope estimated between 10^{-3} Hz and 3 Hz (over the inertial range and up to the end of the transition range around ion scales). The two vertical lines define the frequency range $[0.3, 0.5]$ Hz. (Right) 1D integrated histograms before and after delimited zone. Figure from (Lion, 2016).

Thus, from a general point of view, it is impossible to establish one given scale and to localise the ion transition in frequencies. This point can be also nicely illustrated by Figure 2.5, where we show the 2D–histogram of the local spectral slope of the STEREO/MAG spectra integrated over 9 hours twice a day for 6 years, from 2008 and up to 2014 (Left). As expected for a $k_\perp$ turbulence within the inertial range, the histogram is peaked around the Kolmogorov scaling. Approaching 0.3 Hz (left dashed vertical line), the slope starts to deviate from the $-5/3$ value. No stable mean is observed within the transition range (at $f \in [0.3, 3]$ Hz): the spectral slope decreases in a monotonic way. Thus, there is no definite meaning in the terminology *ion spectral break*, widely used in the literature (e.g., Leamon et al., 1998b; Markovskii et al., 2008; Bourouaine et al., 2012; Alexandrova et al., 2013; Chen et al., 2014; Bruno and Trenchi, 2014; Franci et al., 2016).

Instead, the whole frequency range where the ion scales appear in the spectrum (usually one decade between $0.1 - 0.3$ Hz and $1 - 3$ Hz, at 1 AU) must be avoided when turbulence approach is used (like interpretation of turbulent statistics, etc.). In particular, there is no meaning in a power-law fitting within this decade around ion scales. However, it can indicate a type of discontinuity which dominates ion scales (e.g., Alexandrova, 2008; Lion et al., 2016), see Chapter 4, Section 2 for more developed discussions of this point.

Now, let us go to smaller scales and discuss the spectral shape at sub-ion scales and around electron scales.

3 Turbulent spectrum within the kinetic range

Figure 2.1 (Right) shows the same spectra as in the left panel but as a function of $k_\perp = 2\pi f/V$, and superimposed (with a factor E_0) within the range of $k_\perp$ between $\{k_{\rho_i}, k_{\lambda_i}\}$ and $\{k_{\rho_e}, k_{\lambda_e}\}$. All spectra match perfectly at these scales. Thus, despite different plasma conditions (β_i varies between 0.4 and 2, solar wind speed is $V \in [370, 670]$ km/s), the perpendicular turbulence in the solar wind has *a general spectrum between ion and electron scales* (Alexandrova et al., 2009):

$$E(k_\perp) \sim k_\perp^{-2.8}. \tag{2.7}$$

A case study of Kiyani et al. (2009) and later observations by Chen et al. (2010); Alexandrova et al. (2012); Sahraoui et al. (2013) are in agreement with this finding. More precisely, a statistical study of Alexandrova et al. (2012) shows $\alpha = -2.86 \pm 0.08$, with limit values -3 and -2.6 (see Figure 5(a) in that paper). Sahraoui et al. (2013) gives the mean spectral index of -2.8 and its limits $[-3.1, -2.5]$, see Figure 5 (Left) in that paper. Note, that the scaling $\sim k_\perp^{-2.8}$ is observed only *out of* ion and electron scales. In the literature, a wider range of values can be found, but in most of cases where a different spectral index from -2.8 is found, the fitting procedure includes ion scales (e.g., Alexandrova et al., 2007, 2008a).

What happens at electron scales? Here, as at ion scales, one expects a loss of self-similarity. For our data sample of Figure 2.1, the electron scales appear at frequencies between 30 and 400 Hz: the Doppler shifted inertial length is $f_{\lambda e} = V/2\pi\lambda_e \in [30, 90]$ Hz; the electron Larmor radius appears at $f_{\rho e} = V/2\pi\rho_e \in [60, 200]$ Hz and the electron cyclotron frequency is $f_{ce} \in [60, 440]$ Hz. If we calculate the local spectral index α (not shown here), it follows a constant value $\alpha = -2.8$ up to 30 Hz (beginning of the electron scales). At higher frequencies it starts to decay monotonically, as we have observed already at ion scales, Figure 2.5. This monotonic decay of a local spectral index confirms what we can see by eyes: an exponential spectral shape at $f > 30$ Hz, that is a signature of a turbulence dissipation.

The complete kinetic range spectrum at sub-ion scales, including $k_\perp^{-2.8}$ as well as the dissipation range at electron scales, can be modelled by:

$$E(k_\perp) = Ak_\perp^\alpha \exp(-k_\perp \ell_d), \tag{2.8}$$

where A is the amplitude of the spectrum, α is the spectral index within the power-law range between ion and electron scales and ℓ_d – the cut-off or dissipation scale. In (Alexandrova et al., 2012) we have performed a statistical study of 100 solar wind spectra (integrated over 10 minutes under stable plasma conditions for each of them). The comparison of the spectra with the model function (2.8) shows that (i) the most probable spectral index is $\alpha = -8/3$; (ii) the cut-off scale correlates the best with the electron Larmor radius ρ_e, and the linear regression gives a proportionality coefficient of about 1; precisely we found $\ell_d \sim 1.4\rho_e$:

$$E(k_\perp) = Ak_\perp^{-8/3} \exp(-Ck_\perp\rho_e), \; C = 1.4. \tag{2.9}$$
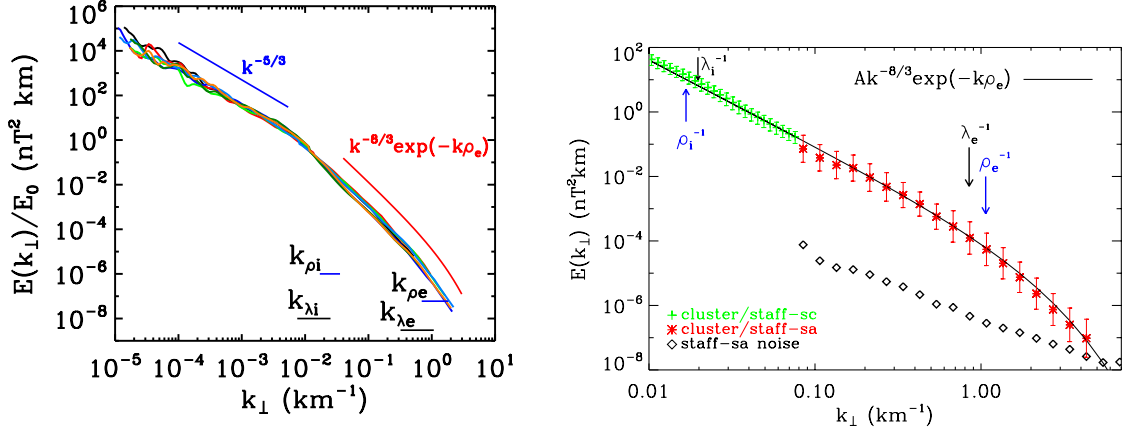
Figure 2.6: Left: Superposition of 107 solar wind spectra under different plasma conditions showing a general shape out of ion scales. Right: Example of the most intense spectrum measured well below electron scales by Cluster/STAFF and the model function (2.9), with $C = 1$, shown by a black solid line. Figures from (Alexandrova et al., 2012).

Note that $\alpha = -8/3 \simeq -2.67$ is not exactly -2.8 found between ion and electron scales. In fact, there is no contradiction in these apparently different numbers: the spectra continue to follow a $k_\perp^{-2.8}$ law between ion and electron scales, but when multiplied by $\exp(-Ck_\perp\rho_e)$, the spectral index of -2.67 should be used to describe the same slope.

Figure 2.6 (Left) shows a comparison of 107 superimposed spectra with the model function Equation (2.9), with $C = 1$. One may see that this function describes the whole spectrum, starting just "after" the ion scales and going beyond electron scales. The compensated spectra are flat over these 2 decades in $k_\perp$, see Figure 4 in (Alexandrova et al., 2012). To appreciate in more details the comparison between the observations and the model, the right panel of Figure 2.6 shows the most intense spectrum only at kinetic scales (as measured by Cluster/STAFF).

Recently, we have analysed Helios/SCM spectra in the inner Heliosphere (Alexandrova et al., 2020) and we have found that the model function

$$E(k_\perp) = Ak_\perp^{-8/3}\exp(-Ck_\perp\rho_e), \; C = 1.8. \tag{2.10}$$

can describe the kinetic spectra at 0.3, 0.6 and 0.9 AU, see Figures 2.7 and 2.8. The factor C here is slightly different from the one found with Cluster at 1 AU. These results should be verified with the Parker Solar Probe closer to the Sun and with the measurements of Solar Orbiter. Nevertheless, the shape of the spectrum seems to be the same at 4 radial distances analysed up to now, indicating the universality of the phenomena.
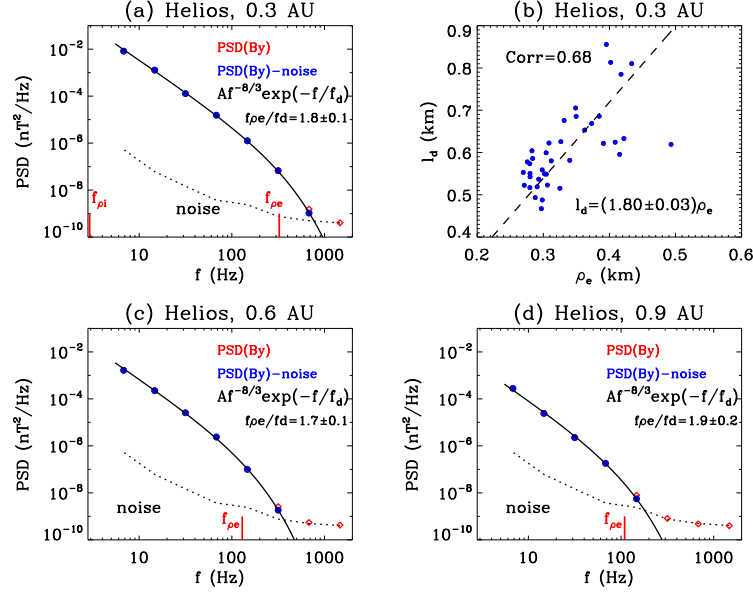
Figure 2.7: Helios spectra at (a) 0.3, (c) 0.6 and (d) 0.9 AU, as well as (b) the relation between the exponential cut-off scale ℓ_d and the electron Larmor radius ρ_e for the most intense 39 spectra at 0.3 AU. Figure from (Alexandrova et al., 2020).

4   Dissipation scale

As we have discussed in Section 1 of this chapter, in the solar wind, the level of turbulence, that is directly related to the energy cascade rate ε (see Equation (2.2)), is observed to be anticorrelated with the electron Larmor radius ρ_e (Alexandrova et al., 2009). Moreover, the exponential cut-off scale ℓ_d in Equation (2.8) correlates the best with ρ_e (Alexandrova et al., 2012; Alexandrova et al., 2020). If the intuitive picture from hydrodynamic turbulence is applicable to the solar wind, our findings point out that ρ_e can play the role of the dissipation scale in nearly collisionless astroplasmas. Let us confirm this statement by another independent test.

Based on the assumption of the balance between the energy injection at large scales and the energy dissipation at small scales, it has been shown that Kolmogorov's spectrum $E(k)$ normalised by the dissipation length ℓ_d and by the kinematic viscosity ν as $E(k)\ell_d/\nu^2$ is a universal function of $k\ell_d$ (Frisch, 1995; Davidson, 2004), i.e., the spectra for different turbulent flows normalised in this way superimpose.

Let's say that we have no *a priori* particular scale in mind, but different candidates for the dissipation scale exist: $\rho_{i,e}$, $\lambda_{i,e}$ and $f_{ci,ce}$. Figure 2.9 shows the Universal Kolmogorov Function $E(k)\ell_d/\nu^2$ as a function of $k\ell_d$ for the three independent candidates for ℓ_d, namely for ρ_i, λ_i and ρ_e; and for one temporal scale, namely the electron gyro-period f_{ce}^{-1} (Alexandrova et al., 2009). For simplicity, the kinematic viscosity ν (that is ill-defined in the solar wind) is assumed to be constant among the 7 time intervals shown here, despite the varying plasma conditions from one time interval to another.
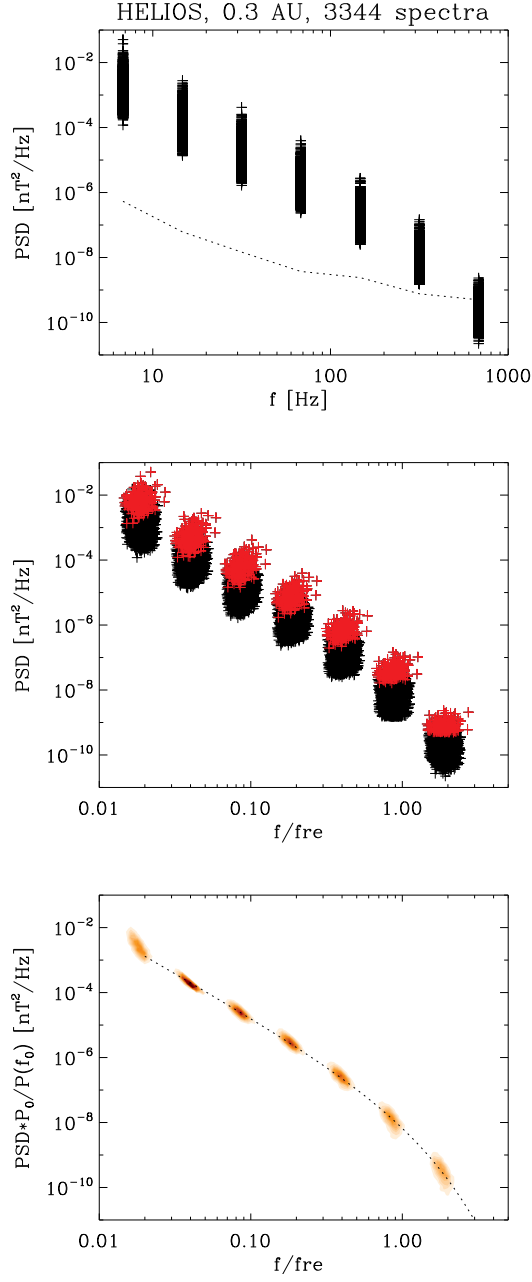
Figure 2.8: Helios spectra at 0.3 AU: (a) Raw 3344 spectra. (b) The same spectra as in (a) but as a function of the normalised frequency to the Doppler shifted ρ_e. The most intense 39 spectra are marked by red crosses. These spectra are used to determine the spectral shape, Equation (2.10). (c) The same spectra as in (b) but superimposed in amplitude and plotted as a 2D histogram. Dashed line represents Equation (2.10) without any particular fitting, only the amplitude was adjusted around $f/f_{\rho_e} = 0.04$. Figure from (Alexandrova et al., 2020).
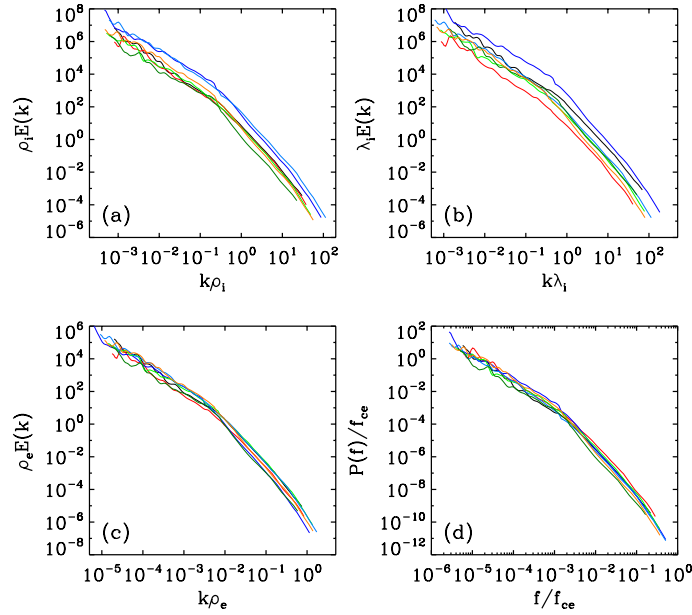
Figure 2.9: Universal Kolmogorov function $\propto \ell_d E(k)$ for different hypothetical dissipation scales ℓ_d as a function of (a) $k\rho_i$, (b) $k\lambda_i$, (c) $k\rho_e$ and (d) f/f_{ce}. Figure from (Alexandrova et al., 2009), corrected for 3 STAFF-SA frequencies, as explained in (Alexandrova et al., 2012).

One can see that the ρ_i and λ_i normalisations are not efficient to superimpose the spectra together. (Normalisation with λ_e gives the same result as with λ_i.) At the same time, the normalisations with ρ_e and f_{ce} bring the spectra close to each other, as expected while normalising with ℓ_d. So, in addition to the spectral analysis presented in Figure 2.6 and to the anticorrelation observed between P_0 and ρ_e, the Universal Kolmogorov Function normalisation gives an independent confirmation that the spatial scale which may play the role of the dissipation scale, in the weakly collisional solar wind, is the electron gyro-radius $\ell_d \sim \rho_e$.

5 Amplitude of the kinetic spectrum

Is it possible to completely determine the kinetic spectrum as a function of the plasma parameters? Up to now, an unclear parameter in Equations (2.9) and (2.10) is the amplitude of the spectrum A. Within the inertial range, the amplitude of the spectrum is well correlated with the mean magnetic and ion thermal pressures (averaged over 1 day time scale), as we have described above (Section 1). The Cluster/STAFF spectra of Figure 2.6 (Left) are integrated over 10 minutes while plasma parameters are nearly constant. Let us consider different forms of plasma pressure corresponding to these kinetic spectra.

Figure 2.10 shows dependencies between the amplitude $P_0 = \mathrm{PSD}(f_0)$ of the turbulent spectrum at $f_0 = 17.5$ Hz (within the kinetic range) and

27
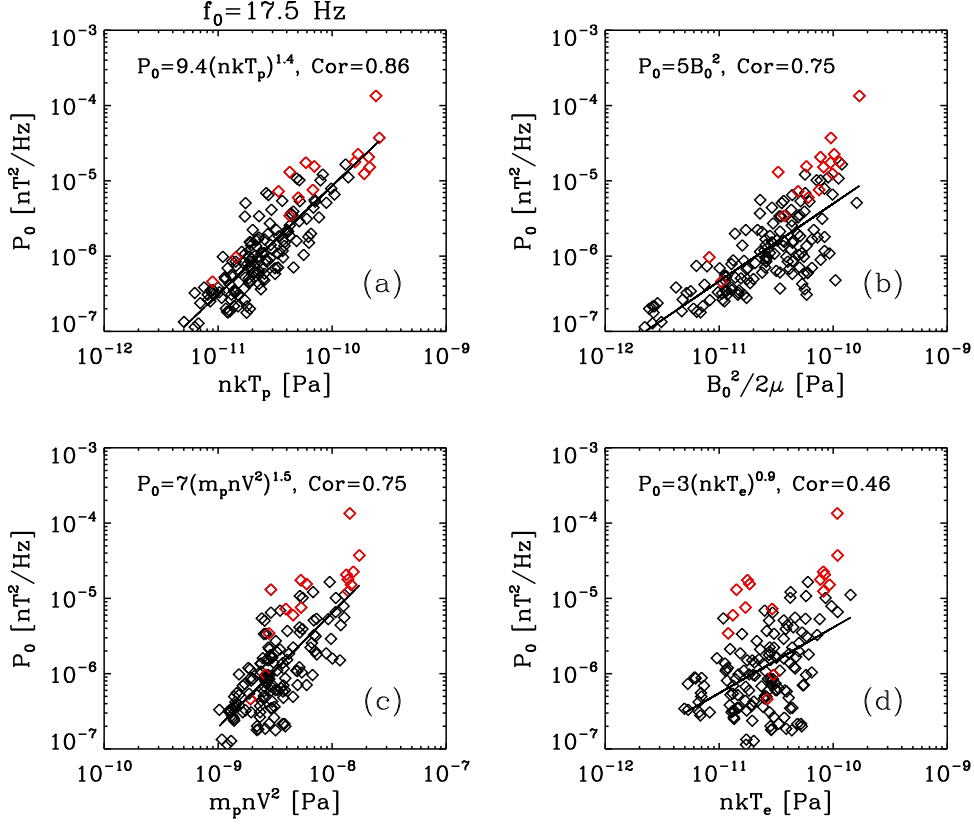
Figure 2.10: Amplitude P_0 of frequency spectra in the solar wind at $f_0 = 17.5$ Hz, i.e., within the kinetic range between ion and electron scales, as a function of (a) the proton thermal pressure $P_{th,p} = nkT_p$, (b) the magnetic pressure $P_{mag} = B_0^2/2\mu_0$, (c) the solar wind dynamical pressure $P_{dyn} = m_p n V_{sw}^2$, (d) the electron thermal pressure $P_{th,e} = nkT_e$. Red crosses are for time intervals downstream of interplanetary shocks. The best correlation is observed between P_0 and the ion thermal pressure. A 0.5 correlation is also observed with $T_{\perp,p}/T_{\parallel,p}$ (not shown); no correlation is found with the electron temperature anisotropy and ion and electron plasma betas. This dataset of 155 intervals in the free solar wind contains the 100 intervals where the spectra of Figure 2.6 (Left) are determined.

plasma pressures	B_0^2	nT_p	nT_e	nV^2
B_0^2	1.00	0.70	0.60	0.65
nT_p		1.00	0.75	0.90
nT_e			1.00	0.80
nV^2				1.00

Table 2.1: Intercorrelations between different forms of plasma pressures in the solar wind for the dataset of 155 time intervals of 10 minutes as measured by Cluster at 1 AU.

plasma parameters	B_0	n	V	T_p	T_e
B_0	1.00	0.30	0.50	0.50	0.50
n		1.00	-0.20	-0.15	0.15
V			1.00	0.90	0.25
T_p				1.00	0.45
T_e					1.00

Table 2.2: Intercorrelations between different solar wind plasma parameters for the same dataset as in Table 2.1.

(a) the proton thermal pressure nkT_p, with correlation coefficient $\Omega(P_0, nT_p) = 0.85$,

(b) the magnetic pressure $B_0^2/2\mu_0$, with $\Omega(P_0, B_0^2) = 0.75$,

(c) the solar wind kinetic pressure $m_p nV^2$, with $\Omega(P_0, nV^2) = 0.75$ and

(d) the electron thermal pressure nkT_e, with $\Omega(P_0, nT_e) = 0.45$.

This is done for a larger statistical sample of 155 time intervals of 10 minutes in the free solar wind, which include the 107 spectra of Figure 2.6 (Left).

Thus, we observe correlations between P_0 and all forms of pressures except may be the electron thermal pressure. The strongest correlation is again with nkT_p. And what about the others, are they independent?

Indeed, it is possible that some of the observed correlations in Figure 2.10 are induced by the inter-correlation of the plasma parameters and/or different forms of pressures in the solar wind. To address this issue, we calculate the two correlation matrices. The first, with the considered plasma pressures in Figure 2.10, B_0^2, nT_p, nT_e, nV^2, and the second, with the basic plasma parameters in the solar wind B_0, n, V, T_p, T_e, where each quantity is a column vector of size 155.

The matrices are indicated in Tables 2.1 and 2.2. All pressures are correlated among one another with $\Omega \geq 0.6$. Regarding plasma parameters, only the well known $T_p - V$ relationship (e.g., Démoulin, 2009; Perrone et al., 2019b) stands out with $\Omega \simeq 0.9$, then, a marginal correlation of 0.5 is observed between B_0 and $T_{e,p}$.

Let us focus on the ion thermal pressure nT_p, which seems to determine the turbulence level P_0 without any doubt. We find that the ion thermal pressure is strongly correlated with (i) the solar wind kinetic pressure $\Omega(nT_p, nV^2) \simeq 0.9$, and (ii) the electron thermal pressure $\Omega(nT_p, nT_e) = 0.75$. The first correlations is explained by the

$T_p - V$ relationship. The second one is due to the presence of density n in both quantities (the correlation between T_e and T_p being 0.45 only). Thus, we discard possible influence of the kinetic and the electron thermal pressures on the amplitude of turbulence spectrum at small scales: the observed $P_0 - nV^2$ and $P_0 - nT_e$ relations are simply induced by $nT_p - nV^2$ and $nT_p - nT_e$ strong correlations.

Can we discard the influence of magnetic pressure? Indeed, we observe quite an important correlation $\Omega(nkT_i, B_0^2) = 0.7$. However, this correlation coefficient is smaller than[6] $\Omega(P_0, B_0^2) = 0.75$. It seems that magnetic pressure is first related to turbulence level and then, via turbulence, correlates with nkT_p. In other words, the correlation between B_0 and nkT_p, which we observe here, is imposed by the turbulence, as we have discussed in Section 1 of this chapter.

Thus, the best and independent correlations of the level of the kinetic spectra are still with the ion thermal pressure and with the magnetic pressure

$$P_0 \sim (nkT_p)^{1.4} \sim B_0^2$$

as within the inertial range of the solar wind turbulence (Lion, 2016). That seems natural: all parts of the turbulent spectrum, from MHD to kinetic scales, go up and down together.

Analyzing spectra as a function of the satellite-frame frequency f is just a first step in understanding the solar wind turbulence. Let us now consider the k–spectra:

$$k = 2\pi f/V, \quad P(k) = P(f)V/2\pi.$$

We find that the correlations of the turbulence level at a given k_0, $P_0(k_0)$, with the magnetic and thermal pressures are still present although they decrease in absolute value (not shown).

And what about normalized spectra by the dissipation scale? We find that the amplitude of the k-spectra normalised by the electron Larmor radius,

$$P(k\rho_e) = P(k)/\rho_e,$$

does not correlate with the plasma pressures anymore. Only one correlation emerges, with ion temperature anisotropy $T_{i\perp}/T_{i\parallel}$ (with correlation coefficient of 0.6, see Figure 20(d) in Alexandrova et al. (2013)). Does it mean that ion temperature instabilities regulate the turbulence level at kinetic scales? At the moment, we have not fully understood the correlations summarized above, and the parametrisation of the turbulent spectrum is not complete.

---

[6]We remind that at large scales, we have observed $\Omega(nkT_i, B_0^2) \simeq 0.5$ and $\Omega(P_0, B_0^2) \simeq 0.7$ (see Section 1).

6 Non-universal spectral features at ion and electron scales due to narrow-band waves

Solar wind observations sometime show spectra different from the picture described above. In fact, when particle distributions are far from the local thermodynamic equilibrium (strong anisotropy, presence of beams or holes, etc...), quasi-linear plasma instabilities operate at scales close to the unstable particles scales in order to bring the plasma in a marginal stability state. A superposition of quasi-linear unstable waves on the background turbulence modify the observed spectrum in the satellite frame.

In case of unstable ions, with $T_{i,\perp} > T_{i,\parallel}$, the Alfvén-Ion-Cyclotron instability may operate if $\beta_i \leq 1$ (e.g., Gary et al., 1994; Schwartz et al., 1996; Hellinger et al., 2006; Matteini et al., 2007; Bale et al., 2009). This instability generates quasi-parallel Alfvén waves at a fraction of f_{ci}, with a left-handed (LH) circular polarisation[7], which resonantly interact with ions. In case of $\beta_i > 2$, the mirror mode instability (at scales close to ρ_i) operates to bring ions toward a more isotropic state. For the inverse anisotropy conditions $T_{i,\perp} < T_{i,\parallel}$, the firehose instability may dominate at ion scales (e.g., Matteini et al., 2007).

The distribution functions of electrons $f(V_e)$ are even more complicated than of ions (e.g., Maksimovic, 2007), as we have already mentioned in the introduction. A typical $f(V_e)$ is a combination of a quasi-thermal core, a Kappa-like halo and a Strahl (a field-aligned electron beam diffused in energy and propagating in the anti-solar direction). The core and halo of $f(V_e)$ can be anisotropic (Štverák et al., 2008). The Strahl can be more or less important and more or less focused around the direction of the mean field $\mathbf{B_0}$ (Maksimovic et al., 2005; Štverák et al., 2009; Kajdič et al., 2016; Berčič et al., 2019). All these non-thermal features may generate narrow-band right-handed (RH) parallel whistler waves at frequencies between the low hybrid frequency $f_{lh} = \sqrt{f_{ci}f_{ce}}$ and a fraction of the electron cyclotron frequency $\sim 0.5 f_{ce}$ (Gary and Feldman, 1977; Lacombe et al., 2014; Stansby et al., 2016; Tong et al., 2019a). Indeed, this frequency range was usually called *whistler wave turbulence* in the past (e.g., Beinroth and Neubauer, 1981).

The narrow-band waves at ion and electron scales are usually quasi-linear. They have small amplitudes $\delta B/B_0 < 0.1$ and appear in turbulent spectra as peaks, bumps or breaks, as a function of the filling factor of the wave with respect to the total time over which the spectrum is integrated, as we have shown in (Lacombe et al., 2014; Roberts et al., 2017). Thus, the presence of such waves makes the spectra different in shape from the general spectrum of the background turbulence described in Sections 1 to 5.

The only way to identify and separate these waves from the background turbulence is to measure the polarisation (phase differences between two perpendicular components to $\mathbf{B_0}$) of the magnetic fluctuations as a function of frequency and time, and then represent it as a polarisation map (see example in Figure 2.11 (Right)). The waves which interact resonantly with ions and electrons have a well defined polarisation in a given narrow frequency range and can thus be clearly seen in the polarisation maps. Below, we

---

[7]Left handed circular polarization corresponds to phase difference between two components in the plane perpendicular to $\mathbf{B_0}$ of $\Delta\Phi_{xy} = -90°$.
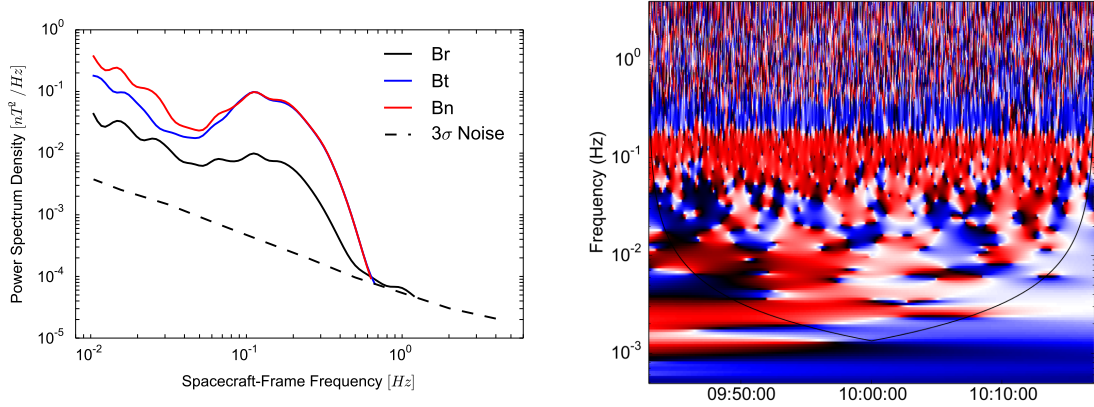
Figure 2.11: STEREO measurements on August 13, 2010, when $B_0 \simeq 3.6$ nT, $f_{ci} = 0.055$ Hz, $f_{lh} = 2.35$ Hz and $f_{ce} = 101$ Hz. Left: PSD of magnetic fluctuations in RTN frame. Right: Polarisation map in the plane perpendicular to the mean magnetic field. Here, red (blue) color corresponds to left-handed (right-handed) polarization. Figures from (Lion et al., 2016).

summarise our solar wind observations of AIC waves in the vicinity of ion scales, and of parallel whistlers in the vicinity of electron scales.

Quasi-parallel Alfvén Ion Cyclotron waves

During the PHD thesis of Sonny Lion, we have studied 6 years of STEREO measurements (2008–2014). It was shown that approximately $\sim 1\%$ of spectra have a bump at ion scales, as is shown in Figure 2.11 (Left) (Lion, 2016). The corresponding polarisation map in Figure 2.11 (Right) reveals a narrow band left-handed polarisation around 0.1 Hz (phase difference of $-90°$, in red) and right-handed polarisation around 0.3 Hz (phase difference of $90°$, in blue). This is probably an example of simultaneous counter-propagating Alfvén-ion-cyclotron waves[8].

Is it possible that AIC waves are permanent features of the solar wind but we do not see them all the time? AIC waves have wave vectors parallel to $\mathbf{B_0}$ which can be detected only when the satellite spans the solar wind in the direction of the mean field $\mathbf{B_0}$ (i.e., when the solar wind speed is aligned with $\mathbf{B_0}$). Figure 2.12 shows histograms of plasma parameters (proton velocity V, proton temperature T_p, density n and the angle between $\mathbf{B_0}$ and the radial direction Θ_{BR}) in the solar wind when only background turbulence is present (black solid line) and when AIC waves are observed (dashed line). The only clear difference appears in the histograms of the Θ_{BR}: the AIC waves are observed when $\Theta_{BR} \simeq 10 - 15°$ and around 150°.

These observations are in agreement with the results of Jian et al. (2009, 2014). In (Jian et al., 2009), the authors have analysed 2 months of STEREO A & B data in

---

[8]At 1 AU, right-handed whistlers are usually observed at $f > 3$ Hz (see below). Thus, the spectral bump within the $[0.05, 0.5]$ Hz frequency range observed here is hardly to be Doppler shifted whistler waves.

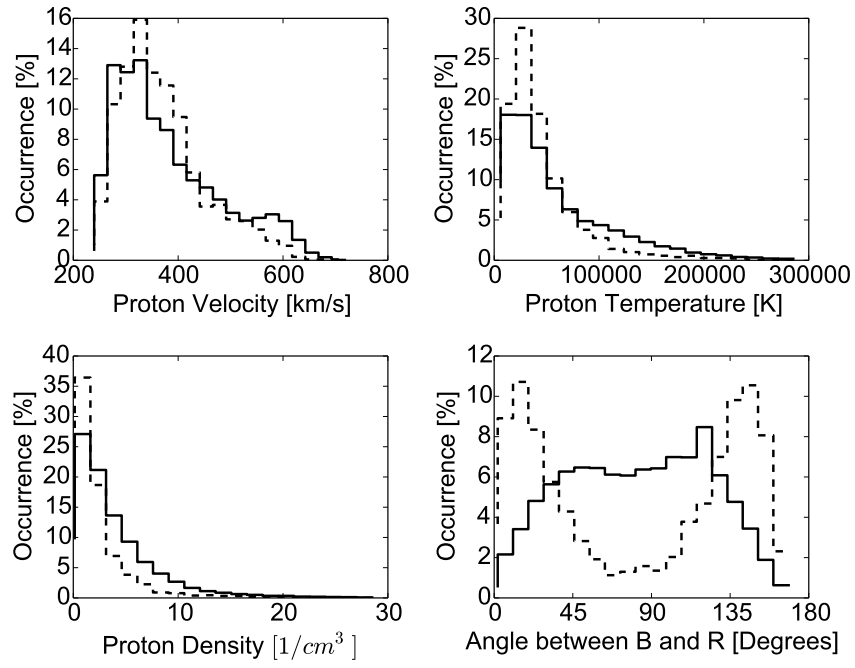Figure 2.12: Analysed dataset of STEREO A separated in two groups: without signatures of AIC waves (solid lines histograms) and with signatures of AIC waves (dashed). Distributions of V, T_p, n are the same for these two groups. The only difference can be seen in the histograms of Θ_{BR}: the AIC waves are observed while $\mathbf{B}$ is more or less radial. Figure from (Lion, 2016).
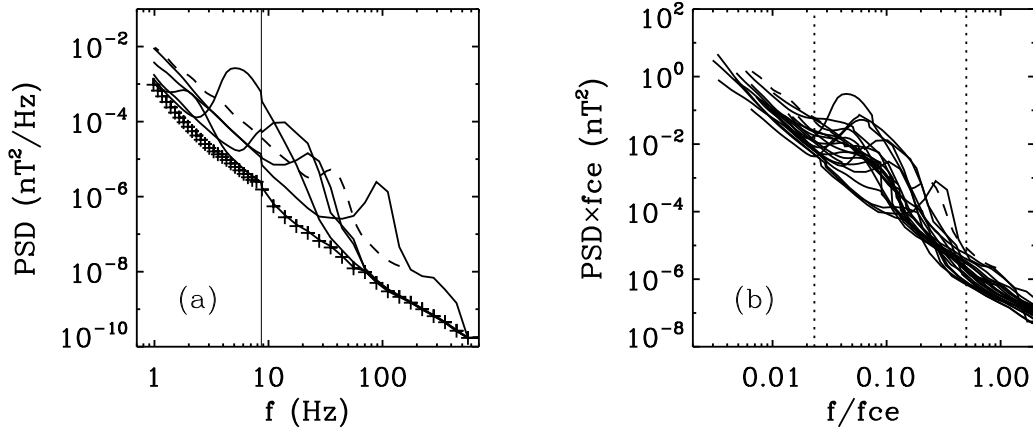
Figure 2.13: (a) Magnetic spectra with bumps covering [3,300] Hz range, with the signatures of quasi-parallel right-handed whistler waves. The solid vertical line gives the limit between SC and SA parts of the Cluster/STAFF instrument; (b) the same spectra but as a function of f/f_{ce}, the bumps appear between f_{lh} and $0.5f_{ce}$, see two vertical dotted lines. Figure from (Lacombe et al., 2014).

July-August 2007. They have shown that the spectral bumps at ion scales ($f \simeq 0.2$ Hz) correspond to quasi-monochromatic ion cyclotron waves propagating along $\mathbf{B_0}$. These waves occur usually when $\mathbf{B_0}$ is more or less radial ($\Theta_{BR} \in [0, 40]°$). In a larger statistical study, over the one year 2008 of STEREO data, Jian et al. (2014) have analysed bursts of left- and right-handed polarised waves lasting over 10 minutes, named in this study *Low-frequency waves (LFW) storms*. The authors concluded that storms and isolated wave-packets have the same properties: (i) the observed frequency is close to 0.2 Hz, (ii) the relative amplitude of waves is $\delta B_\perp/B_0 \simeq 0.03$, and (iii) the estimated wave vector in terms of the ion skin depth is $k\lambda_p \simeq 0.3$. Such waves are observed about 1% of the time at the Earth's orbit, when the magnetic field is radial. Storms are preferentially detected in the rarefaction regions following the fast wind.

Closer to the Sun, the magnetic field is more radial than at 1 AU; therefore, one might expect to observe AIC waves more than 1% of the time with the Parker Solar Probe/FIELDS measurements. First results recently published by Bowen et al. (2020) confirm this idea.

Quasi-parallel whistler waves

Similar spectral features as we have just seen but at electron scales are due to parallel whistlers. In (Lacombe et al., 2014) we have done the first large statistical study of quasi-parallel whistler waves in the free solar wind thanks to Cluster data. Indeed, it is with Cluster/STAFF-SA (constructed in DESPA, now named LESIA) that for the first time we have continuous measurements of the spectral matrix with polarisation properties of the fluctuations at frequencies $f \in [8, 4000]$ Hz, every 4 seconds. We have made a survey of five years of Cluster (2001–2005) and selected solar wind intervals not
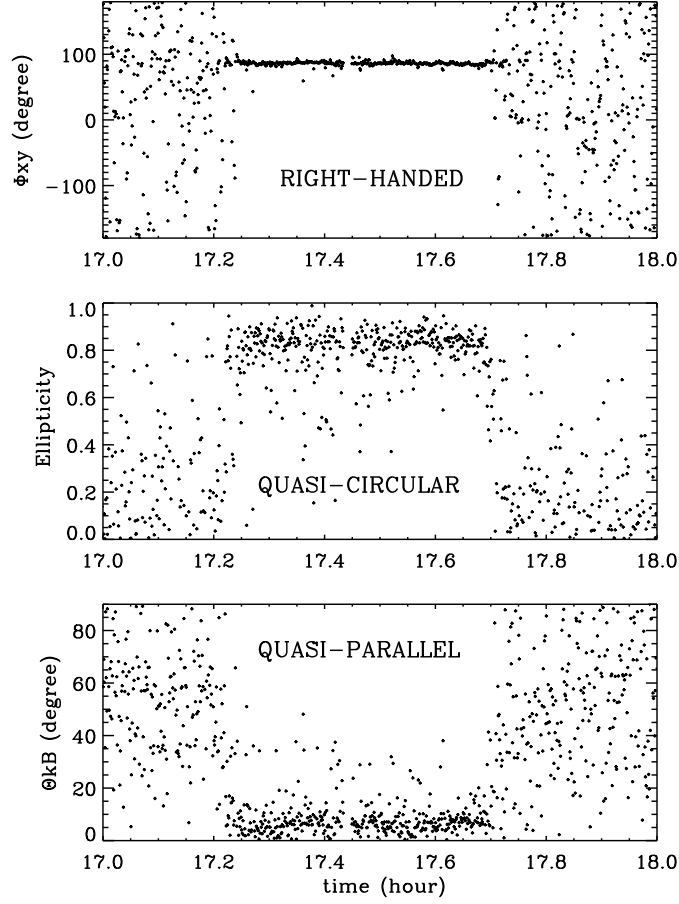
Figure 2.14: Example of polarisation and propagation properties of the observed whistler waves. Upper panel: phase difference $\Delta\Phi_{xy} = \Phi_x - \Phi_y$ during 1 h, $\Delta\Phi_{xy}$ is variable in the beginning and at the end of the time interval, and is constant ($\Delta\Phi_{xy} = 90°$) between 17:12 and 17:42 UT indicating right-handed polarisation. Middle panel: ellipticity is close to 1 during the constant phase difference interval, that corresponds to quasi-circular polarisation. Bottom panel: angle Θ_{kB} between the minimum variance direction and the mean field, indicating quasi-parallel propagation during the interval with a right-handed circular polarisation. Figure from (Lacombe et al., 2014).

connected to the Earth's bow-shock, using the Cluster/WHISPER instrument. Most of the data show the spectrum of the background turbulence discussed above. In $\sim 10\%$ of the retained data[9], the spectra have bumps between 3 Hz and 300 Hz, as is shown in Figure 2.13. The typical polarisation properties of the fluctuations for each time interval with a spectral bump is shown in Figure 2.14, where a continuous (for this case, ~ 30 min long) right handed polarisation is observed at a fixed frequency (the central frequency of the spectral bump).

In cases when the spectrum shows a break at electron scales, the polarisation generally indicates intermittent whistlers at the frequency of the break, as we have shown in (Lacombe et al., 2014) and (Roberts et al., 2017) using Cluster/STAFF-SC burst mode data, see Figures 2.15.

One can argue that whistler waves are expected to be present in the corresponding frequency range ($f \in [30, 400]$ Hz at 1 AU) and so are a part of the background turbulence at kinetic scales. As we show in (Lacombe et al., 2017), the background turbulence at kinetic scales have low frequencies $f \sim 0$ and $k_\perp \gg k_\parallel$. The narrow-band whistlers are characterized by $f \in [f_{lh}, 0.5 f_{ce}]$ and $k_\parallel \gg k_\perp$. Thus, the fact that these two phenomena are superimposed in the satellite frame is incidental. In the plasma frame they are well separated.

The generation of whistlers in the solar wind and their interaction with electrons and with the background turbulence are under debate (Lacombe et al., 2014; Kajdič et al., 2016; Stansby et al., 2016; Tong et al., 2019b,a; Krishna Jagarlamudi et al., 2020).

In (Kajdič et al., 2016), we have analysed the electron distribution functions $f(V_e)$ in the presence of quasi-parallel whistler waves and in the neighbour time intervals without whistlers. We could show that the intervals with waves have a suprathermal electron Strahl wider by $10°$ than without waves. These results make us think that parallel whistlers may be at the origin of the Strahl diffusion with increasing radial distance (Maksimovic et al., 2005). It will be interesting to verify these results with Parker Solar Probe measurements closer to the Sun and with Solar Orbiter in the inner Heliosphere.

Regarding the observability conditions and generation of quasi-parallel whistlers, we have found that the waves are observed mostly within the slow wind, $V < 500$ km/s and for a low proton thermal pressure nkT_p, i.e., when the background turbulence has a low amplitude (Lacombe et al., 2014). For fast wind and high nkT_p, the background turbulence is intense and may hide possible whistler waves. We also find that whistlers appear when there is a change in the $\mathbf{B}_0$ direction, close to the heliospheric current sheet. It is possible that in these particular cases, whistlers are generated during reconnection

---

[9]The following criteria have been applied to construct *Cluster-Kinetic-Turbulence-database*, which is used in the studies of Alexandrova et al. (2012) and Lacombe et al. (2014, 2017): (i) visual inspection of the electrostatic waves around plasma frequency measured by WHISPER allows for detection of the free solar wind time intervals not magnetically connected to the Earth's bow shock (the shock connectivity appears as intense Langmuir waves emissions at local plasma frequency); (ii) measurements of the DC magnetic field (FGM) and of magnetic fluctuations (STAFF), as well as ion and electrons moments (CIS/HIA and PEACE instruments) are available; (iii) 10 minutes of homogeneous time interval (no important changes in the plasma parameters). This selection over 5 years of Cluster mission gives us 173 time intervals with 154 examples of usual background turbulence described above and 19 intervals of long lived whistler waves, lasting at least 5 minutes within the selected 10 minutes interval.
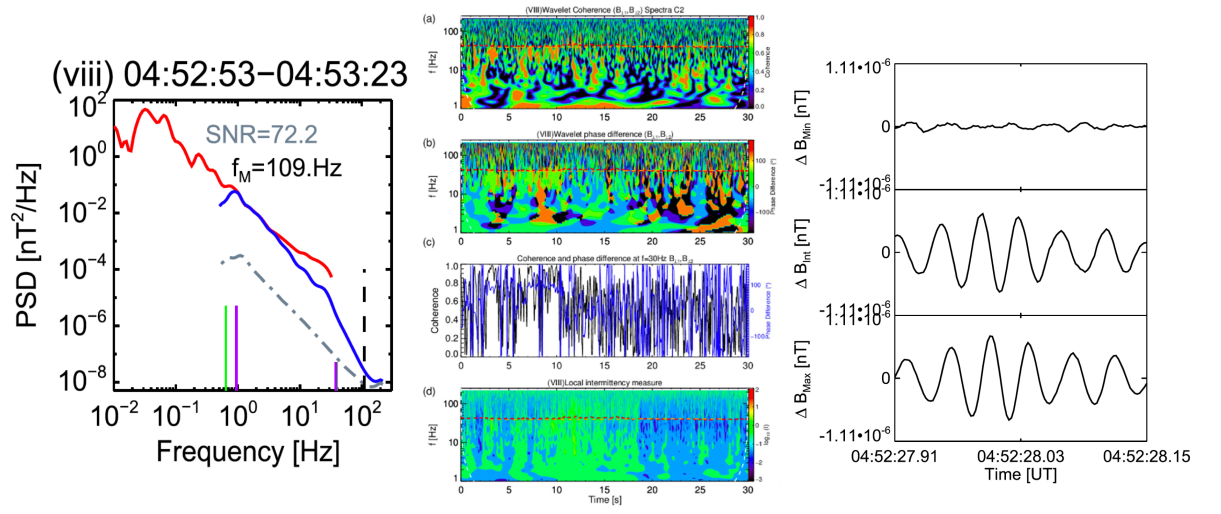
Figure 2.15: Left: Magnetic spectrum measured by Cluster/FGM (red line) and STAFF-SC in the burst mode (blue line). A clear break around electron scales ($\sim 30-40$ Hz) is observed. Middle: Wavelet analysis of $\delta\mathbf{B}_\perp$: (a) coherence between two perpendicular components of magnetic field. (b) Phase difference between two perpendicular components of $\delta\mathbf{B}$, the green colour corresponds to phase difference of $90°$ (RH polarisation); (c) A one-dimensional cut of the coherency (black) and of the phase difference (blue) at 30 Hz; (d) Local Intermittency measure. Right: The whistler waveforms, which appear around $t = 3.5$ s in the middle panel. Figures from (Roberts et al., 2017).

37

events within the heliospheric current sheet, and we observe them far from their source. The most important condition of the appearance of parallel whistlers is the presence of an electron heat flux larger than a certain threshold. Therefore, the electron heat flux instability is probably at the origine of the observed parallel whistlers at 1 AU. No evidence of the electron temperature anisotropy have been found in this study.

Recently, Tong et al. (2019b) studied solar wind whistlers with ARTEMIS spacecraft. The authors confirm that quasi-parallel whistlers can be generated by the heat flux instability. Interestingly, they show that the electron heat flux instability is affected by the temperature anisotropy of halo electrons: A slight parallel anisotropy ($T_{e,\parallel} > T_{e,\perp}$) may quench the instability, while a slight perpendicular anisotropy ($T_{e,\perp} > T_{e,\parallel}$) may significantly increase the growth rate of the the electron heat flux instability, see also (Gary and Feldman, 1977).

The radial evolution of whistlers waves in the inner Heliosphere for $R \in [0.3, 0.9]$ AU using Helios/SCM measurements have been recently studied by Vamsee Krishna Jagarlamudi during his PHD thesis, (Krishna Jagarlamudi, 2019). In (Krishna Jagarlamudi et al., 2020), we show that the whistlers signatures are mostly present in the slow wind streams, and their number increases with the radial distance R, from $\sim 3\%$ at 0.3 AU to $\sim 10\%$ at 0.9 AU. In the fast wind, spectral bumps appear for $R > 0.6$ AU and their number increases from $\sim 0.03\%$ at 0.65 AU to $\sim 1\%$ at 0.9 AU. Interestingly, the plasma follows the marginal stability path of the heat flux instability, but the radial evolution of whistlers follows the radial evolution of the core and halo temperature anisotropy. Perhaps, these are indications of the same effect found by Tong et al. (2019b), i.e., the perpendicular anisotropy ($T_{e,\perp} > T_{e,\parallel}$) of $f(V_e)$ favors the heat flux instability. Observations of Parker Solar Probe and Solar Orbiter will provide us with new elements on this puzzling problem.

Chapter 3

Coherent structures across the turbulent cascade

The previous chapter has been devoted to the spectral shape. What is *behind* the observed spectrum of background turbulence in the solar wind? What do the turbulent fluctuations which form this spectrum look like? Any turbulent flow is intermittent. Let us focus now on intermittency and coherent structures. In this chapter, first, we attempt to give a definition of a coherent structure. Then, we verify the presence of such structures in a wide range of scales of the solar wind turbulent cascade (from the energy injection to the dissipation scales). We show that all over the cascade, signatures of space-localised and scale-delocalised structures exist. We illustrate the connection between the presence of such structures, non-Gaussianity and the phase coupling in the observed signal. We analyse the topology of the structures within different frequency ranges, and we show the presence of magnetic vortices within the inertial range and at kinetic plasma scales.

Most of the studies of intermittency in turbulence are based on statistical methods. These methods show non-Gaussianity of turbulent fluctuations and the increase of this non-Gaussianity toward small scales (e.g., Sorriso-Valvo et al., 1999; Bruno and Carbone, 2013). It is well known that these statistical manifestations are due to the presence of coherent structures (e.g., Frisch, 1995).

Fiedler (1988) gives the following characteristics of coherent structures in non-magnetised flows (here is the complete quote):

1. They are typically of composite scales (i.e., they cover a range of scales), the largest scale being comparable to the lateral flow dimension.

2. They appear to be flow-specific in shape and composition, i.e., indirectly related to boundary conditions.

3. They show strong similarities with corresponding structures of the (preceding) laminar-turbulent transition.

39

4. They are, and this is their very essence, as a pattern recurrent, having a life-span typically at least the average passage time of a structure. (Cardesa et al. (2017) have recently estimated life time of eddies in 3D numerical simulations of isotropic hydrodynamic turbulence: the structures may persist up to $20\tau_{NL}$.)

5. They exhibit a high degree of organization in their structure as well as in their dynamics, their appearance is at best quasi-periodic (typically stochastically intermittent).

Farge and Schneider (2015) define coherent structures in any turbulent flow (non-magnetised and MHD) as *everything that is not noise*. This is very general, but if we apply such definition to the solar wind observations, it will include narrow-band waves, like AIC and whistlers. We do not think that events which are localized in frequency (and $\mathbf{k}$), as waves, can be classified as coherent structures.

We propose here the following definition of a *Coherent structure* in the space plasma turbulence :

- A coherent structure is a high amplitude event localized in space. This means that it is delocalized in Fourier space and it exhibits phase coupling over a large range of scales. (For the satellite *in-situ* measurements coherent structures are localized in time and delocalized in frequency, i.e., with a broad band.)

- A coherent structure has a particular topology, which yields a coupling between the components of the fields, i.e., to a particular apparent polarisation. (How this topology is related to the flow boundaries and/or original structures of the laminar-turbulent transition, as is the case in hydrodynamic turbulence, has never been studied yet in the solar wind.)

- Its life time τ_{life} is much longer than the life time of the random fluctuations at the smallest scale of the structure that is the eddy turn-over time at this scale. (As far as coherent structures cover a very large range of scales, τ_{life} is probably of the order or bigger than τ_{NL} at the largest scale of the structure.)

Let us now verify the first two points[1] for the solar wind turbulence, starting from scales larger than the inertial range, and going to the smallest resolved electron scales. For this purpose, first, we use the Wind/MAG data within one of the longest recorded slow solar wind stream (about 9 days), where we observe a f^{-1} spectrum at the lowest frequencies and most of the inertial range (dataset analysed by Vamsee Jagarlamudi during his PHD, (Krishna Jagarlamudi, 2019)). Then, we use the famous interval of Leamon et al. (1998b) to illustrate the inertial range and the ion transition range (Lion et al., 2016). To study sub-ion and electron scales we use the waveforms of the Cluster/STAFF instrument in normal and burst modes, respectively (Alexandrova et al., 2020).

---

[1]We will not address the issue of coherent structures life time here. This will be a subject of our future studies.

1 Time localisation and frequency/scale delocalisation

Figure 3.1 shows the turbulent spectrum $S_\perp(f)$ of transverse (or Alfvénic) magnetic fluctuations $\delta B_\perp$ (solid), and the spectrum $S_\parallel(f)$ of compressible fluctuations $\delta B_\parallel$ (dashed line) for a 9 days time interval in a slow solar wind stream as measured by the Wind/MAG instrument on August 9–18, 2009 (221–230 DOY). The spectra are calculated using the Morlet wavelet transform integrated over the time variable (e.g., Torrence and Compo, 1998; Alexandrova et al., 2008a; Dudok de Wit et al., 2013). The spectrum $S_\perp(f)$ displays a transition from the power-law $f^{-1.1}$ to $f^{-1.8}$ between $2 \cdot 10^{-4}$ Hz and $5 \cdot 10^{-4}$ Hz, or a break around $3 \cdot 10^{-4}$ Hz. The highest resolved frequency is about $3 \cdot 10^{-2}$ Hz, which is just below the ion cyclotron frequency $f_{ci} \simeq 4.5 \cdot 10^{-2}$ Hz, indicated by a vertical solid line. The compressible fluctuations follow nearly a Kolmogorov scaling all over the observed frequency range. However, the spectrum $S_\parallel(f)$ is not a perfect power-law within the transition frequency range of $S_\perp(f)$. This non-equal behaviour of transverse and parallel spectra is quite puzzling (but is out of the scope for the present manuscript).

The compressibility $S_\parallel(f)/S(f)$ (middle panel of Figure 3.1) exhibits a large local minimum around the break at about $3 \cdot 10^{-4}$ Hz. At higher frequencies, i.e., across the inertial range of the $\delta B_\perp$ fluctuations, the compressibility increases monotonically from 0.02 to ~ 0.1.

The two upper panels of Figure 3.1 give *averaged characteristics* of the solar wind turbulence at MHD scales within the considered slow wind stream. The bottom panel of Figure 3.1 shows *the Local Intermittency Measure* (*LIM*) introduced by Farge (1992) as

$$I(t,\tau) = \frac{|W(t,\tau)|^2}{\langle |W(t,\tau)|^2 \rangle_t}, \tag{3.1}$$

where $W(\tau,t)$ is a wavelet coefficient at time t and scale τ, and $|W(\tau,t)|^2$ is a wavelet scalogram. Thus, *LIM* is just a wavelet scalogram normalised over the mean value of energy at each scale τ. This representation allows to appreciate the texture of the turbulent fluctuations in time and scales and to see the deviation of energy of fluctuations from the mean spectrum (shown in the upper panel). The darker the colour, the lower the energy of the fluctuations. We observe that, at very large scales, there is an event around $\tau \simeq 5 \cdot 10^4$ s (~ 14 hours), lasting about 2 days (between day 2 and 4). This is probably the *trace* of a solar structure[2]. At the time scale of the spectral break, $\tau \simeq 10^4$ s (~ 3 h) there is an onset of completely different behaviour: energetic events localised in time appear and continue all down the inertial range up to the smallest resolved scale. We observe here the phenomenon of time localisation and scale delocalisation, one of the properties of coherent structures.

Let us now move to smaller scales ($\tau < 10^2$ s) and see if this tendency continues down to the end of the inertial range and at kinetic plasma scales.

Figure 3.2 shows the spectra and the compressibility level (on the left). On the right, there are the Morlet wavelet scalograms of $\delta B_\perp$ (right, upper panel) and of $\delta B_\parallel$ (middle

---

[2]Could this be a signature of supergranulation, whose lifetime is approximately twice the observed scale $\simeq 10^5$ s (e.g., Velli, 2003)?
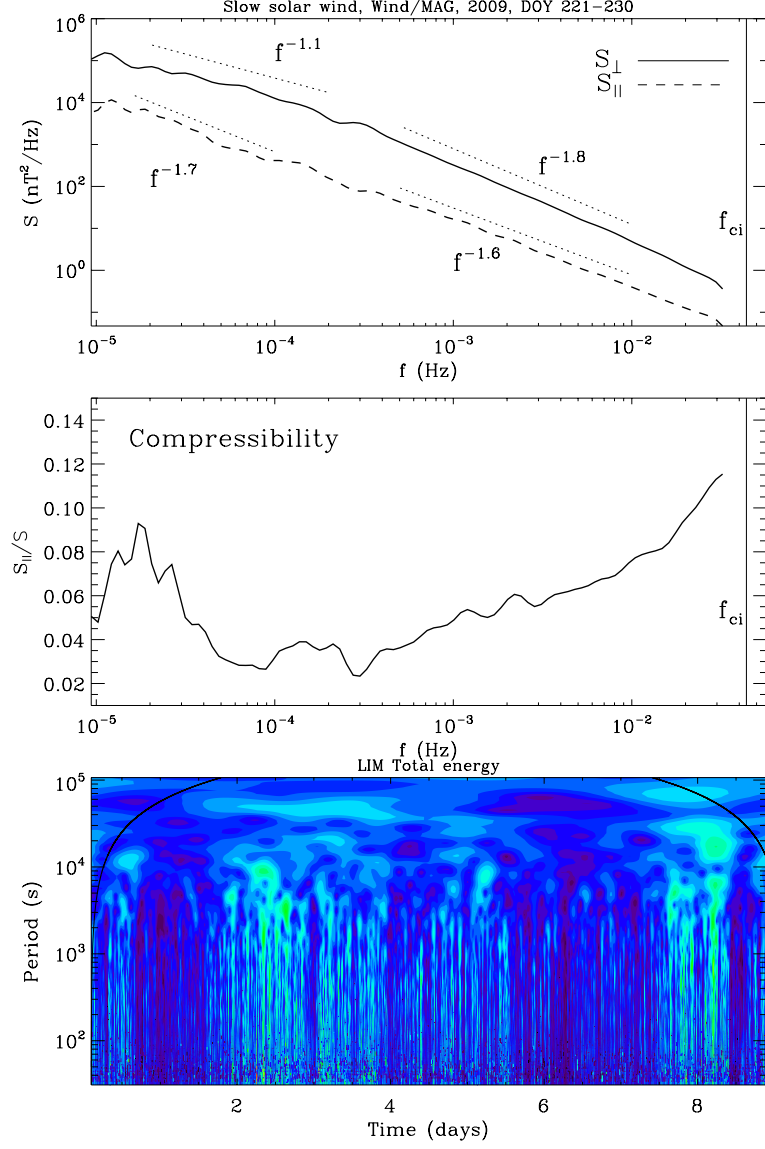
Figure 3.1: Time interval of 9 days within the slow wind as measured by Wind/MAG, analysed by Jagarlamudi et al. (2019). Upper panel: PSD of $\delta B_\perp$, $S_\perp$ (solid line), PSD of $\delta B_\parallel$, $S_\parallel$ (dashed line); Middle: Compressibility level $S_\parallel(f)/S(f)$ of the fluctuations as a function of the satellite frame frequency; Bottom: Local Intermittency Measure (LIM) of the total energy of the magnetic fluctuations.
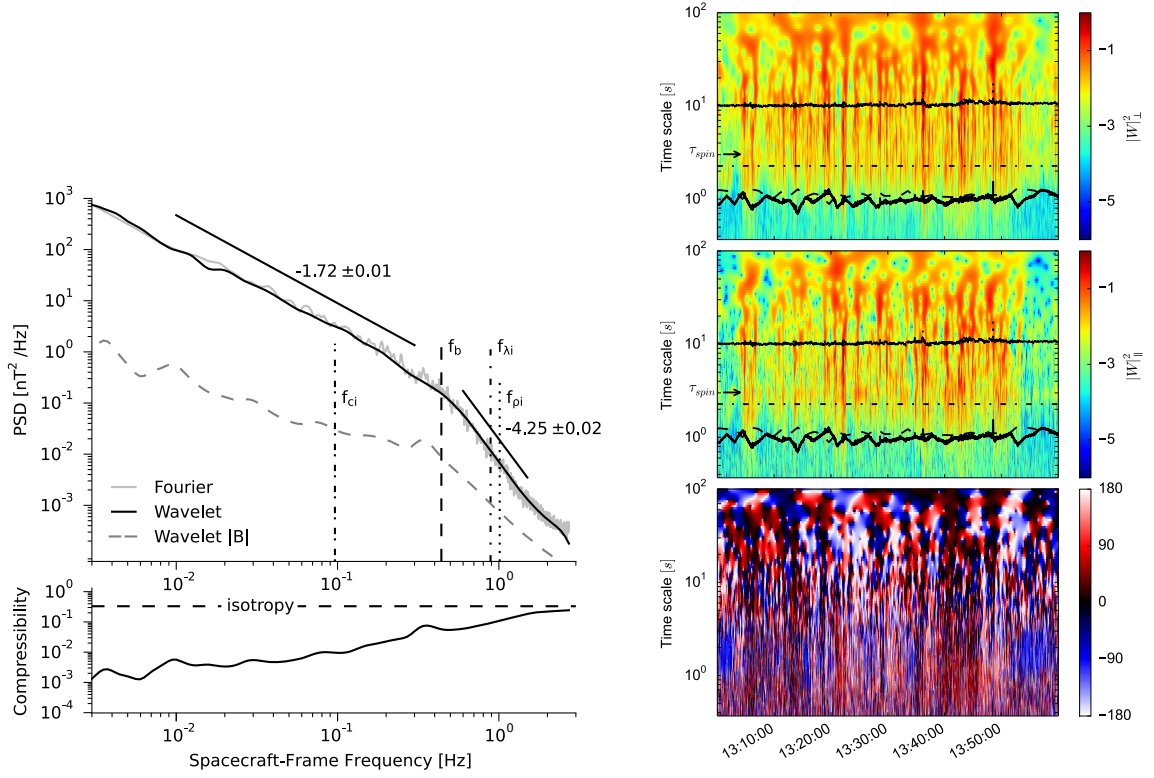
Figure 3.2: Left: Magnetic turbulent spectrum measured in a fast wind stream by Wind/MAG on the January 30, 1995, between 13:00 et 14:00 UT. The total energy (solid line) follows an $f^{-1.7}$ power-law within the inertial range and has a very steep spectrum (close to f^{-4}) at ion scales. The bottom panel shows the compressibility on the same way as in Fig. 3.1. Right: scalograms normalised by the Kolmogorov scaling ($\tau^{-1.7}$) of $\delta B_\perp$ (upper panel) and of $\delta B_\parallel$ (middle panel) are shown with a colour code; in both scalograms, the cyclotron period is the solid curve around $\tau = 10$ s; the ion break time scale $\tau_b = 2.3$ s (corresponding to $f_b \simeq 0.44$ Hz) is indicated by a horizontal dashed-dotted line; two curves below $\tau = 1$ s are the Doppler shifted ρ_i (dashed) and λ_i (solid). The bottom panel shows the polarisation of the magnetic fluctuations in the plane (x, y) perpendicular to $\mathbf{B_0}$, the left-hand polarisation is indicated by blue, and the right-hand polarisation is in red. A left-hand-emission is observed at the ion break time scale τ_b in the beginning and at the end of the time interval. Courtesy of Sonny Lion, 2015, see also (Lion et al., 2016).

43

Figure 3.3: Left: Spectrum of magnetic fluctuations in the slow solar wind from ion to sub-electron scales (Cluster/STAFF-SC and SA measurements). Right: $\delta B_x(t)$ as measured by STAFF-SC in normal mode (up to 12.5 Hz) in Geocentric solar ecliptic (GSE) reference frame, scalogram and *LIM* of $\delta B_x(t)$ from ion and to sub-ion scales (waveforms 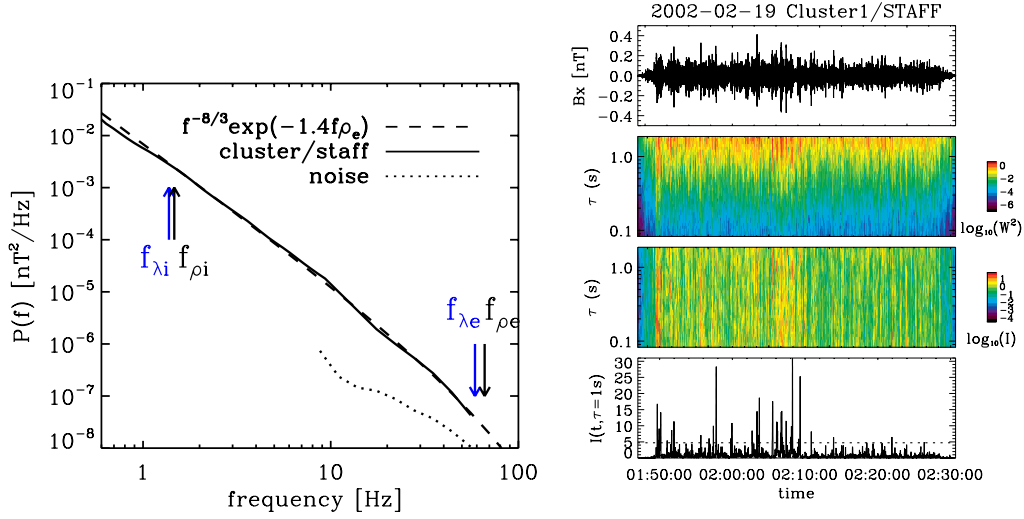at electron scales are not measured for this time interval). The bottom panel gives *LIM* for a fixed scale $\tau = 1$ s. Figure from Alexandrova et al. (2020).

panel), normalized by $\tau^{-1.7}$, for scales covering two decades of the inertial range and more than one decade around ion scales. The bottom panel on the right gives informations on the polarisation of the magnetic fluctuations in the plane (x, y) perpendicular to the mean field $\mathbf{B_0}$ during the considered time interval of a fast stream (Leamon et al., 1998b; Lion et al., 2016). In the three scalograms, one observes the energetic events localised in time which cover all the observed scales in the inertial range; they 'cross' the ion break scale $\tau_b = 1/f_b$ (horizontal dashed-dotted line at 2.3 s) and become less visible at scales smaller than ρ_i and λ_i (black solid and dashed curves below $\tau = 1$ s). The normalization of the scalograms by the inertial range scaling gives the impression that the two spatial ion scales ρ_i and λ_i (which are close to each other for this time interval) are the smallest scales of most of the localised energetic events of the inertial range. However, from the polarization map (bottom panel on the right), there are no changes across the ion scales for the localized events: one observes vertical lines up to the smallest resolved scale, except for time intervals where left-handed waves are present. Let us consider now smaller scales.

Cluster/STAFF (Cornilleau-Wehrlin et al., 1997) is the most sensitive instrument by today to measure the sub-ion scales in the solar wind. Figure 3.3 shows STAFF measurements at kinetic scales for a slow wind time interval of 45 minutes on February 2, 2002. The left panel gives the spectrum of the total energy of magnetic fluctuations from ion and up to electron scales. One observes here the general spectrum as described in the previous chapter. The exact fitting to this spectrum in the frequency domain gives $P(f) \sim f^{-8/3} \exp\left(-1.4 f/f_{\rho_e}\right)$, with $f_{\rho_e} = V/2\pi\rho_e$. The right panel shows from

top to bottom: (i) the original $B_x(t)$ signal as measured by STAFF-SC in normal mode, i.e., $f \in [0.1, 12.5]$ Hz; (ii) its Morlet wavelet scalogram; (iii) its Local Intermittency Measure, LIM, $I(t, \tau)$ (see Equation (3.1)) and (iv) LIM for a fixed time scale $\tau = 1$ s as a function of time. LIM (in the 3rd panel on the right) shows the same tendency as in the inertial range: localised energetic events exist and cover all the observed scales. Unfortunately, for this time interval, the STAFF instrument was in normal mode and could not measure the waveforms up to the electron scales. To complete the study, we analysed burst mode STAFF-SC data[3]. We found a continuation of the localised events up to the electron scales $\tau \simeq 0.01$ s (not shown).

To conclude, starting at the spectral break between f^{-1} and $f^{-5/3}$, i.e., at a time scale around 3 hours and going to electron scales, $\tau < 0.1$ s, all over the cascade we observe time localised energetic events covering all the observed scales (or frequencies). Is there a reset of these events at ion scales or do the same structures continue at smaller scales? This will be a subject of a future study. Here we just note the observational fact that for randomly chosen time intervals in slow or fast solar wind streams, the same tendency of time localisation of the energy and its scale/frequency delocalisation is observed at all scales across the cascade.

Below, we address the issue of how this time localisation and frequency delocalisation relates to phase coupling across scales and non-Gaussianity of turbulence fluctuations.

2 Phase coupling and non-Gaussianity

To approach this problem, we use an idea of Hada et al. (2003) and Koga and Hada (2003), who compared the observed signal and surrogate random and constant phase signals. The upper panel of Figure 3.4 shows from left to right: (i) the same signal $B_x(t)$ as in Figure 3.3, (ii) its Fourier spectrum between 0.5 and 12.5 Hz, and (iii) its phase as a function of the measured frequency. In the middle panels we have the same representation but for a random phase signal $B_{x,r}(t)$ constructed as follows: we keep the Fourier amplitudes of the observed signal, we resample phases uniformly and randomly and then we perform the inverse Fourier Transform. In the bottom panels the constant phase surrogate signal is shown: it is obtained by fixing all phases to 90°, giving a coherent high-amplitude event in the middle of the time domain. A zoom on this event is shown in the Laurea Thesis of Claudia Rossi (2011). Let us now compare statistics for these three signals.

Figure 3.5 (Left) shows the probability distribution functions (PDFs) of the normalised magnetic fluctuations $\delta B_x / \sigma_x$ (σ_x being the standard deviation of δB_x at a given scale τ) at 3 different scales $\tau = 0.08$, 0.16 and 0.64 s and for the 3 signals, original and two surrogate. One observes non-Gaussian distributions for the original signal, with increasing of tails toward small scales (upper panels), as expected for an intermittent turbulence. Middle panels reveal the connection between Gaussianity and phases: the distributions for the random phase signal are completely Gaussian at all scales. The

---

[3]See http://sci.esa.int/cluster/55616-guest-investigator-operations-2015-2016/
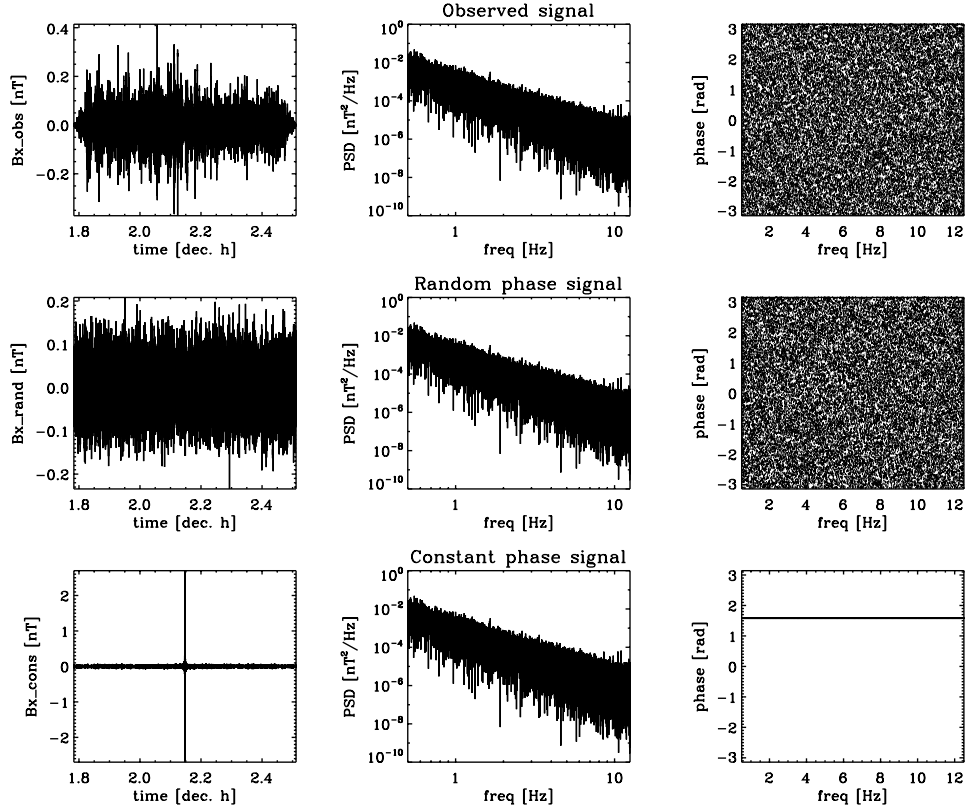
Figure 3.4: Upper panels: Original signal B_x as measured by Cluster/STAFF-SC for the same time interval as in Figure 3.3, its Fourier spectrum and phases. Middle panels: the same representation as in the upper panels, but for the uniform random phase signal. Bottom panels: the same for the constant phase signal. Figure from (Claudia Rossi, Thesi di Laurea, 2011).
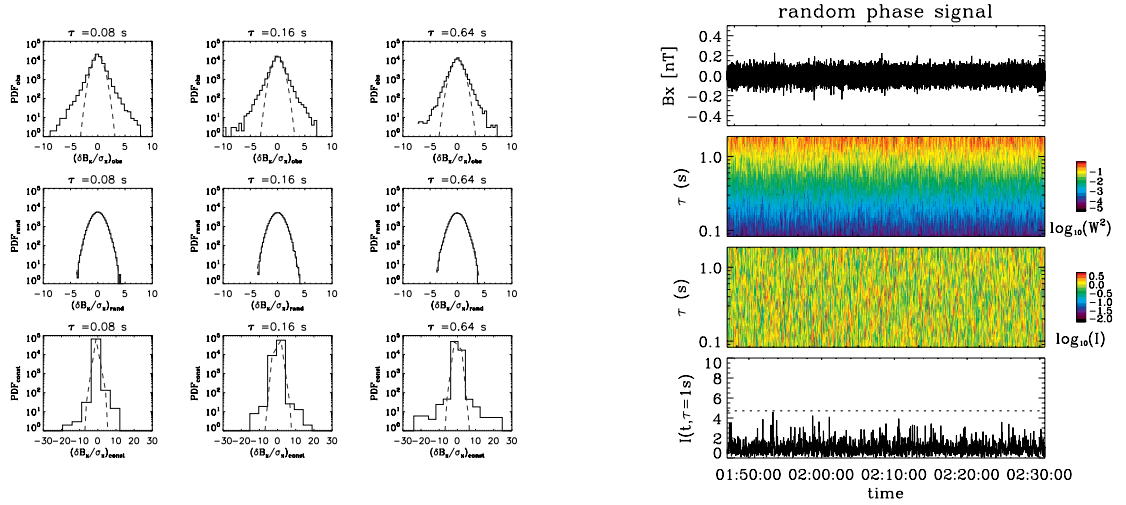
Figure 3.5: Left: Upper panels: PDFs for the measured signal B_x at 3 time scales. Middle panels: the same representation as in the upper panels, but for the random phase signal. Bottom panels: the same for the constant phase signal. Figure from (Claudia Rossi, Thesi di Laurea, 2011). Right: Random phase signal and its scalogram and *LIM* represented in the same way as in Figure 3.3 (Right).

constant phase signal shows PDFs with very heavy tails (bottom panels). Therefore, the original signal (upper panels) might be a combination of coherent events with coupled phases, and random phase fluctuations. This will give statistics between the two considered limits. In other words, the solar wind turbulence contains fluctuations with coupled phases that are at the origin of the non-Gaussian tails of the PDFs.

Figure 3.5 (Right) shows the same information as Figure 3.3 (Right) but for the random phase signal. From the time series of the random phase signal (upper panel in Figure 3.5 (Right)) and its *LIM* at a fixed scale $\tau_0 = 1$ s (bottom panel), it becomes clear that by randomising phases, we *kill* all high amplitude events. Thus, it seems that phase coupling leads to high amplitude events. From the scalograms of wavelets and *LIM* (2nd and 3d panels in Figure 3.5 (Right)), we observe a completely homogeneous energy distribution in time and scales. Therefore, by proof of the opposite, all time localised and scale delocalised energetic events observed in scalograms of Figures 3.1, 3.2 and 3.3, from the beginning of the inertial range down to the sub-ion scales, correspond to events with coupled phases which are at the origin of non-Gaussianity and intermittency.

So, we have shown the relation between phase coupling, time localisation and scale delocalisation, and non-Gaussianity of the fluctuations. Indeed, by making a noise from the observed turbulent signal, we destroy all these properties. Here, we agree with Farge and Schneider (2015) who define coherent structures as *everything that is not noise*. Now, let us verify the topology of these localised energetic events with coupled phases.

3 Topology of the structures

What do the coherent structures look like? To answer this question, let's go back to the physical space and consider the magnetic field and its fluctuations at different scales.

Fluctuations at time scales smaller or equal to τ for a j's component of the field are defined as

$$\delta B_j^\tau(t) = B_j(t) - \langle B_j(t)\rangle_\tau, \tag{3.2}$$

where $\langle.\rangle_\tau$ is the moving average with a window of size τ. This definition is equivalent to a high-pass filter for $f \geq 1/\tau$. The low-pass filter for $f < 1/\tau$ is just the smoothed field

$$B_j^\tau(t) = \langle B_j(t)\rangle_\tau. \tag{3.3}$$

The band-pass filter between frequencies $f_1 = 1/\tau_1$ and $f_2 = 1/\tau_2$ can be defined as

$$\delta B_j(t) = \langle B_j(t) - B_j^{\tau_1}(t)\rangle_{\tau_2} = \langle \delta B_j^{\tau_1}(t)\rangle_{\tau_2}, \tag{3.4}$$

with $\tau_1 > \tau_2$.

Large scales: from f^{-1} to $f^{-5/3}$

The largest resolved scales have been discussed in the beginning of Section 1 of this chapter; see Figure 3.1, where we show the spectrum and the intermittency measure, *LIM*, for the time interval of 9 days of continuous slow solar wind. Let us now only consider the second day of this time interval to see in more details the magnetic field at different time scales (or frequency ranges). Figure 3.6(a) shows the components of the magnetic field $\mathbf{B}(t)$ for this particular day. The panels below, show $\mathbf{B}(t)$ for different frequency ranges.

Based on the spectrum and *LIM* of Figure 3.1 upper and lower panels, respectively, and using Equations (3.2–3.4), we separate $\mathbf{B}(t)$ into (i) a smoothly varying field of the f^{-1}–range (for $f < 10^{-4}$ Hz), see Figure 3.6(b), (ii) fluctuations defined between $f_1 = 10^{-4}$ and $f_2 = 5 \cdot 10^{-4}$ Hz, i.e., around the break at $f_b \simeq 3 \cdot 10^{-4}$ Hz, see panel (c), and (iii) $\delta \mathbf{B}(t)$ within the inertial range, i.e. for frequencies $f > 10^{-3}$ Hz, see panel (d).

For the scales of the break, in panel (c), the magnetic structures last several hours ($\sim 4 - 6$ hours), and look like a sequence of flux ropes or vortices (see below). Their amplitude $\delta B/B_0$ is about 1, as expected for fluctuations at the break scale (Matteini et al., 2018). Within the inertial range, the fluctuations are very intermittent with a number of high amplitude events: a 30 minutes zoom around one of such event with $\delta B/B_0 \sim 1$ is shown in the bottom panel of Figure 3.6, and it looks like a current sheet (see below). Let us now consider the inertial range structures in more details.

Inertial range and ion transition

As discussed above, the inertial range is filled with structures localised in time and delocalised in frequencies, with the smallest scales around the ion scales. Indeed, Lion et al. (2016) performed the phase coherency analysis of the time interval shown in Figure 3.2.
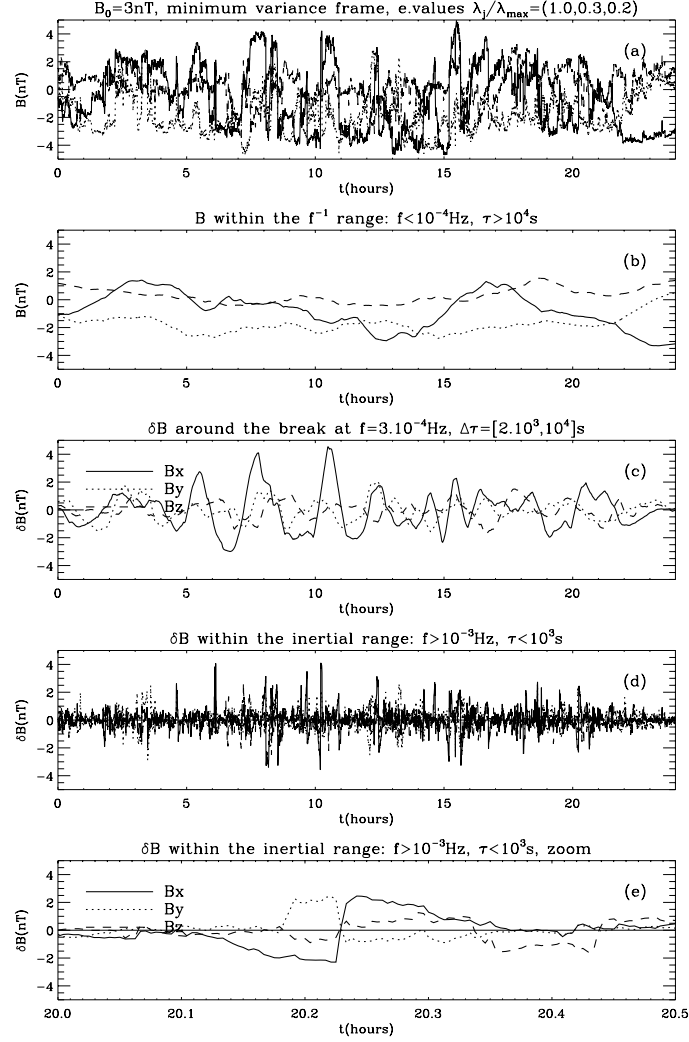
Figure 3.6: $\mathbf{B}(t)$ (in the minimum variance frame) within the slow wind stream, which is characterised by the spectrum shown in Figure 3.1: (a) raw measurements: B_x (solid line) is the maximum variance component, B_y (dotted) is the intermediate, B_z (dashed) is the minimum variance component. The normalised eigenvalues are $\lambda_j/\lambda_{max} = (1, 0.3, 0.2)$, i.e., fluctuations are mostly linearly polarized. (b) $\delta\mathbf{B}(t)$ within the f^{-1} spectral range (low-pass filtered $\mathbf{B}(t)$ for $f < 10^{-4}$ Hz). (c) $\delta\mathbf{B}(t)$ at scales around the break scale, $f \in [10^{-4}, 5 \cdot 10^{-4}]$ Hz. (d) $\delta\mathbf{B}(t)$ within the inertial range. (e) A 30 minutes zoom of the panel (d) around one of the coherent structures.

49
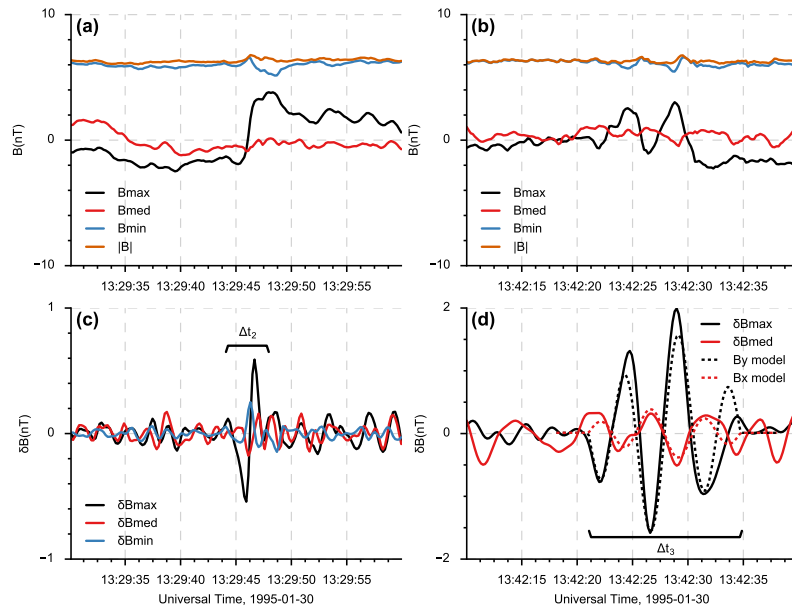
Figure 3.7: Upper panels: Wind/MAG measurements around two localized events, in time intervals of 30 seconds. Bottom panels: Fluctuations $\delta\mathbf{B}$ defined at scales around the ion break scale, in panel (c) band pass filter is applied between 0.4 and 1 Hz, in (d) – between 0.1 and 0.5 Hz. Figure from (Lion et al., 2016).

This analysis reveals that the structures present at the ion break scale have a filling factor of 40% in time (or space) and cover a wide range of scales, from $4 \cdot 10^{-2}$ Hz to 1 Hz that corresponds to $\tau \in [1-25]$ s and spatial scales of the order of $\ell \in [0.5-20] \cdot 10^3$ km $\simeq [5-200]\rho_i = [4-160]\lambda_i$.

Figure 3.7 (upper panels) shows the magnetic field around two of such events: in panel (a) we observe a strong gradient in one of magnetic field components; usually such a variation is interpreted as a current sheet. In panel (b), we have waveforms inherent to a magnetic vortex or a flux rope[4].

Figure 3.7 (bottom panels) show magnetic fluctuations around ion scales. The fluctuations within the current sheet (defined between 0.4 and 1 Hz, panel c) do not cross zero at the same time. It seems that, at ion scales, the substructure of the large scale current sheet looks more like a small flux rope or a vortex than a smaller scale current sheet.

In panel (d) of Figure 3.7, the magnetic fluctuations within the frequency range $[0.1-0.4]$ Hz can be compared with the Alfvén vortex model shown by dotted lines (Petviashvili and Pokhotelov, 1992; Alexandrova, 2008). Unfortunately, on Wind spacecraft, the time resolution of the ion moments, and thus of the velocity fluctuations $\delta\mathbf{V}$, is not good enough to verify the alignment between $\delta\mathbf{B}_\perp$ and $\delta\mathbf{V}_\perp$, which is the property that distinguishes the Alfvén vortex from the magnetic flux-rope.

Another issue with Wind is that it is a mono-satellite. To confirm the space localization of magnetic vortex signatures in the solar wind, 4 satellite measurements are needed. We have done such analysis in detailed case studies in the slow and fast wind streams using Cluster data, see (Roberts et al., 2016) and (Perrone et al., 2016, 2017).

Alfvén vortices will be discussed in more details in Chapter 4. Now, let us follow the localised energetic events down the cascade, toward sub-ion and electron scales.

Kinetic scales

At plasma kinetic scales, $\delta B/B_0$ is so small that an approach based on a mixture of weakly interacting waves (wave turbulence) seems applicable. However, as we have shown above (Section 1), these scales are filled with signatures of coherent structures: energetic events localised in time and delocalised in scales.

Figure 3.8 shows magnetic fluctuations around one of the energetic events, observed as a vertical line in LIM in Figure 3.3 and detected by the 4 satellites of Cluster (see the 4 panels): in the centre of the 4 s–time interval we find coherent fluctuations with $\delta B/B_0 \simeq 0.1 - 0.2$ depending on the satellite. The time delays between the satellites are consistent with a space localised cylindrical magnetic vortex at spatial scales of the order of the inter-satellite separations (~ 200 km) and which slowly propagates ($\sim 0.4V_A$) in the plasma frame quasi-perpendicularly to $\mathbf{B_0}$. The difference of amplitude of the fluctuations detected by the different satellites indicates that the four satellites

---

[4]The magnetic field of an Alfvén vortex is similar to the field of a flux rope, usually approximated by the force-free current. The difference between them is alfvénicity: within a vortex magnetic fluctuations are aligned with velocity ones (see Chapter 4).

crossed the vortex with slightly different trajectories, that is in agreement with the space localisation of the structure.

To resolve electron scales, we consider the data obtained during the Cluster Guest Investigator campaign of O. Alexandrova (2015-2016) [5]. The only available data in the free solar wind during this campaign is in the slow wind ($V \simeq 330$ km/s) on February 15, 2015. This time interval looks like any other typical solar wind turbulence, but here Cluster 3 and Cluster 4 were only 7 km apart, and the time resolution is 0.0028 s (i.e., 360 vectors per second), which allow us to resolve electron scales in the solar wind in space and in time simultaneously, for the first time[6].

The shape of the coherent structures at such small scales resembles magnetic vortices as well. An example of such an electron-scale magnetic vortex detected on two close satellites (Cluster 3 and Cluster 4) is shown on Figure 3.9: the duration of the crossing of such a vortex is about 0.05 s. The strongest gradient within this structure is localised within about 0.01 s, which corresponds to a spatial scale of about 3 km, i.e., several electron Larmor radii ρ_e. Note that this is the first time that such small-scale vortices are found in the solar wind. They can be interpreted by the theory of electron-scale vortices in high-β plasmas in the presence of electron temperature anisotropy (Jovanović et al., 2015). Similar structures have been found in 2D Particle-in-cell (PIC) numerical simulations (Haynes et al., 2015) and in the Earth's plasma sheet (Sundberg et al., 2015); bigger magnetic vortices ($\sim 30\rho_e$) have been recently detected by MMS in the Earth's magnetosheath (Huang et al., 2017).

How general are these results at 1 AU? We have analysed in the same way a dozen of hours in the free solar wind between 2001 and 2006 under different plasma conditions and we have always found signatures of coherent structures at kinetic scales. Then, we have done a visual check of many random samples of STAFF measurements from 19 years of Cluster mission on the Cluster Quicklook (Fields & Waves). Signatures of coherent structures, i.e., time localised and frequency delocalised energy enhancements, were always present in the spectrograms while Cluster is in the free solar wind. Thus it seems that presence of coherent structures is the typical situation at kinetic scales at 1 AU. Results on kinetic scale structures are summarized in (Alexandrova et al., 2020).

4   Concluding remarks

In this chapter, we show that time localised and frequency delocalised energetic events are signatures of coherent structures. In the solar wind, such signatures are observed all over the turbulent cascade, starting at the onset of the inertial range, and going up to the electron scales.

The topology and dimension[7] of coherent structures seems to vary. Scales of the onset

---

[5]See `http://sci.esa.int/cluster/55616-guest-investigator-operations-2015-2016/`.

[6]Unfortunately, MMS/SCM measurements are not sensitive enough to resolve kinetic turbulence in the solar wind.

[7]We can define the dimension of coherent structures as three minus the dimension of the symmetry group of the structure. For example, a cylindrical structure is an invariant under translation along one

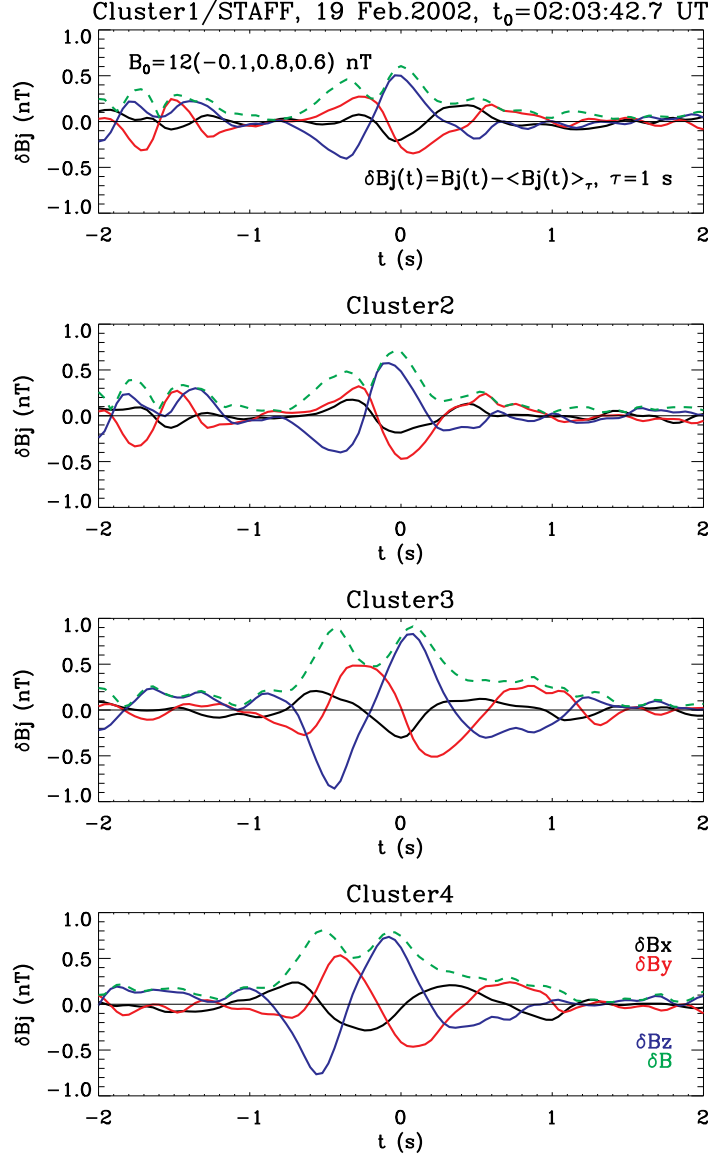Figure 3.8: A vortex-like structure at sub-ion scales observed by the four Cluster satellites with inter-separation distances of about 200 km, during the time interval of Figure 3.3. Magnetic field components are in the GSE frame. Such magnetic fluctuations correspond to current filaments localised in the centre of each structure with a cross section of the order of ion scales. Figure from Alexandrova et al. (2020).
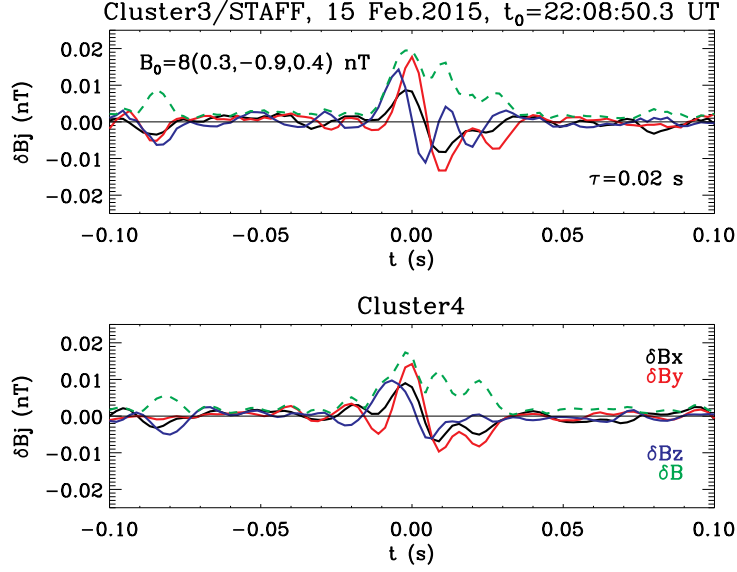
Figure 3.9: Electron scale vortex-like structure crossed by two satellites of Cluster, 7 km apart (Cluster Guest Investigator Operations of 2015); here the time interval is 20 times shorter than in Figure 3.8. Such magnetic fluctuations correspond to current filaments with a cross section of the order of several ρ_e. Figure from Alexandrova et al. (2020).

of turbulence are probably dominated by flux ropes (or magnetic vortices) (Borovsky, 2008). Large scale planar discontinuities are present within the inertial range (Veltri and Mangeney, 1999; Salem, 2000; Mangeney et al., 2001). Vortex filaments seem to co-exist with the current sheets within the inertial range and to dominate within the kinetic range (Perri et al., 2012a; Greco et al., 2016; Lion et al., 2016; Roberts et al., 2016; Perrone et al., 2016, 2017; Alexandrova et al., 2020). The time intervals analysed here for the illustration of different frequency ranges are more or less randomly chosen. We need to do a more systematic study to reach firm conclusions.

What is the filling factor of different type of the structures, and how it varies with radial distance from the Sun, will be subjects of our future studies.

---

dimension (along its axis), and variations are important only in two other dimensions, we call it 2D structure (3−1). A plane structure, like a current sheet or a shock, is invariant in the plane, so their dimension is one (3−2). In reality, infinitely long magnetic vortices are probably do not exist and a finite parallel to the field length appears. Still, $\ell_\parallel \gg \ell_\perp$, but probably the derivative along the vortex axis is not zero, so the structure can be considered as 3D. The same perhaps true for the current sheets with finite size within the plane and thus, they can be considered as 2D or even 3D structures.

Chapter 4

Alfvén vortices as building blocks of the space plasma turbulence?

As we have just seen in the previous chapter, Alfvén vortices or vortex-like fluctuations seem to cover all observable scales, i.e., from the large scale spectral break, between f^{-1} and $f^{-5/3}$, down to electron scales.

By today, the most studied Alfvén vortices are at small scales of the inertial range, and down to ion scales (Alexandrova et al., 2006; Alexandrova, 2008; Alexandrova and Saur, 2008; Lion et al., 2016; Roberts et al., 2016; Perrone et al., 2016, 2017; Wang et al., 2019). The first observations of nearly incompressible Alfvén vortices at these scales have been done by Alexandrova et al. (2006) in the quasi-perpendicular Earth's magnetosheath. Thanks to the multi-satellite measurements of Cluster it was possible to show the space localisation of these structures in the plane perpendicular to $\mathbf{B_0}$, i.e, $\ell_\perp < \ell_\parallel$. The plasma is nearly incompressible within the vortices, even if the surrounding plasma can be compressible in the Earth's magnetosheath, see Figure 1 from (Alexandrova, 2008), shown below in Figure 4.4.

Later, using Cassini/MAG magnetic field measurements, Alexandrova and Saur (2008) have shown that signatures of such vortices are also present in the quasi-perpendicular magnetosheath of Saturn, see Figure 4.5. These observations of Alfvén vortices with a radius $a = \ell_\perp \simeq 10\lambda_i \sim 10\rho_i$ in planetary magnetosheaths made us think that they are inherent to the shock physics, see discussions in the review part of (Alexandrova, 2008), where we compare magnetosheath and solar wind turbulence.

However, our recent multi-satellite studies in the solar wind (Roberts et al., 2016; Perrone et al., 2016, 2017), showing the existence of such structures in slow and fast streams, indicate that magnetic vortices are generally present in space plasma turbulence. Figure 4.1, from (Roberts et al., 2016), shows an example of an Alfvén vortex in the slow solar wind as observed on the four Cluster satellites (the dotted lines are the fitting of the model, with different closest approaches for the different satellites).

Indeed, these structures are more frequently observed than current sheets. In a case study of the fast wind (Perrone et al., 2017), we found only a few isolated current sheets (6 events among 138), the rest of the intermittent events being vortices (isolated or in a
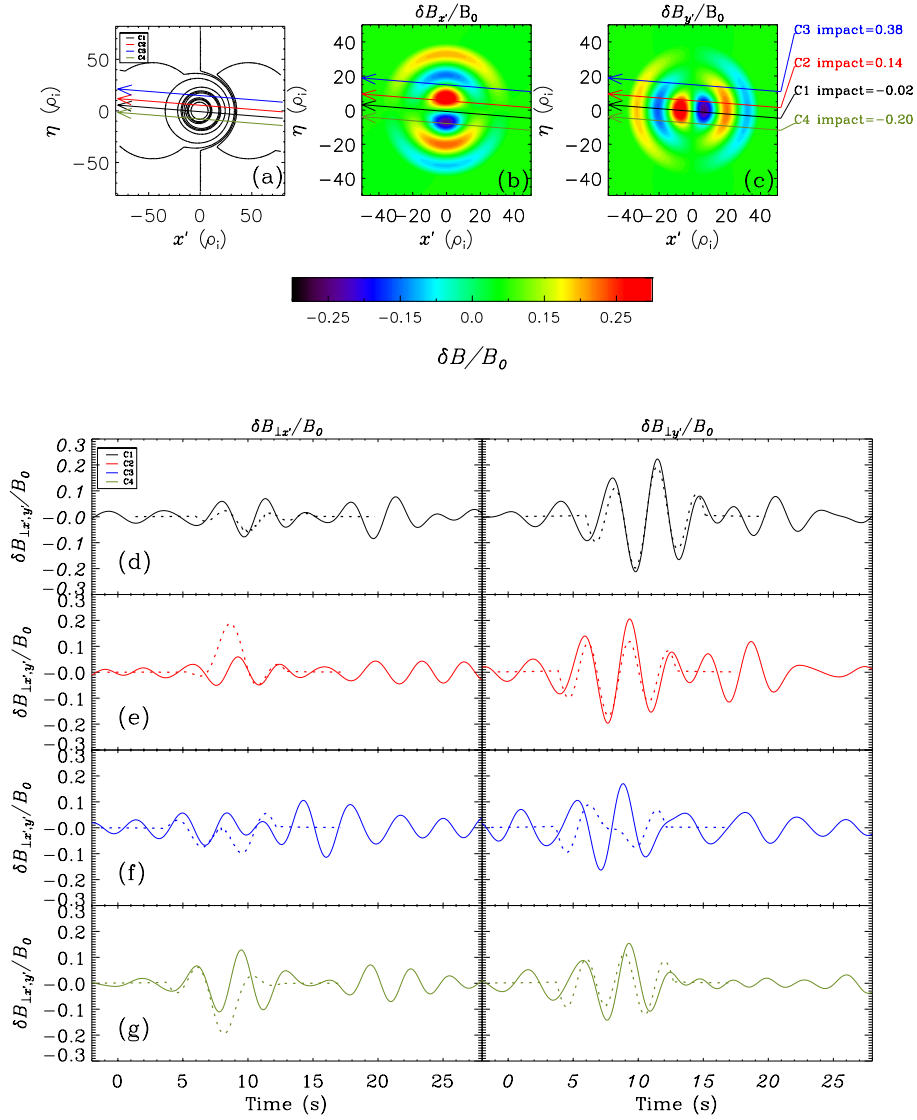
Figure 4.1: (a) The magnetic field lines of a quasi-monopolar Alfvén vortex, i.e, nearly aligned with $\mathbf{B}_0$ (the angle between the axis and $\mathbf{B}_0$ is $0.35°$). (b and c) The perpendicular magnetic fluctuations due to the vortex. The arrows denote the paths of the spacecraft through the vortex which give the modelled fluctuations in Figures 4d–4g. The impact parameters for the various spacecraft are given in units of vortex radius and denote the distance from the vortex axis (in the centre of the (a-c) panels). The spacecraft trajectories are denoted by arrows. (d–g) The observed fluctuations (solid lines) and the modelled fluctuations (dashed lines) which correspond to the trajectories presented in panels (a–c). The left column shows δB_x and the right one shows the δB_y for the four satellites (C1, C2, C3 and C4) of Cluster. Figure from (Roberts et al., 2016).

56

network). Very often, on the boundaries of the vortices or during a central pass through a dipole vortex, we observe a signal which can be interpreted as a current sheet crossing.

Another case study of a slow solar wind confirms the dominance of the vortices over different types of intermittent events, like current sheets, magnetic solitons, holes and shocks, as we found in (Perrone et al., 2016). Indeed, in the slow wind, the ion plasma β_i can be larger than or equal to 1, and compressible structures with $\delta B_\parallel \gg \delta B_\perp$, such as shocks, magnetic holes and solitons, are present; moreover, the vortices, which are characterised by $\delta \mathbf{B}_\perp$, have a non-negligible compressible component $\delta B_\parallel \neq 0$ (Perrone et al., 2016).

An incompressible hydrodynamic vortex was first described by Lamb (1895, 1906) and Chaplygin (1903) independently. Its magnetic counterpart, the classical Alfvén vortex, was introduced by Petviashvili and Pokhotelov (1992). The Alfvén vortex model is based on incompressible non-linear quasi-bidimensional MHD equations of Kadomtsev and Pogutse (1974) and Strauss (1976).

Solar wind plasma is nearly incompressible when $\beta < 1$, however, it become more and more compressible while β increases. Recently, we have proposed the first Alfvén vortex model for the plasma with $\beta \sim 1$ (Jovanovic et al., 2020). The model is rather complex but the topology of the vortex solution is very similar to the incompressible case, the principal difference is the presence of a compressible part $\delta B_\parallel$ within the vortex core resulting from the pressure balance. For more details we refer the reader to the article (Jovanovic et al., 2020).

Below we summarize the basic equations of Petviashvili and Pokhotelov (1992), which admit fluid Alfvén vortices as solutions. Then, we discuss these solutions in light of the interpretation of the spacecraft data, such as waveforms, polarisation and coherency analysis, as well magnetic spectra.

1 Fluid Alfvén vortex model

The Alfvén vortex is a non-linear solution of the ideal incompressible MHD equations in some approximation regime. It is characterized by magnetic field and velocity fluctuations mostly perpendicular to the unperturbed magnetic field $\mathbf{B_0}$ (taken here as parallel to the z direction), $\delta B_z \ll \delta B_\perp$ and $\delta V_z \ll \delta V_\perp$; they have a slow time dependence, $\partial_t \ll \Omega_{ci}$, and their space variations verify $\partial_z \ll \nabla_\perp$ (i.e., $k_\perp \gg k_\parallel$). Their amplitude $\varepsilon \sim \delta B_\perp / B_0$ is assumed to be small although finite, $0 < \varepsilon < 1$ and they satisfy the following scaling relations:

$$\frac{\partial_z}{\nabla_\perp} \sim \frac{\partial_t}{V_A \nabla_\perp} \sim \frac{\delta B_z}{\delta B_\perp} \sim \frac{\delta V_z}{\delta V_\perp} \sim \frac{\delta B_\perp}{B_0} \sim \frac{\delta V_\perp}{V_A} \sim \epsilon. \tag{4.1}$$

Neglecting all terms of order ϵ^3, the transverse fluctuations can then be described by two scalar functions, the parallel component of the vector potential A_z and a flux function ψ

$$\delta \mathbf{B}_\perp = \nabla A_z \times \mathbf{z}, \quad \delta \mathbf{V}_\perp = \mathbf{z} \times \nabla \psi \tag{4.2}$$

(in the following the symbol δ will be omitted).

For the scalar variables A_z and ψ the MHD equations

$$\rho(\partial_t + \mathbf{V} \cdot \nabla)\mathbf{V} = -\nabla p + \frac{1}{4\pi}(\nabla \times \mathbf{B}) \times \mathbf{B} \qquad (4.3)$$

$$\partial_t \mathbf{B} = \nabla \times (\mathbf{V} \times \mathbf{B}) \qquad (4.4)$$

$$\nabla \cdot \mathbf{V} = 0 \;;\; \nabla \cdot \mathbf{B} = 0 \qquad (4.5)$$

reduce to two non-linear scalar equations (Kadomtsev and Pogutse, 1974; Strauss, 1976; Petviashvili and Pokhotelov, 1992): the conservation of the momentum along z

$$\partial_t \nabla_\perp^2 \psi + \{\psi, \nabla_\perp^2 \psi\} = \frac{1}{4\pi\rho}\{A_z, \nabla_\perp^2 A_z\} - \frac{B_0}{4\pi\rho}\partial_z \nabla_\perp^2 A_z, \qquad (4.6)$$

and the Maxwell-Faraday equation in the plane perpendicular to z

$$\partial_t A_z + B_0 \partial_z \psi + \{\psi, A_z\} = 0. \qquad (4.7)$$

Here the notation $\{.,.\}$ corresponds to the Poisson bracket (or the Jacobian)

$$\{a, b\} = \partial_x a \partial_y b - \partial_y a \partial_x b \equiv (\nabla a \times \nabla b) \cdot \mathbf{z}.$$

These equations can be written in dimensionless form, using new variables $t = \Omega_{ci} t$, $r_\perp = r_\perp/\rho_i$, $z = z/(c/\omega_{pi})$, $\rho = \rho/\rho_0$, $\Phi = \psi/(\rho_i^2 \Omega_{ci})$, $A = A_z V_A/(B_0 \rho_i^2 \Omega_{ci})$

$$d_t \nabla_\perp^2 \Phi = \{A, J\} - \partial_z J \qquad (4.8)$$

$$d_t A + \partial_z \Phi = 0 \qquad (4.9)$$

where $J = \nabla_\perp^2 A$ is the longitudinal current and

$$d_t \equiv \partial_t + \mathbf{V}_\perp \cdot \nabla_\perp.$$

The Alfvén vortices are solutions which are localized in a plane nearly perpendicular to z and propagate with a speed u in this plane while conserving their shape. Choosing the variables in the vortex plane x and η, with

$$\eta = y + \alpha z - ut, \quad \alpha = \tan(\vartheta), \qquad (4.10)$$

ϑ being the angle between the normal to the plane (x, η) and $\mathbf{B}_0$, we arrive to a two dimensional problem. In the new variables (x, η) the Eqs. (4.8) and (4.9) become

$$\{\Phi - ux, \nabla_\perp^2(\Phi - ux)\} = \{A - \alpha x, J\} \qquad (4.11)$$

$$\{\Phi - ux, A - \alpha x\} = 0 \qquad (4.12)$$

with the new Poisson bracket $\{a, b\} = \partial_x a \partial_\eta b - \partial_\eta a \partial_x b$. Equation (4.12) means that $(\Phi - ux)$ and $(A - \alpha x)$ depend on each other:

$$A - \alpha x = f(\Phi - ux) \qquad (4.13)$$

58
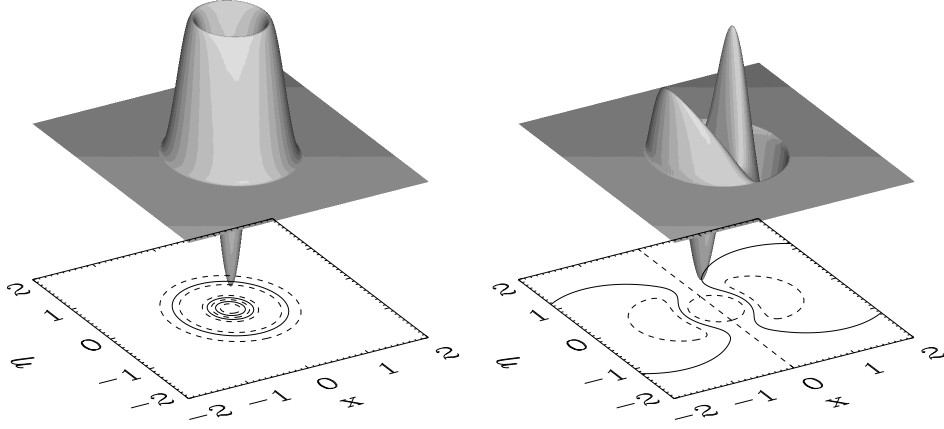
Figure 4.2: The surface of the current J above the vortex plane (x, η) and the contours of the potential A (that coincide here with the field lines) in this plane for (Left) the monopolar structure with the radius of localization $a=1$ and angle $\alpha=0$; (Right) the bipolar vortex with $a=1$, $\alpha=5°$, here the current and field lines are symmetric with respect to the line $x=0$ as far as the amplitude of the monopolar part of the vortex is chosen to be $A_0=0$. Figure from (Alexandrova, 2008).

so that Eq. (4.11) leads to an equation for $(\Phi - ux)$

$$\nabla_\perp^2 (\Phi - ux) = f'(\Phi - ux)J + f_1(\Phi - ux), \tag{4.14}$$

containing two arbitrary functions, f and f_1. There is, therefore, an infinite number of solutions of the system (4.11) and (4.12) in the form of travailing vortices.

Among this infinite set of solutions, the simplest Alfvén vortex solution is localized in a circle of the radius a (called below as *vortex radius*) in the plane (x, η), and decays at infinity as a power law. It satisfies a generalized Alfvén relation

$$\Phi = \xi A, \quad \text{with } \xi = \frac{u}{\alpha} \tag{4.15}$$

where α and u can be zero only simultaneously. Its current density J is a linear function of $A - \alpha x$ inside a circle of radius a and vanishes outside

$$\begin{cases} J = -k^2(A - \alpha x - c), & r < a \\ J = 0, & r \geq a \end{cases} \tag{4.16}$$

where k and c are constants. This solution is

$$\begin{cases} A = A_0(J_0(kr) - J_0(ka)) - \dfrac{2\alpha x}{kr} \dfrac{J_1(kr)}{J_0(ka)} + \alpha x, & r < a \\ A = a^2 \frac{\alpha x}{r^2}, & r \geq a. \end{cases} \tag{4.17}$$

Here A_0 is a constant amplitude, J_0 and J_1 are the Bessel functions of 0th and 1st order respectively, $r = \sqrt{x^2 + \eta^2}$ is the radial variable in the plane of the vortex.

The continuity of the solution (4.17) in $r=a$ requires that the parameter k and the radius a are coupled by the following dispersion relation

$$J_1(ka) = 0. \tag{4.18}$$

This relation ensures the continuity of the magnetic field $\mathbf{B}_\perp=(B_x, B_\eta)=(\partial_\eta A, -\partial_x A)$ in $r=a$ as well as a vanishing divergence of $\mathbf{B}_\perp$ everywhere.

Going back to the 3-D problem we must respect the following conditions: since $\partial_z \ll \nabla_\perp$ has to be satisfied, $\alpha = \tan(\vartheta) \sim \partial_z/\nabla_\perp \sim \varepsilon$ and thus the angle ϑ must be small. Similarly, the velocity u must also be small in order to satisfy the condition $\partial_t \ll \Omega_{ci}$, i.e. $u \sim \partial_t/\Omega_{ci} \sim \varepsilon$. In principle, ξ is arbitrary, but of the order of 1.

The Alfvén vortex solution (4.17) is the analogue of the incompressible unmagnetized hydrodynamic vortex solution, and, as in hydrodynamics, we distinguish here two types of vortices: monopole and dipole.

The monopolar vortex solution correspond to the case with $\alpha=0$ ($u=0$), i.e., when the projection of the mean field to the vortex plane is zero. This vortex is at rest in the plasma frame. It corresponds to a field-aligned force-free current localized within a circle of the radius a

$$\begin{cases} A = A_0(J_0(kr) - J_0(ka)), & r < a \\ A = 0, & r \geq a. \end{cases} \tag{4.19}$$

The current J and the field lines of the monopole are shown in Figure 4.2 (Left).

As soon as $\alpha \neq 0$ ($u \neq 0$) and the amplitude of monopolar part A_0 is zero, the solution (4.17) describes the dipolar vortex. It is not stationary in the plasma as the monopole, but propagates with a velocity u along the η-direction, the direction of the mean field projection on the vortex plane. The current of the dipolar vortex and its field lines are presented in Figure 4.2 (Right).

The situation when $u \neq 0$ and $A_0 \neq 0$ corresponds to a combined solution, with a monopole vortex traveling on the top of a dipole vortex. A, J, the magnetic field lines and velocity field lines are not symmetric with respect to the vortex center in this case.

The pure monopolar and pure dipolar vortices are topologically different and there is no continuous transition between them. These differences reflect themselves in the Fourier spectra of these two vortex types.

2   Spectral properties of Alfvén vortices

The Alfvén vortices are multi-scale nonlinear structures and one may wonder how they can influence the turbulent spectrum.

Suppose that a magnetic probe moves in space with a constant velocity, along the x-axis, with the coordinate $\eta = -0.2a$ (i.e., with the closest approach to the vortex axis of $0.2a$). Figure 4.3 (upper panels) shows the "measured" B_x profiles of monopole and dipole vortex structures for such a trajectory across the vortex. The lower panels of Figure 4.3 show the power spectral densities of these signals calculated via Fourier (solid
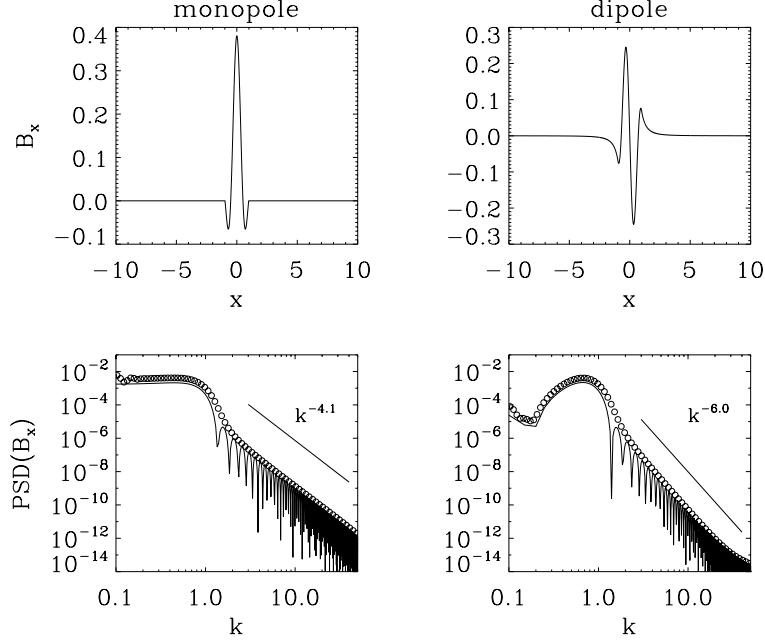
Figure 4.3: Upper panels: B_x component of the magnetic field of the monopole (left) and dipole (right) measured along x with $\eta=-0.2a$. Lower panels: the Fourier (solid line) and the Morlet (empty circles) transformations of the signals of the upper panels. The straight lines refer to the power law fits. Figure from (Alexandrova, 2008).

lines) and via Morlet Wavelet Transforms (circles). The power spectra of both, monopole and dipole, have a knee around the wave vector $k = 1/a$ (here, the radius of the vortex is $a=1$). Above this maximum, for $ka>2$, well-defined power laws are observed. The monopole vortex spectrum follows $\sim(ka)^{-4}$, while the dipolar follows $\sim(ka)^{-6}$. These power laws can be easily explained.

The magnetic field of a monopole vortex is completely localized within the circle of the radius a. It yields a discontinuity at $r=a$ for the current density, so that the PSD of J follows a k^{-2} power law. Therefore the power spectral density of the magnetic field components is k^{-4} (indeed, $J \sim k \cdot B$ and then $B^2 \sim J^2/k^2$). In the case of a dipolar vortex structure, the current is localized while the field extends to infinity, the derivative of the current has a discontinuity and its PSD follows a k^{-2} law, the PSD of the current is $\propto k^{-4}$ and that of the field follows a k^{-6} law.

Note that these spectra are not completely independent of the trajectory of the virtual probe through the vortices. Along some particular trajectories, the magnetic field components are equal to zero and then the spectrum vanishes. These trajectories are vortex separatrices, which can be easily seen in Figure 4 in (Alexandrova, 2008). For example, for the monopole structure, the trajectory along the x-axis with $\eta=0$ is a separatrix of the B_x component, and the one along η with $x=0$ is a separatrix of B_y. The dipole has twice as many separatrices: the trajectory along the x-axis with $\eta=0$ and the one along η with $x = 0$ are the separatrices of B_x, while $B_y=0$ along the diagonals.

61
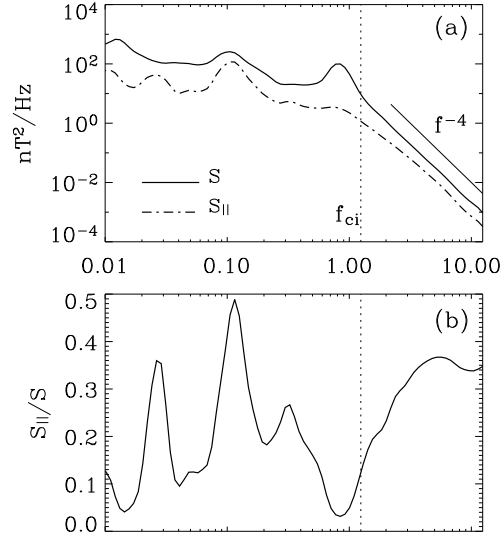
Figure 4.4: Spectral properties of magnetic fluctuations in the magnetosheath downstream of a quasi-perpendicular bow-shock during a time period [18:36–18:44] UT on March 31, 2001: (a) Solid line: the total power spectral density of magnetic fluctuations $\mathcal{S}$; dashed line: the spectrum of parallel fluctuations of magnetic field $\mathcal{S}_\parallel$. The straight line refers to a fit with a power law $\propto f^{-4}$. The vertical dotted line indicates the ion cyclotron frequency $f_{ci}=1.2$ Hz. (b) The level of compressible fluctuations $S_\parallel/S$ for different frequencies; even if strongly compressible fluctuations are present at 0.025 and 0.1 Hz, at the scales of the vortex (around 1 Hz), the compressibility is going down drastically, reflecting the incompressible nature of Alfvén vortices. Figure from (Alexandrova, 2008).

Actually, the probability that the satellite crosses the vortex along a separatrix is small and the spectra of Figure 4.3 can be considered as typical.

A spectral knee around the scale of the vortex radius is indeed observed in space plasmas, see Figure 2(a) in (Alexandrova et al., 2006) and Figure 4.4, for the Earth's magnetosheath examples; then, Figure III.12 in the PhD thesis of Lion (2016), for a fast solar wind example. In all these cases, a power-law spectrum close to f^{-4} is observed at higher frequencies (i.e., smaller scales). Spectra with a f^{-6} scaling have so far not been observed in the solar wind.

3 Apparent polarisation

When a spacecraft crosses a vortex structure, the polarisation, or coupling between different components of the magnetic field (and velocity field), depends on the trajectory. Let us consider observations within Saturn's magnetosheath, where Cassini/MAG have detected Alfvén vortex signatures, see Figure 4.5(a, upper panels). The corresponding polarisation $\delta B_y(\delta B_x)$ of the observed events is shown in the bottom panels of this figure. Figure 4.5(b) shows monopole (left) and dipole (right) crossed along the y-axis with different distances from the vortex centres (with different x coordinates); and in
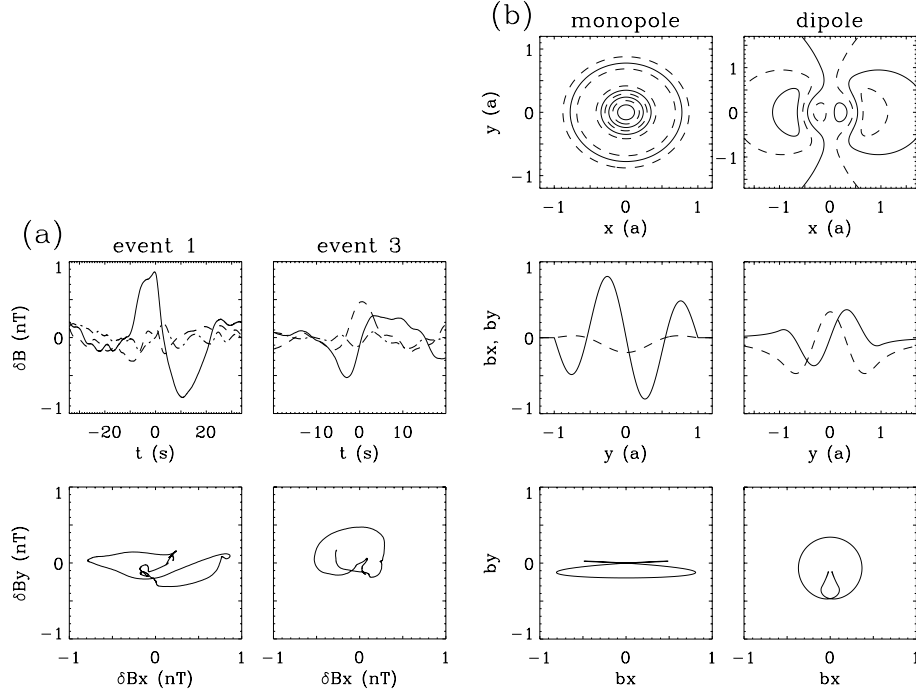
Figure 4.5: (a) Two examples of Alfvén vortices observed downstream of the Kronian bow-shock with Cassini/MAG instrument: magnetic field fluctuations (top) and corresponding polarisations (bottom panels); (b) monopole and dipole Alfven vortex cross-sections (Petviashvili and Pokhotelov, 1992) (top), magnetic field fluctuations along the satellite trajectory (along y-axis) with the closest approach to the vortex centrum $\Delta x = 0.04a$ in the case of the monopole, and with $\Delta x = 0.2a$ in the case of the dipole (middle panels); corresponding polarisations (bottom panels). Figure from (Alexandrova and Saur, 2008; Dudok de Wit et al., 2013).

the bottom panels, polarisations of the modelled field components $b_y(b_x)$[1] are shown in both cases. One can see that in the case of the monopole crossed close to its center, (with the closest approach $\Delta x \simeq 0.04a$), the polarisation is elliptical (nearly linear), and in the case of the dipole, crossed with $\Delta x = 0.2a$, the two transverse components have equal amplitudes and the polarisation is nearly circular. A visible difference with a quasi-linear circularly polarised Alfvén wave here is that smaller scales are present within a vortex and in the plane (bx, by), they give a kind of a *loop* around $b_x = 0$. The direction of polarisation (left or right handed) is also trajectory-dependent.

This trajectory dependence of the observed signal, and thus of the polarisation, explains why Alfvén vortices are difficult to detect from the polarisation maps, like Figure 3(d) in (Lion et al., 2016). But they are easily detected from the wavelet scalograms (or *LIM*'s) as energetic coherent events covering all scales[2].

The knowledge of possible observed polarisations by a spacecraft crossing an Alfvén vortex and also their spectral features may help to explain old puzzling observations of Tsurutani et al. (1994). The authors observed Alfvénic fluctuations with $\delta B/B_0 \simeq 0.3$ at ion scales, with a spectral knee around f_{ci} and with a very steep spectrum at higher frequencies. The polarisation in the plane perpendicular to the mean field was variable, from elliptical/quasi-linear to circular and both, left and right handed. The minimum variance indicated an oblique propagation, $\Theta_{kB} = 60°$, but also $5°$. These fluctuations were detected for all mean field orientations, with the Parker spiral orientation being the most likely, and not only for the radial $\mathbf{B_0}$, when small amplitude linear AIC waves are usually observed (see our discussion in Chapter 2, Section 6).

Indeed, the Parker spiral at 1 AU corresponds to $\Theta_{BV} \simeq 45°$, when $k_\perp$ fluctuations dominate the turbulent spectrum. As Alfvén vortices are $k_\perp$ structures, it is very possible that the described observations of ISEE-3 (Tsurutani et al., 1994) are indeed such vortices. Nearly linear polarisation and oblique Θ_{kB} can be explained by an Alfvén vortex crossed close to its centre, when the minimum and intermediate variance directions can be mixed up. Quasi-circular polarisation and small Θ_{kB} can be explained by a vortex crossed with a certain distance from the centre, and in this case the minimum variance is aligned with the vortex axis, i.e. along $\mathbf{B}_0$, like in the case study by Alexandrova et al. (2006).

4 Plasma behaviour within an Alfvén vortex

How does plasma behave within magnetic vortices? How do vortices interact with ions and electrons? Which role do they play in solar wind heating?

An attempt to estimate velocity fluctuations $\delta\mathbf{V}$ using the electric and magnetic field data was done in (Alexandrova et al., 2006). It was shown that indeed magnetic and velocity fluctuations are well aligned as expected for an Alfvén vortex.

---

[1] We distinguish here the notations for observed magnetic fluctuations $\delta\mathbf{B}$ and modelled ones $\mathbf{b}$.

[2] Alfvén vortices can also be detected in coherency maps, as we show in (Lion et al., 2016), see Figure 6 in this paper and the corresponding discussion.

Concerning kinetic physics, we have analysed electron distribution functions during the crossing of a vortex chain by Cluster in a fast solar wind stream in (Perrone et al., 2017). At times corresponding to the vortex central region, the electron distributions seem to be typical for the solar wind: almost isotropic with a spectral break between the core and the halo at about 60 eV. No evidence of accelerated particles or beams is observed. A different situation is found close to the vortex boundary, where the theoretical model predicts a discontinuity of the current. Here, the electron distributions are atypical, beams appear around 100 eV, in both antiparallel and perpendicular directions (parallel direction is not resolved in this case). These distributions could be unstable and generate Langmuir waves (Perrone et al., 2017). Unfortunately, due to the low time resolution of Cluster particles measurements, we were not able to follow the evolution of the electron pitch angle distribution all over the structure.

Recently, using MMS observations within an Alfvén vortex in the Earth's magnetosheath, we could study behaviour of the ions and the electrons within different parts of the vortex (Wang et al., 2019), see Figure 4.6.

We could verify the generalised Alfvén relation and show that

$$\delta \mathbf{B}_\perp / B_0 \simeq -0.9 \delta \mathbf{V}_\perp / V_A$$

within the vortex. Thus, the parallel current density $j_\parallel$ and the flow vorticity $\omega_\parallel$ are anti-aligned, see Figure 4.6(a). We observe T_i and T_e to be anti-correlated across the vortex: T_i varies as $j_\parallel$ and T_e correlates with $\omega_\parallel$. We note as well that, as was already observed with Cluster in the fast solar wind (Perrone et al., 2017), in the middle of the vortex and within two other $j_\parallel$ local maxima, the electron distribution function $f(\mathbf{v}_e)$ becomes isotropic (Figure 4.6(c)). Within the local minima of the current density, electrons have a $T_{e,\parallel} > T_{e,\perp}$ anisotropy. Ions behave in a different way: they are more isotropic at inflection points of $j_\parallel(r)$ and $\omega_\parallel(r)$ within the vortex (Figure 4.6(b)). Then, at the local extrema of $j_\parallel(r)$ the ions are anisotropic: $T_{i,\parallel} > T_{i,\perp}$ at the local maxima (where electrons are isotropic) and $T_{i,\parallel} < T_{i,\perp}$ at the local minima.

These MMS observations are not yet well understood and will be the subject of a future study. Recently developed fluid theory of coherent magnetic vortices in high-β space plasmas (Jovanovic et al., 2020) may probably explain the temperature behavior observed here.

5   Concluding remarks

Alfvén vortices are the simplest non-linear cylindrical solutions of the incompressible reduced MHD equations. A well known example of such a non-linear standing Alfvén wave in close cosmos is *the Alfvén wing* in the Jupiter magnetosphere (Drell et al., 1965; Neubauer, 1980; Saur et al., 2004) and (J. Saur, private communication, 2008).

In space plasma turbulence, such vortices seem to be quite generic: we observe them in the quasi-perpendicular magnetosheath of the Earth (Alexandrova et al., 2004, 2006; Alexandrova, 2008; Wang et al., 2019) and Saturn (Alexandrova and Saur, 2008), in the
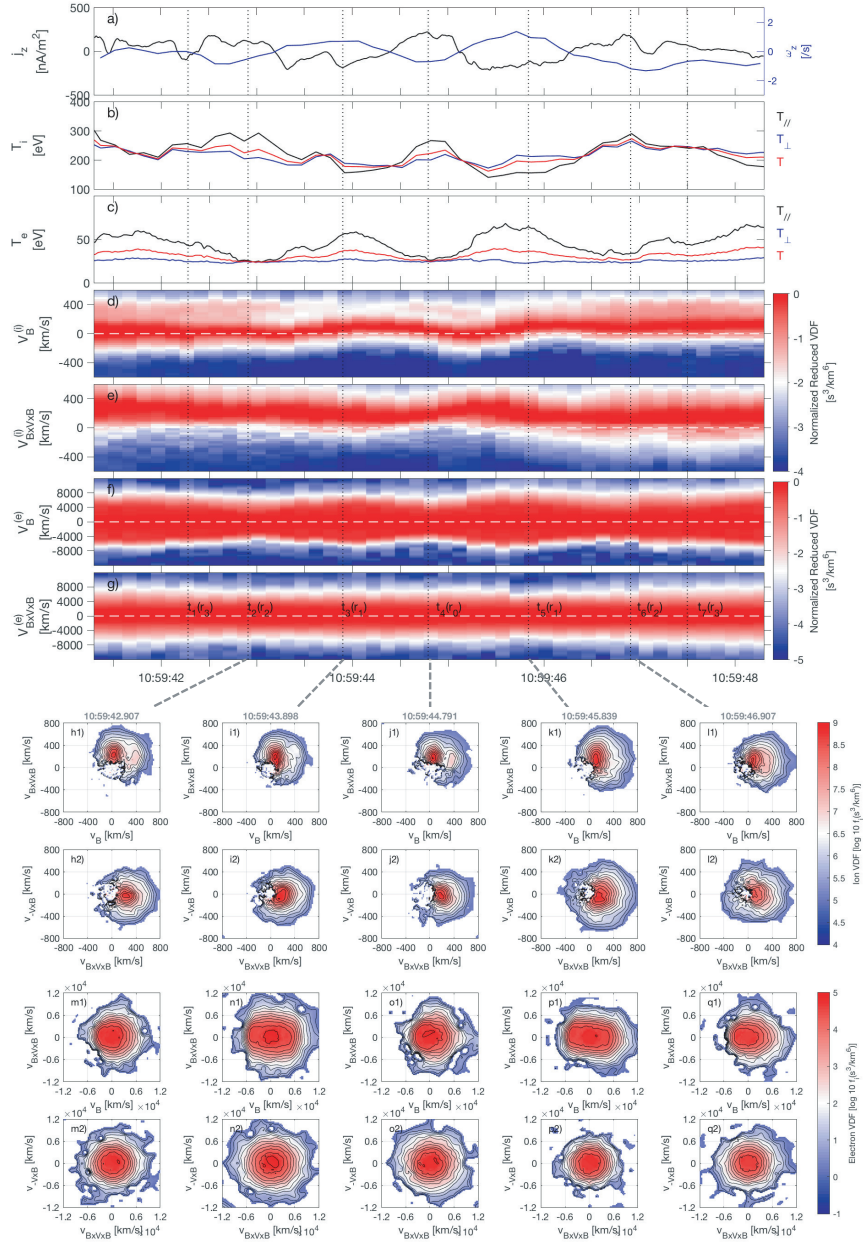
Figure 4.6: An Alfvén vortex crossed by MMS in Earth's magnetosheath on October 2nd, 2015, just before 11:00 UTC. (a) Parallel current density j_z and vorticity ω_z; (b) ion temperatures, total T_i (red), parallel $T_{i,\parallel}$ (black) and perpendicular $T_{i,\perp}$ (blue); (c) electron temperatures (with the same color code); (d) normalised reduced velocity distribution function (VDF) of the ions along and (e) perpendicular to the mean field; (f) and (g) the same as (d) and (e) but for electrons; (h)-(l) projections of the ion VDF's in the local $(\mathbf{B}, \mathbf{V})$–frame (e.g., Lion et al., 2016), in the middle of the vortex (r_0), and within the local minima and maxima of j_z (r_1 and r_2); (m)-(q) the same for electron VDF's. Figure from (Wang et al., 2019).

66

fast (Lion et al., 2016; Perrone et al., 2017) and the slow (Perrone et al., 2016; Roberts et al., 2016) solar wind.

Before the era of the multi-satellite measurements with Cluster and MMS, the magnetic perturbations $\delta\mathbf{B}$ due to Alfvén vortices, their spectral features and apparent polarisation have been probably interpreted as AIC or large amplitude Alfvén waves (e.g., Tsurutani et al., 1994).

The classical model of Petviashvili and Pokhotelov (1992) can explain our observations at $\ell \simeq [10, 20]\rho_i$ (Alexandrova et al., 2006; Alexandrova, 2008; Lion et al., 2016; Roberts et al., 2016; Perrone et al., 2017). At kinetic scales, this model is no more applicable. Approaching ion scales, vortices show the presence of a compressible component appearing when β_i increases (Perrone et al., 2016). We could explain this feature by pressure balance within the structure in the framework of fluid model of coherent vortices in high-β plasma (Jovanovic et al., 2020). At sub-ion scales there exist topologically similar cylindrical nearly field aligned vortex filaments, however, analytically it was possible to describe only a particular case when $\delta B_{\parallel}/B_0 = \delta n/n_0$ (Jovanovic et al., 2020). At electron scales, we could find vortex solutions in the presence of electron temperature anisotropy $T_{e\perp}/T_{e\parallel} > 1$ (Jovanović et al., 2015). These self-organized structures are non-linear cylindrical oblique whistler waves. They are characterized by both compressional and torsional perturbations of the magnetic field. These structures may probably explain our observations at the smallest resolved scales, of the order of a few ρ_e, described in Chapter 3, Section 3 (see Figure 3.9) and summarised in (Alexandrova et al., 2020).

Chapter 5

Conclusion and discussion

In this manuscript, we attempted to give our understanding of well developed turbulence in the solar wind. It is based on *in-situ* observations we could carry out with Cluster, Wind, Stereo, Helios, Ulysses, Cassini and MMS spacecrafts, under different plasma conditions and at radial distances $R \in [0.3, 9.5]$ AU.

Despite important differences with neutral fluids, space plasma turbulence seems to show a number of general properties inherent to hydrodynamic turbulence, such as a general turbulent spectrum and intermittency. Our principal contributions to the understanding of space plasma turbulence described in this document are:

- the observation of the kinetic range spectrum at sub-ion scales (Alexandrova et al., 2009, 2011, 2012; Alexandrova et al., 2020) and the evidence of its general shape between 0.3 and 1 AU in the form:

$$E(k_\perp) = A k_\perp^{-8/3} \exp(-k_\perp \ell_d); \tag{5.1}$$

- the observational evidence that the electron Larmor radius ρ_e plays the role of the *dissipation scale*, ℓ_d, for the electromagnetic turbulence in a collisionless plasma (Alexandrova et al., 2009, 2012; Alexandrova et al., 2020)

$$\ell_d = C\rho_e, \text{ with } C \in [1, 2]; \tag{5.2}$$

- the observational evidence that the turbulence amplitude A is correlated with the ion thermal and magnetic pressures, within the inertial range and at kinetic scales, in the solar wind (Alexandrova et al., 2011, 2013; Lacombe et al., 2014; Lion, 2016) and in the Saturn's magnetosphere (von Papen et al., 2014);

- the detection of coherent structures in the form of magnetic vortex filaments in a wide range of scales (from the inertial range to the dissipation range), in different plasma environments (fast and slow winds, planetary magnetosheaths) and at different distances from the Sun (at $R = 1$ and 9.5 AU), see (Alexandrova et al., 2006; Alexandrova, 2008; Alexandrova and Saur, 2008; Lion et al., 2016; Lion, 2016; Roberts et al., 2016; Perrone et al., 2016, 2017; Wang et al., 2019; Alexandrova et al., 2020).

What is the theoretical interpretation of these results? How consistent are they with previous and recent observations?

1 Interpretation of kinetic spectrum: small scale cascade and dissipation range?

The end of the inertial range and ion scales were usually attributed to the dissipation range of solar wind turbulence. However, the power-law behavior observed at ion scales (e.g., Leamon et al., 1998a) instilled uncertainty in my mind when I started reading solar wind literature during my short post-doctoral period in Calabria University (in 2006): What if it was not the end of the story, or rather, of the cascade?

Thanks to Cluster/STAFF instrument, that is the most sensitive search-coil magnetometer by today, we were able to measure the small scale cascade following a general shape $k_\perp^{-2.8}$ (if the fitting frequency range is well separated from the ion and electron scales) and an exponential roll-off at electron scales. Three different observational approaches point out that this roll-off is controlled by ρ_e. One analytic function which describes both parts is given by Equation (5.1). Precisely, it describes the solar wind spectrum of magnetic fluctuations at scales smaller than the ion characteristic scales, λ_i and ρ_i, and going beyond the electron scales. This model describes well the totality of observed spectra without signatures of quasi-parallel whistlers. The amplitude of the spectrum A seems to be a function of the ion thermal pressure $A \sim nkT_p$ and magnetic pressure $A \sim B_0^2$. Such dependences are also observed in the magnetosphere of Saturn (von Papen et al., 2014), indicating the generality of the phenomenon.

The power-law range at sub-ion scales is usually attributed to a mixture of dispersive modes, such as the magnetosonic/whistler mode or the kinetic Alfvén mode (Stawicki et al., 2001; Galtier and Bhattacharjee, 2003; Cho and Lazarian, 2004; Howes et al., 2008a; Schekochihin et al., 2009; Rudakov et al., 2011; Boldyrev and Perez, 2012; Cerri et al., 2016), interacting non-linearly in Fourier space.

The observed power-law $k_\perp^{-2.8}$ is quite steep with respect to the incompressible Hall MHD, Electron MHD or gyro-kinetic predictions, $k^{-7/3}$ (Biskamp et al., 1999; Howes et al., 2008b; Schekochihin et al., 2009), or wave turbulence prediction $k_\perp^{-5/2} k_\parallel^{-1/2}$ (Galtier and Bhattacharjee, 2003; Galtier, 2006, 2009).

A scaling of $k_\perp^{-8/3}$, closer to observations, was found in 3D incompressible EMHD numerical simulations in presence of a strong external magnetic field $\mathbf{B_0}$ (Meyrand and Galtier, 2013). The authors observe that under such conditions, turbulence is characterized by filaments of electric currents parallel to $\mathbf{B_0}$ and the transfer of energy in the parallel direction is negligible. This turbulent regime is in agreement with our observations of Alfvén vortices at kinetic scales.

The same scaling of $k_\perp^{-8/3}$ was observed in a numerical study of strong KAW turbulence (Boldyrev and Perez, 2012). It was explained by the dominance of pressure-balanced 2D-structures. This is in agreement with magnetic vortices in high β plasma (Jovanovic et al., 2020).

Indeed, compressible effects are important at kinetic scales (Alexandrova et al., 2008a; Salem et al., 2012; Kiyani et al., 2013; Perrone et al., 2016). In Lacombe et al. (2017), we have shown that the magnetic compressibility, defined as,

$$C_\parallel = \delta B_\parallel^2 / (\delta B_\perp^2 + \delta B_\parallel^2), \tag{5.3}$$

at kinetic scales varies with the plasma β in a way compatible with the predictions of Boldyrev et al. (2013) for low frequency magnetic structures in pressure balance, e.g., KAWs in the linear regime (Matteini et al., 2020).

2D and 3D Hybrid numerical simulations of Franci et al. (2015, 2016) recover magnetic spectra $\sim k_\perp^{-\alpha}$, with $\alpha \in [2.8, 3.5]$, which is close to what is observed in the solar wind. Moreover, the same numerical model describes well the observed $C_\parallel$ behavior, as we have recently shown in (Matteini et al., 2020). Franci et al. (2017) provides numerical evidence of magnetic reconnection of current sheets at ion scales being at the origin of the small-scale cascade. This result may provide an explanation of observations of magnetic filaments at sub-ion scales.

A theoretical model describing vortex generation by tearing instability for low β at the scales of the ion spectral break was proposed by Mallet et al. (2017). However, it is not clear if the time needed to switch on the instability (inverse of the growth rate $\tau_{\text{tearing}} = \gamma_{\text{tearing}}^{-1}$) is short enough to dominate the non-linear transfer ($\tau_{\text{tearing}} < \tau_{NL}$ at the scale of a current sheet thickness). This point can be probably checked by numerical simulations.

Loureiro and Boldyrev (2017) propose a similar idea, but to describe the whole kinetic range of turbulence. The authors assume $\tau_{\text{tearing}} < \tau_{NL}$ and then obtain the energy spectrum of Alfvénic turbulence mediated by kinetic reconnection to follow a power-law $\sim k_\perp^{-\alpha}$, with $\alpha \in [8/3, 3]$.

What about an exponential roll-off at electron scales? In usual fluid turbulence, the far dissipation range is described by $E(k) \sim k^3 \exp(-ck\ell_d)$ (with $c \simeq 7$) (Chen et al., 1993). This is due to the resistive damping rate $\propto k^2$ valid in a collisional fluid, which gives an exponential spectral tail. In the collisionless plasma of the solar wind there is no resistive damping, and thus this coincidence deserves an explanation.

Gyrokinetic simulations of Howes et al. (2008a) typically show an exponential roll-off of the magnetic power spectra at electron scales. This behavior seems to be related to the electron Landau damping. However, local interactions result in a strong Landau damping and in a sharp cut-off at electron scales.

Howes et al. (2011) consider a *weakened cascade model* which includes nonlinear and non-local transfer of energy from large to small scales in Fourier space (see Equation (23) in (Howes et al., 2011)) and the damping of kinetic Alfvén waves. The spectral laws are respectively $E_k \propto k_\perp^{-5/3}$ at large scales and $E_k \propto k_\perp^{-7/3}$ between ion and electron scales. When taking into account the damping term, Howes et al. (2011) obtain numerically the same spectral laws, with a final curved tail at scales smaller than electron scales. Superficially, this spectrum thus resembles the analytic form which we have found to be valid to describe the solar wind turbulence.

Note that the damping term in the model of Howes et al. (2011) is obtained by linearising the Vlasov-Maxwell equations in the gyrokinetic limit ($k_\parallel \ll k_\perp$, with frequencies $f \ll f_{ci}$). For $k_\perp \rho_i \gg 1$ it has the form $\gamma \simeq k_\parallel V_A (k_\perp \rho_i)^2 \propto k_\parallel k_\perp^2$ (see Equation (63) in (Howes et al., 2006)). Taking into account the assumption of critical balance $\tau_{NL} = \tau_A$ (i.e., $k_\perp u = k_\parallel V_A$) and the spectral index $-7/3$ (that means that velocity fluctuation u verifies $u \sim k_\perp^{-2/3}$), one gets $k_\parallel \propto k_\perp^{1/3}$. Therefore, the damping term takes the form $\gamma \propto k_\perp^{2+1/3}$. The exponent of the damping rate is thus very close to the k^2 scaling of the Laplacian viscous term, which is known to lead in hydrodynamical turbulence to an exponential tail in the dissipation range.

The model of Howes et al. (2011) is based on the assumption $k_\perp \gg k_\parallel$. So, while the proposed phenomenology may explain the exponential tail of the $k_\perp$–spectrum, it cannot describe more isotropic wave vectors. Indeed, in Lacombe et al. (2017), we have shown that while between ion and electron scales quasi-2D turbulence (with $k_\perp \gg k_\parallel$) dominates, at electron scales, the wave vectors are more isotropic (as well as the amplitudes of $\delta \mathbf{B}$).

Passot and Sulem (2015) proposed the phenomenological model of KAW turbulence, which covers weak and strong regimes. The authors show that the weak turbulence regime of KAW cannot survive in the presence of a significant Landau damping. In the strong turbulence regime, the process of ion temperature homogenization along magnetic field lines, induced by Landau damping, introduces an additional characteristic time which modifies the turbulence transfer time at sub-ion scales, leading to a power law magnetic spectrum steeper than the classical $-7/3$ spectrum of critically balanced KAW turbulence. At electron scales, this model shows spectra following an exponential cut-off due to the electron Landau damping.

Schreiner and Saur (2017) developed an analytic dissipation model to describe turbulence at electron scales. This model combines the energy transport from large to small scales and collisionless damping, which removes energy from the magnetic fluctuations in the kinetic regime. The authors assume wave-particle interactions of KAWs to be the main damping process. Turbulence is strong and critically balanced, i.e., for a given $k_\perp$, $k_\parallel \propto k_\perp^{1/3}$. Based on the KAWs dissipation rate particularity, the authors explain why $\ell_d \simeq \rho_e$, independently of the solar wind conditions. This model described nicely the observed spectrum, Equation (5.1).

Parashar et al. (2018) did a 2D full particle simulations to study the role of electron plasma beta, β_e. The obtained magnetic power spectra show an exponential-like shape on electron scales with a weak dependence on β_e: the PSDs decrease faster for larger β_e (and for larger ρ_e) (cf., Parashar et al., 2018, Figure 6, top panel) in a qualitative agreement with the observational results presented here.

2 Intermittency: current sheets or vortices?

Most of the studies of intermittent events in the solar wind reveal the presence of planar structures such as current sheets, shocks and rotational discontinuities (Veltri and Man-

geney, 1999; Salem, 2000; Mangeney et al., 2001; Greco et al., 2009, 2010; Perri et al., 2012b). Here we show the importance of magnetic vortices (Alexandrova et al., 2006; Alexandrova and Saur, 2008; Lion et al., 2016; Roberts et al., 2016; Perrone et al., 2016, 2017), rarely observed before (Rezeau et al., 1993; Verkhoglyadova et al., 2003). Why such structures did not attract more attention in the past?

The most important point is *mono-satellite vs multi-satellite observations*. Indeed, a wave-packet passing across a satellite along $\mathbf{B_0}$ will give the same signal of $\delta\mathbf{B}(t)$ as a magnetic flux rope convected by the wind in a plane perpendicular to $\mathbf{B_0}$. Only multi-satellite observations can discriminate these two phenomena, see Figure 5 in (Alexandrova et al., 2006) and the corresponding discussion. Thus, only with the era of Cluster (and later with MMS), we could establish the presence of such cylindrical structures in the turbulent signal in the solar wind and the Earth's magnetosheath. Previously, the signatures of vortices could be interpreted as large-amplitude Alfvén (or AIC) waves, see the discussion in Chapter 4, Section 3.

Another crucial point is the *detection method*. Current sheets are easily detected using the Partial Variance of Increments (PVI) method (Greco et al., 2018), based on magnetic field increments $\Delta B_{j,\tau} = B_j(t+\tau) - B_j$, where $j = x, y, z$. Haar wavelets are indeed very similar to PVI and give alike results (Veltri and Mangeney, 1999; Salem, 2000; Mangeney et al., 2001). In our studies we usually use Morlet wavelets (Alexandrova et al., 2006; Alexandrova and Saur, 2008), whose mother function looks like the vortex solution (in the form of a Bessel $J_{0,1}$ function of the zeroth and first order) close to a vortex centre. Thus, it helps to detect vortices. But to avoid an influence of the method on our results, we also used direct magnetic field measurements at a given frequency range (Perrone et al., 2016, 2017). And again, we have found magnetic vortices. These last studies show just few current sheets. While, the signal depends on the trajectory of a satellite across the vortex, it can be quite similar to a current sheet if the trajectory goes through the centrum.

It is interesting to understand how the dominance of Alfvén vortices as intermittent structures agrees with modern theories of space plasma turbulence.

As we have discussed in Chapter 1, a very popular model of solar wind turbulence is Critically Balanced Alfvénic turbulence of Goldreich and Sridhar (1995) at MHD scales. At kinetic scales, it is Critically Balanced Kinetic Alfvén turbulence (e.g., Schekochihin et al., 2009). As we have already discussed, the basis of these models is the balance between linear Alfvén time τ_A at MHD scales (τ_{KAW} at kinetic scales) and non-linear time τ_{NL}. Vortices are cylindrical structures which can be (i) field aligned magnetostatic or (ii) slightly inclined tubes having a small angle with $\mathbf{B_0}$, such vortices propagate slowly in the plane nearly perpendicular to the mean field. If these structures dominate turbulence within 1–2 decades of the inertial range and at sub-ion scales, there is a problem with the Critical Balance approach. In fact, the parallel time of a field-aligned vortex is zero all along the field line ($\tau_{\parallel,\text{vortex}} = 0$), and it is small for an inclined vortex. A perpendicular time (or life time) can be quite long if the vortex is stable in the plasma ($\tau_{\perp,\text{vortex}} \gg \tau_{NL}$ at the smallest scale of the vortex). So, parallel and perpendicular characteristic times are not of the same order at all. The estimation of the vortex life-

time, however, is an open question and should be studied in more details via numerical simulations and multi-satellite observations. In particular, it will be interesting to find occurrence of the same plasma parcel measured by Parker Solar Probe and by Solar Orbiter at different R during the satellites radial alignments.

A larger statistical study should be done to determine also typical filling factors of different structures (planar and cylindrical) and their possible coupling across scales. How do they interact with ions and electrons, and thus participate to the solar wind global heating? And what is going on closer to the Sun, where we have an onset of turbulence?

In hydrodynamic turbulence, the topology of intermittent events reflects the original structures of the laminar-turbulent transition, i.e, the onset of turbulence. The first results of Parker Solar Probe at 0.17 AU (Bale et al., 2019) show $\delta B/B_0 \sim 1$ reversals at very large scales. They are observed during the time intervals for a non-radial-field wind, when fluctuations with $\mathbf{k}\perp\mathbf{B_0}$ are measured. Probably here, we are facing the origin of turbulence in the solar wind... How are they generated? Which role do they play in the shaping of the particles distributions?

During these reversals at smaller scales, Bale et al. (2019) observe signatures of coherent structures covering inertial and kinetic ranges, see Figure 3 in (Bale et al., 2019). The topology of these structures closer to the Sun is not known by today and will be the topic of some of our future studies.

Bibliography

Alexandrova, O. (2008). Solar wind vs magnetosheath turbulence and Alfvén vortices. *Nonlinear Processes in Geophysics*, 15:95–108.

Alexandrova, O., Carbone, V., Veltri, P., and Sorriso-Valvo, L. (2007). Solar wind Cluster observations: Turbulent spectrum and role of Hall effect. *Planet. Space Sci.*, 55:2224–2227.

Alexandrova, O., Carbone, V., Veltri, P., and Sorriso-Valvo, L. (2008a). Small-Scale Energy Cascade of the Solar Wind Turbulence. *ApJ*, 674:1153–1157.

Alexandrova, O., Chen, C. H. K., Sorriso-Valvo, L., Horbury, T. S., and Bale, S. D. (2013). Solar Wind Turbulence and the Role of Ion Instabilities. *Space Sci. Rev.*, 178:101–139.

Alexandrova, O., Jagarlamudi, V. K., Rossi, C., Maksimovic, M., Hellinger, P., Shprits, Y., and Mangeney, A. (2020). Kinetic turbulence in space plasmas observed in the near-earth and near-sun solar wind. *arXiv2004.01102*.

Alexandrova, O., Lacombe, C., and Mangeney, A. (2008b). Spectra and anisotropy of magnetic fluctuations in the Earth's magnetosheath: Cluster observations. *An.Geo.*, 26:3585–3596.

Alexandrova, O., Lacombe, C., Mangeney, A., and Grappin, R. (2011). Fluid-like dissipation of magnetic turbulence at electron scales in the solar wind. *arXiv:1111.5649v1*.

Alexandrova, O., Lacombe, C., Mangeney, A., Grappin, R., and Maksimovic, M. (2012). Solar Wind Turbulent Spectrum at Plasma Kinetic Scales. *ApJ*, 760:121.

Alexandrova, O., Mangeney, A., Maksimovic, M., Cornilleau-Wehrlin, N., Bosqued, J.-M., and André, M. (2006). Alfvén vortex filaments observed in magnetosheath downstream of a quasi-perpendicular bow shock. *J. Geophys. Res.*, 111(A10):12208.

Alexandrova, O., Mangeney, A., Maksimovic, M., Lacombe, C., Cornilleau-Wehrlin, N., Lucek, E. A., Décréau, P. M. E., Bosqued, J.-M., Travnicek, P., and Fazakerley, A. N. (2004). Cluster observations of finite amplitude Alfvén waves and small-scale magnetic filaments downstream of a quasi-perpendicular shock. *J. Geophys. Res.*, 109:5207–+.

Alexandrova, O. and Saur, J. (2008). Alfvén vortices in Saturn's magnetosheath: Cassini observations. *Geophys. Res. Lett.*, 35:15102.

Alexandrova, O., Saur, J., Lacombe, C., Mangeney, A., Mitchell, J., Schwartz, S. J., and Robert, P. (2009). Universality of Solar-Wind Turbulent Spectrum from MHD to Electron Scales. *Phys. Rev. Lett.*, 103(16):165003–+.

Artemyev, A. V., Angelopoulos, V., Halekas, J. S., Vinogradov, A. A., Vasko, I. Y., and Zelenyi, L. M. (2018). Dynamics of Intense Currents in the Solar Wind. *ApJ*, 859(2):95.

Artemyev, A. V., Angelopoulos, V., and Vasko, I. Y. (2019). Kinetic Properties of Solar Wind Discontinuities at 1 AU Observed by ARTEMIS. *Journal of Geophysical Research (Space Physics)*, 124(6):3858–3870.

Bale, S. D., Badman, S. T., Bonnell, J. W., and et al. (2019). Highly structured slow solar wind emerging from an equatorial coronal hole. *Nature*, 576:237–242.

Bale, S. D., Kasper, J. C., Howes, G. G., Quataert, E., Salem, C., and Sundkvist, D. (2009). Magnetic Fluctuation Power Near Proton Temperature Anisotropy Instability Thresholds in the Solar Wind. *Phys. Rev. Lett.*, 103:211101–+.

Bale, S. D., Kellogg, P. J., Mozer, F. S., Horbury, T. S., and Reme, H. (2005). Measurement of the Electric Fluctuation Spectrum of Magnetohydrodynamic Turbulence. *Phys. Rev. Lett.*, 94(21):215002–+.

Banerjee, S. and Galtier, S. (2014). A kolmogorov-like exact relation for compressible polytropic turbulence. *Journal of Fluid Mechanics*, 742:230–242.

Banerjee, S., Hadid, L. Z., Sahraoui, F., and Galtier, S. (2016). Scaling of Compressible Magnetohydrodynamic Turbulence in the Fast Solar Wind. *ApJ*, 829(2):L27.

Bavassano, B., Dobrowolny, M., Mariani, F., and Ness, N. F. (1982). Radial evolution of power spectra of interplantary Alfvénic turbulence. *J. Geophys. Res.*, 87(A5):3617–3622.

Beinroth, H. J. and Neubauer, F. M. (1981). Properties of whistler mode waves between 0.3 and 1.0 AU from HELIOS observations. *J. Geophys. Res.*, 86:7755–7760.

Belcher, J. W. and Davis, L. (1971). Large-amplitude Alfvén waves in the interplanetary medium, 2. *J. Geophys. Res.*, 76:3534–3563.

Berčič, L., Maksimović, , M., Land i, S., and Matteini, L. (2019). Scattering of strahl electrons in the solar wind between 0.3 and 1 au: Helios observations. *MNRAS*, 486(3):3404–3414.

Biskamp, D., Schwarz, E., and Drake, J. F. (1996). Two-Dimensional Electron Magnetohydrodynamic Turbulence. *Phys. Rev. Lett.*, 76:1264–1267.

Biskamp, D., Schwarz, E., Zeiler, A., Celani, A., and Drake, J. F. (1999). Electron magnetohydrodynamic turbulence. *Physics of plasmas*, 6:751–758.

Boldyrev, S. (2006). Spectrum of Magnetohydrodynamic Turbulence. *Phys. Rev. Lett.*, 96(11):115002–+.

Boldyrev, S., Horaites, K., Xia, Q., and Perez, J. C. (2013). Toward a Theory of Astrophysical Plasma Turbulence at Subproton Scales. *ApJ*, 777(1):41.

Boldyrev, S. and Perez, J. C. (2012). Spectrum of Kinetic-Alfvén Turbulence. *ApJ*, 758:L44.

Borovsky, J. E. (2008). Flux tube texture of the solar wind: Strands of the magnetic carpet at 1 AU? *J. Geophys. Res.*, 113(A12):8110–+.

Bourouaine, S., Alexandrova, O., Marsch, E., and Maksimovic, M. (2012). On Spectral Breaks in the Power Spectra of Magnetic Fluctuations in Fast Solar Wind between 0.3 and 0.9 AU. *ApJ*, 749:102.

Bowen, T. A., Mallet, A., Huang, J., Klein, K. G., Malaspina, D. M., Stevens, M., Bale, S. D., Bonnell, J. W., Case, A. W., Chandran, B. D. G., Chaston, C. C., Chen, C. H. K., Dudok de Wit, T., Goetz, K., Harvey, P. R., Howes, G. G., Kasper, J. C., Korreck, K. E., Larson, D., Livi, R., MacDowall, R. J., McManus, M. D., Pulupa, M., Verniero, J. L., and Whittlesey, P. (2020). Ion-scale Electromagnetic Waves in the Inner Heliosphere. *ApJS*, 246(2):66.

Bruno, R. and Carbone, V. (2013). The Solar Wind as a Turbulence Laboratory. *Living Reviews in Solar Physics*, 10:2.

Bruno, R. and Trenchi, L. (2014). Radial Dependence of the Frequency Break between Fluid and Kinetic Scales in the Solar Wind Fluctuations. *ApJ*, 787:L24.

Bruno, R., Trenchi, L., and Telloni, D. (2014). Spectral Slope Variation at Proton Scales from Fast to Slow Solar Wind. *ApJ*, 793:L15.

Burlaga, L. F. (1969). Directional Discontinuities in the Interplanetary Magnetic Field. *Sol. Phys.*, 7(1):54–71.

Burlaga, L. F. (1971). Nature and origin of directional discontinuities in the solar wind. *J. Geophys. Res.*, 76(19):4360.

Burlaga, L. F., Lemaire, J. F., and Turner, J. M. (1977). Interplanetary current sheets at 1 AU. *J. Geophys. Res.*, 82(22):3191.

Burlaga, L. F. and Ness, N. F. (1969). Tangential Discontinuities in the Solar Wind. *Sol. Phys.*, 9(2):467–477.

Carbone, V., Marino, R., Sorriso-Valvo, L., Noullez, A., and Bruno, R. (2009). Scaling Laws of Turbulence and Heating of Fast Solar Wind: The Role of Density Fluctuations. *Phys. Rev. Lett.*, 103(6):061102–+.

Cardesa, J. I., Vela-Martín, A., and Jiménez, J. (2017). The turbulent cascade in five dimensions. *Science*, 357(6353):782–784.

Celnikier, L. M., Harvey, C. C., Jegou, R., Moricet, P., and Kemp, M. (1983). A determination of the electron density fluctuation spectrum in the solar wind, using the ISEE propagation experiment. *A&A*, 126:293–298.

Cerri, S. S., Califano, F., Jenko, F., Told, D., and Rincon, F. (2016). Subproton-scale Cascades in Solar Wind Turbulence: Driven Hybrid-kinetic Simulations. *ApJ*, 822(1):L12.

Chaplygin, S. A. (1903). One case of vortex motion in fluid. *[reprinted in: Collected Works, **2**, 155 (1948) (in Russian)],*
One case of vortex motion in fluid, *Trans. Phys. Sect. Imperial Moscow Soc. Friends Nat. Sci.*, 11:11–14.

Chen, C. H. K. (2016). Recent progress in astrophysical plasma turbulence from solar wind observations. *Journal of Plasma Physics*, 82(6):535820602.

Chen, C. H. K. and Boldyrev, S. (2017). Nature of kinetic scale turbulence in the earths magnetosheath. *The Astrophysical Journal*, 842(2):122.

Chen, C. H. K., Boldyrev, S., Xia, Q., and Perez, J. C. (2013). Nature of Subproton Scale Turbulence in the Solar Wind. *Phys. Rev. Lett.*, 110(22):225002.

Chen, C. H. K., Horbury, T. S., Schekochihin, A. A., Wicks, R. T., Alexandrova, O., and Mitchell, J. (2010). Anisotropy of Solar Wind Turbulence between Ion and Electron Scales. *Phys. Rev. Lett.*, 104:255002–+.

Chen, C. H. K., Howes, G. G., Bonnell, J. W., Mozer, F. S., Klein, K. G., and Bale, S. D. (2012a). Kinetic scale density fluctuations in the solar wind. *Solar Wind 13 Proceedings (in press), arXiv:1210.0127*.

Chen, C. H. K., Leung, L., Boldyrev, S., Maruca, B. A., and Bale, S. D. (2014). Ion-scale spectral break of solar wind turbulence at high and low beta. *Geophys. Res. Lett.*, 41:8081–8088.

Chen, C. H. K., Salem, C. S., Bonnell, J. W., Mozer, F. S., and Bale, S. D. (2012b). Density Fluctuation Spectrum of Solar Wind Turbulence between Ion and Electron Scales. *Phys. Rev. Lett.*, 109(3):035001.

Chen, S., Doolen, G., Herring, J. R., Kraichnan, R. H., Orszag, S. A., and She, Z. S. (1993). Far-dissipation range of turbulence. *Physical Review Letters*, 70:3051–3054.

Cho, J. and Lazarian, A. (2004). The Anisotropy of Electron Magnetohydrodynamic Turbulence. *ApJ*, 615:L41–L44.

Cornilleau-Wehrlin, N., Chauveau, P., Louis, S., Meyer, A., Nappa, J. M., Perraut, S., Rezeau, L., Robert, P., Roux, A., de Villedary, C., de Conchy, Y., Friel, L., Harvey, C. C., Hubert, D., Lacombe, C., Manning, R., Wouters, F., Lefeuvre, F., Parrot, M., Pincon, J. L., Poirier, B., Kofman, W., and Louarn, P. (1997). The Cluster Spatio-Temporal Analysis of Field Fluctuations (STAFF) Experiment. *Space Sci. Rev.*, 79:107–136.

Danaila, L., Anselmet, F., Zhou, T., and Antonia, R. A. (2001). Turbulent energy scale budget equations in a fully developed channel flow. *Journal of Fluid Mechanics*, 430:87–109.

Davidson, P. A. (2004). *Turbulence: An Introduction for Scientists and Engineers.* Oxford University Press.

Démoulin, P. (2009). Why Do Temperature and Velocity Have Different Relationships in the Solar Wind and in Interplanetary Coronal Mass Ejections? *Sol. Phys.*, 257(1):169–184.

Denskat, K. U., Beinroth, H. J., and Neubauer, F. M. (1983). Interplanetary magnetic field power spectra with frequencies from 2.4 X 10 to the -5th HZ to 470 HZ from HELIOS-observations during solar minimum conditions. *J. Geophys.*, 54:60–67.

Drell, S. D., Foley, H. M., and Ruderman, M. A. (1965). Drag and Propulsion of Large Satellites in the Ionosphere; An Alfvén Propulsion Engine in Space. *Phys. Rev. Lett.*, 14(6):171–175.

Dudok de Wit, T., Alexandrova, O., Furno, I., Sorriso-Valvo, L., and Zimbardo, G. (2013). Methods for Characterising Microphysical Processes in Plasmas. *Space Sci. Rev.*.

Escoubet, C. P., Schmidt, R., and Goldstein, M. L. (1997). Cluster - Science and Mission Overview. *Space Sci. Rev.*, 79:11–32.

Farge, M. (1992). Wavelet transforms and their applications to turbulence. *Annual Review of Fluid Mechanics*, 24:395–457.

Farge, M. and Schneider, K. (2015). Wavelet transforms and their applications to MHD and plasma turbulence: a review. *ArXiv e-prints*.

Fiedler, H. E. (1988). Coherent structures in turbulent flows. *Progress in Aerospace Sciences*, 25:231–269.

Franci, L., Cerri, S. S., Califano, F., Landi, S., Papini, E., Verdini, A., Matteini, L., Jenko, F., and Hellinger, P. (2017). Magnetic Reconnection as a Driver for a Sub-ion-scale Cascade in Plasma Turbulence. *ApJ*, 850(1):L16.

Franci, L., Landi, S., Matteini, L., Verdini, A., and Hellinger, P. (2016). Plasma Beta Dependence of the Ion-scale Spectral Break of Solar Wind Turbulence: High-resolution 2D Hybrid Simulations. *ApJ*, 833:91.

Franci, L., Verdini, A., Matteini, L., Landi, S., and Hellinger, P. (2015). Solar Wind Turbulence from MHD to Sub-ion Scales: High-resolution Hybrid Simulations. *ApJ*, 804:L39.

Frisch, U. (1995). *Turbulence*. Cambridge University Press.

Galtier, S. (2006). Wave turbulence in incompressible Hall magnetohydrodynamics. *Journal of Plasma Physics*, 72:721–769.

Galtier, S. (2009). Wave turbulence in magnetized plasmas. *Nonlinear Processes in Geophysics*, 16:83–98.

Galtier, S. and Bhattacharjee, A. (2003). Anisotropic weak whistler wave turbulence in electron magnetohydrodynamics. *Physics of plasmas*, 10:3065–3076.

Galtier, S. and Buchlin, E. (2007). Multiscale Hall-Magnetohydrodynamic Turbulence in the Solar Wind. *ApJ*, 656:560–566.

Gary, S. P., Convery, P. D., Denton, R. E., Fuselier, S. A., and Anderson, B. J. (1994). Proton and helium cyclotron anisotropy instability thresholds in the magnetosheath. *J. Geophys. Res.*, 99(A4):5915–5934.

Gary, S. P. and Feldman, W. C. (1977). Solar wind heat flux regulation by the whistler instability. *J. Geophys. Res.*, 82:1087–1094.

Ghosh, S., Siregar, E., Roberts, D. A., and Goldstein, M. L. (1996). Simulation of high-frequency solar wind power spectra using Hall magnetohydrodynamics. *J. Geophys. Res.*, 101:2493–2504.

Goldreich, P. and Sridhar, S. (1995). Toward a theory of interstellar turbulence. II. Strong Alfvénic turbulence. *ApJ*, 438:763–775.

Gosling, J. T. (2012). Magnetic Reconnection in the Solar Wind. *Space Sci. Rev.*, 172(1-4):187–200.

Gosling, J. T., McComas, D. J., Roberts, D. A., and Skoug, R. M. (2009). A One-Sided Aspect of Alfvenic Fluctuations in the Solar Wind. *ApJ*, 695(2):L213–L216.

Grafke, T., Grauer, R., and Schäfer, T. (2015). The instanton method and its numerical implementation in fluid mechanics. *Journal of Physics A Mathematical General*, 48(33):333001.

Grappin, R., Leorat, J., and Pouquet, A. (1983). Dependence of MHD turbulence spectra on the velocity field-magnetic field correlation. *A&A*, 126:51–58.

Grappin, R., Mangeney, A., and Marsch, E. (1990). On the origin of solar wind MHD turbulence - HELIOS data revisited. *J. Geophys. Res.*, 95:8197–8209.

Grappin, R., Müller, W.-C., and Verdini, A. (2016). Alfvén-dynamo balance and magnetic excess in magnetohydrodynamic turbulence. *A&A*, 589:A131.

Greco, A., Matthaeus, W. H., D'Amicis, R., Servidio, S., and Dmitruk, P. (2012). Evidence for Nonlinear Development of Magnetohydrodynamic Scale Intermittency in the Inner Heliosphere. *ApJ*, 749:105.

Greco, A., Matthaeus, W. H., Perri, S., Osman, K. T., Servidio, S., Wan, M., and Dmitruk, P. (2018). Partial Variance of Increments Method in Solar Wind Observations and Plasma Simulations. *Space Sci. Rev.*, 214(1):1.

Greco, A., Matthaeus, W. H., Servidio, S., Chuychai, P., and Dmitruk, P. (2009). Statistical Analysis of Discontinuities in Solar Wind ACE Data and Comparison with Intermittent MHD Turbulence. *ApJ*, 691:L111–L114.

Greco, A., Perri, S., Servidio, S., Yordanova, E., and Veltri, P. (2016). The Complex Structure of Magnetic Field Discontinuities in the Turbulent Solar Wind. *ApJ*, 823:L39.

Greco, A., Servidio, S., Matthaeus, W. H., and Dmitruk, P. (2010). Intermittent structures and magnetic discontinuities on small scales in MHD simulations and solar wind. *Planet. Space Sci.*, 58:1895–1899.

Hada, T., Koga, D., and Yamamoto, E. (2003). Phase coherence of MHD waves in the solar wind. *Space Sci. Rev.*, 107:463–466.

Haynes, C. T., Burgess, D., Camporeale, E., and Sundberg, T. (2015). Electron vortex magnetic holes: A nonlinear coherent plasma structure. *Physics of Plasmas*, 22(1):012309.

Hellinger, P., Trávníček, P., Kasper, J. C., and Lazarus, A. J. (2006). Solar wind proton temperature anisotropy: Linear theory and WIND/SWE observations. *Geophys. Res. Lett.*, 33:L09101.

Hellinger, P., TráVníček, P. M., Štverák, Š., Matteini, L., and Velli, M. (2013). Proton thermal energetics in the solar wind: Helios reloaded. *Journal of Geophysical Research (Space Physics)*, 118(4):1351–1365.

Hellinger, P., Verdini, A., Landi, S., Franci, L., and Matteini, L. (2018). von Kármán-Howarth equation for Hall magnetohydrodynamics: Hybrid simulations. *Astrophys. J. Lett.*, 857.

Horbury, T. S., Burgess, D., Fränz, M., and Owen, C. J. (2001). Three spacecraft observations of solar wind discontinuities. *Geophys. Res. Lett.*, 28(4):677–680.

Horbury, T. S., Forman, M., and Oughton, S. (2008). Anisotropic Scaling of Magneto-hydrodynamic Turbulence. *Phys. Rev. Lett.*, 101(17):175005–+.

Horbury, T. S., Forman, M. A., and Oughton, S. (2005). Spacecraft observations of solar wind turbulence: an overview. *Plasma Phys. Controlled Fusion*, 47:B703–B717.

Howes, G. G., Bale, S. D., Klein, K. G., Chen, C. H. K., Salem, C. S., and TenBarge, J. M. (2012). The Slow-mode Nature of Compressible Wave Power in Solar Wind Turbulence. *ApJ*, 753(1):L19.

Howes, G. G., Cowley, S. C., Dorland, W., Hammett, G. W., Quataert, E., and Schekochihin, A. A. (2006). Astrophysical Gyrokinetics: Basic Equations and Linear Theory. *ApJ*, 651:590–614.

Howes, G. G., Cowley, S. C., Dorland, W., Hammett, G. W., Quataert, E., and Schekochihin, A. A. (2008a). A model of turbulence in magnetized plasmas: Implications for the dissipation range in the solar wind. *Journal of Geophysical Research (Space Physics)*, 113(A5):A05103.

Howes, G. G., Dorland, W., Cowley, S. C., Hammett, G. W., Quataert, E., Schekochihin, A. A., and Tatsuno, T. (2008b). Kinetic Simulations of Magnetized Turbulence in Astrophysical Plasmas. *Phys. Rev. Lett.*, 100(6):065004–+.

Howes, G. G., Tenbarge, J. M., and Dorland, W. (2011). A weakened cascade model for turbulence in astrophysical plasmas. *Physics of Plasmas*, 18(10):102305.

Huang, S. Y., Sahraoui, F., Yuan, Z. G., He, J. S., Zhao, J. S., Le Contel, O., Deng, X. H., Zhou, M., Fu, H. S., Shi, Q. Q., Lavraud, B., Pang, Y., Yang, J., Wang, D. D., Li, H. M., Yu, X. D., Pollock, C. J., Giles, B. L., Torbert, R. B., Russell, C. T., Goodrich, K. A., Gershman, D. J., Moore, T. E., Ergun, R. E., Khotyaintsev, Y. V., Lindqvist, P.-A., Strangeway, R. J., Magnes, W., Bromund, K., Leinweber, H., Plaschke, F., Anderson, B. J., and Burch, J. L. (2017). Magnetospheric Multiscale Observations of Electron Vortex Magnetic Hole in the Turbulent Magnetosheath Plasma. *ApJ*, 836:L27.

Issautier, K., Mangeney, A., and Alexandrova, O. (2010). Spectrum of the electron density fluctuations: preliminary results from Ulysses observations. In Maksimovic, M., Issautier, K., Meyer-Vernet, N., Moncuquet, M., and Pantellini, F., editors, *Twelfth International Solar Wind Conference*, volume 1216 of *American Institute of Physics Conference Series*, pages 148–151.

Jagarlamudi, V. K., de Wit, T. D., Krasnoselskikh, V., and Maksimovic, M. (2019). Inherentness of non-stationarity in solar wind. *The Astrophysical Journal*, 871(1):68.

Jian, L. K., Russell, C. T., Luhmann, J. G., Strangeway, R. J., Leisner, J. S., and Galvin, A. B. (2009). Ion Cyclotron Waves in the Solar Wind Observed by STEREO Near 1 AU. *ApJ*, 701(2):L105–L109.

Jian, L. K., Wei, H. Y., Russell, C. T., Luhmann, J. G., Klecker, B., Omidi, N., Isenberg, P. A., Goldstein, M. L., Figueroa-Viñas, A., and Blanco-Cano, X. (2014). Electromagnetic Waves near the Proton Cyclotron Frequency: STEREO Observations. *Astrophys. J.*, 786(2):123.

Jovanović, D., Alexandrova, O., and Maksimović, M. (2015). Theory of coherent electron-scale magnetic structures in space plasma turbulence. *Phys. Scr*, 90(8):088002.

Jovanovic, D., Alexandrova, O., Maksimovic, M., and Belic, M. (2020). Fluid theory of coherent magnetic vortices in high-beta space plasmas. *accepted for publication in APJ*, page arXiv:1705.02913.

Kadomtsev, B. B. and Pogutse, O. P. (1974). Nonlinear helical perturbations of a plasma in the tokamak. *Zhurnal Eksperimental noi i Teoreticheskoi Fiziki*, 65:575–589.

Kajdič, P., Alexandrova, O., Maksimovic, M., Lacombe, C., and Fazakerley, A. N. (2016). Suprathermal Electron Strahl Widths in the Presence of Narrow-band Whistler Waves in the Solar Wind. *ApJ*, 833(2):172.

Kiyani, K. H., Chapman, S. C., Khotyaintsev, Y. V., Dunlop, M. W., and Sahraoui, F. (2009). Global Scale-Invariant Dissipation in Collisionless Plasma Turbulence. *Phys. Rev. Lett.*, 103(7):075006–+.

Kiyani, K. H., Chapman, S. C., Sahraoui, F., Hnat, B., Fauvarque, O., and Khotyaintsev, Y. V. (2013). Enhanced Magnetic Compressibility and Isotropic Scale Invariance at Sub-ion Larmor Scales in Solar Wind Turbulence. *ApJ*, 763:10.

Kiyani, K. H., Osman, K. T., and Chapman, S. C. (2015). Dissipation and heating in solar wind turbulence: from the macro to the micro and back again. *Philosophical Transactions of the Royal Society of London Series A*, 373(2041):20140155–20140155.

Knetter, T., Neubauer, F. M., Horbury, T., and Balogh, A. (2004). Four-point discontinuity observations using Cluster magnetic field data: A statistical survey. *Journal of Geophysical Research (Space Physics)*, 109(A6):A06102.

Koga, D. and Hada, T. (2003). Phase coherence of foreshock MHD waves: wavelet analysis. *Space Sci. Rev.*, 107:495–498.

Kolmogorov, A. (1941). The Local Structure of Turbulence in Incompressible Viscous Fluid for Very Large Reynolds' Numbers. *Akademiia Nauk SSSR Doklady*, 30:301–305.

Krishna Jagarlamudi, V. (2019). *Solar wind turbulence studies from 0.3 to 1 AU : HELIOS and WIND Observations*. PhD thesis, EMSTU, University of Orleans, Orleans.

Krishna Jagarlamudi, V., Alexandrova, O., Berčič, L., Dudok de Wit, T., Krasnoselskikh, V., Maksimovic, M., and Štverák, c. (2020). Whistler waves and electron properties in the inner heliosphere: Helios Observations. *The Astrophysical Journal*, 897(2).

Kuzzay, D., Alexandrova, O., and Matteini, L. (2019). Local approach to the study of energy transfers in incompressible magnetohydrodynamic turbulence. *Phys. Rev. E*, 99(5):053202.

Lacombe, C., Alexandrova, O., and Matteini, L. (2017). Anisotropies of the Magnetic Field Fluctuations at Kinetic Scales in the Solar Wind: Cluster Observations. *ApJ*, 848:45.

Lacombe, C., Alexandrova, O., Matteini, L., Santolík, O., Cornilleau-Wehrlin, N., Mangeney, A., de Conchy, Y., and Maksimovic, M. (2014). Whistler Mode Waves and the Electron Heat Flux in the Solar Wind: Cluster Observations. *ApJ*, 796:5.

Lacombe, C., Samsonov, A. A., Mangeney, A., Maksimovic, M., Cornilleau-Wehrlin, N., Harvey, C. C., Bosqued, J. M., and Trávníček, P. (2006). Cluster observations in the magnetosheath - Part 2: Intensity of the turbulence at electron scales. *Annales Geophysicae*, 24(12):3523–3531.

Lamb, H. (1895). *Hydrodynamics*. Cambridge: Cambridge Univ. Press, 2nd ed.

Lamb, H. (1906). *Hydrodynamics*. Cambridge: Cambridge Univ. Press, 3rd ed.

Leamon, R. J., Matthaeus, W. H., Smith, C. W., and Wong, H. K. (1998a). Contribution of Cyclotron-resonant Damping to Kinetic Dissipation of Interplanetary Turbulence. *ApJ*, 507:L181–L184.

Leamon, R. J., Smith, C. W., Ness, N. F., Matthaeus, W. H., and Wong, H. K. (1998b). Observational constraints on the dynamics of the interplanetary magnetic field dissipation range. *J. Geophys. Res.*, 103:4775–+.

Lion, S. (2016). *Multi-spacecraft and multi-scale analysis of solar wind turbulence*. Theses, Université Pierre et Marie Curie - Paris VI.

Lion, S., Alexandrova, O., and Zaslavsky, A. (2016). Coherent Events and Spectral Shape at Ion Kinetic Scales in the Fast Solar Wind Turbulence. *ApJ*, 824:47.

Loureiro, N. F. and Boldyrev, S. (2017). Collisionless reconnection in magnetohydrodynamic and kinetic turbulence. *The Astrophysical Journal*, 850(2):182.

Maksimovic, M. (2007). *On the Existence of Non-maxwellian Velocity Distribution Functions in the Corona and their Consequences for the Solar Wind Acceleration*, volume 725, page 191. Springer-Verlag Berlin Heidelberg.

Maksimovic, M., Zouganelis, I., Chaufray, J. Y., Issautier, K., Scime, E. E., Littleton, J. E., Marsch, E., McComas, D. J., Salem, C., Lin, R. P., and Elliott, H. (2005). Radial evolution of the electron distribution functions in the fast solar wind between 0.3 and 1.5 AU. *Journal of Geophysical Research (Space Physics)*, 110(A9):A09104.

Mallet, A., Schekochihin, A. A., and Chand ran, B. D. G. (2017). Disruption of Alfvénic turbulence by magnetic reconnection in a collisionless plasma. *Journal of Plasma Physics*, 83(6):905830609.

Mangeney, A., Lacombe, C., Maksimovic, M., Samsonov, A. A., Cornilleau-Wehrlin, N., Harvey, C. C., Bosqued, J.-M., and Trávníček, P. (2006). Cluster observations in the magnetosheath - Part 1: Anisotropies of the wave vector distribution of the turbulence at electron scales. *An.Geo.*, 24:3507–3521.

Mangeney, A., Salem, C., Veltri, P. L., and Cecconi, B. (2001). Intermittency in the solar wind turbulence and the haar wavelet transform. In B. Warmbein, editor, *Sheffield Space Plasma Meeting: Multipoint Measurements versus Theory*, volume 492 of *ESA Special Pub.*, page 53.

Marino, R., Sorriso-Valvo, L., Carbone, V., Noullez, A., Bruno, R., and Bavassano, B. (2008). Heating the Solar Wind by a Magnetohydrodynamic Turbulent Energy Cascade. *ApJ*, 677:L71–L74.

Markovskii, S. A., Vasquez, B. J., and Smith, C. W. (2008). Statistical Analysis of the High-Frequency Spectral Break of the Solar Wind Turbulence at 1 AU. *ApJ*, 675:1576–1583.

Matteini, L., Alexandrova, O., Chen, C. H. K., and Lacombe, C. (2017). Electric and magnetic spectra from MHD to electron scales in the magnetosheath. *MNRAS*, 466:945–951.

Matteini, L., Franci, L., Alexandrova, O., Lacombe, C., Landi, S., Hellinger, P., Papini, E., and Verdini, A. (2020). Magnetic field turbulence in the solar wind at sub-ion scales: in situ observations and numerical simulations. *arXiv e-prints*, page arXiv:2008.13219.

Matteini, L., Landi, S., Hellinger, P., Pantellini, F., Maksimovic, M., Velli, M., Goldstein, B. E., and Marsch, E. (2007). Evolution of the solar wind proton temperature anisotropy from 0.3 to 2.5 AU. *Geophys. Res. Lett.*, 34:20105–+.

Matteini, L., Stansby, D., Horbury, T. S., and Chen, C. H. K. (2018). On the 1/f Spectrum in the Solar Wind and Its Connection with Magnetic Compressibility. *ApJ*, 869(2):L32.

Matthaeus, W. H., Servidio, S., and Dmitruk, P. (2008). Comment on "Kinetic Simulations of Magnetized Turbulence in Astrophysical Plasmas". *Phys. Rev. Lett.*, 101(14):149501–+.

Matthaeus, W. H., Servidio, S., and Dmitruk, P. (2010). Dispersive Effects of Hall Electric Field in Turbulence. In Maksimovic, M., Issautier, K., Meyer-Vernet, N., Moncuquet, M., and Pantellini, F., editors, *Twelfth International Solar Wind Conference*, volume 1216 of *American Institute of Physics Conference Series*, pages 184–187.

Matthaeus, W. H. and Velli, M. (2011). Who Needs Turbulence?. A Review of Turbulence Effects in the Heliosphere and on the Fundamental Process of Reconnection. *Space Sci. Rev.*, 160:145–168.

Meyrand, R. and Galtier, S. (2013). Anomalous $k_\perp^{-8/3}$ Spectrum in Electron Magnetohydrodynamic Turbulence. *Phys. Rev. Lett.*, 111(26):264501.

Neubauer, F. M. (1980). Nonlinear standing Alfvén wave current system at Io: Theory. *J. Geophys. Res.*, 85(A3):1171–1178.

Neugebauer, M. (2006). Comment on the abundances of rotational and tangential discontinuities in the solar wind. *Journal of Geophysical Research (Space Physics)*, 111(A4):A04103.

Osman, K. T., Matthaeus, W. H., Greco, A., and Servidio, S. (2011). Evidence for Inhomogeneous Heating in the Solar Wind. *ApJ*, 727(1):L11.

Papini, E., Franci, L., Landi, S., Verdini, A., Matteini, L., and Hellinger, P. (2019). Can Hall magnetohydrodynamics explain plasma turbulence at sub-ion scales? *Astrophys. J.*, 870.

Parashar, T. N., Matthaeus, W. H., and Shay, M. A. (2018). Dependence of Kinetic Plasma Turbulence on Plasma β. *Astrophys. J. Lett.*, 864.

Parker, E. N. (1958). Dynamics of the Interplanetary Gas and Magnetic Fields. *ApJ*, 128:664–+.

Passot, T. and Sulem, P. L. (2015). A Model for the Non-universal Power Law of the Solar Wind Sub-ion-scale Magnetic Spectrum. *ApJ*, 812(2):L37.

Perri, S., Goldstein, M. L., Dorelli, J. C., and Sahraoui, F. (2012a). Detection of Small-Scale Structures in the Dissipation Regime of Solar-Wind Turbulence. *Physical Review Letters*, 109(19):191101.

Perri, S., Goldstein, M. L., Dorelli, J. C., and Sahraoui, F. (2012b). Detection of Small-Scale Structures in the Dissipation Regime of Solar-Wind Turbulence. *Physical Review Letters*, 109(19):191101.

Perrone, D., Alexandrova, O., Mangeney, A., Maksimovic, M., Lacombe, C., Rakoto, V., Kasper, J. C., and Jovanovic, D. (2016). Compressive Coherent Structures at Ion Scales in the Slow Solar Wind. *ApJ*, 826:196.

Perrone, D., Alexandrova, O., Roberts, O., Lion, S., Lacombe, C., Walsh, A., Maksimovic, M., and Zouganelis, I. (2017). Coherent Structures at Ion Scales in Fast Solar Wind: Cluster observations. *submitted to APJ*.

Perrone, D., Stansby, D., Horbury, T. S., and Matteini, L. (2019a). Radial evolution of the solar wind in pure high-speed streams: HELIOS revised observations. *MNRAS*, 483(3):3730–3737.

Perrone, D., Stansby, D., Horbury, T. S., and Matteini, L. (2019b). Thermodynamics of pure fast solar wind: radial evolution of the temperature-speed relationship in the inner heliosphere. *MNRAS*, 488(2):2380–2386.

Petviashvili, V. I. and Pokhotelov, O. A. (1992). *Solitary Waves in Plasmas and in the Atmosphere*. Gordon & Breach Science Pub.

Podesta, J. J., Roberts, D. A., and Goldstein, M. L. (2006). Power spectrum of small-scale turbulent velocity fluctuations in the solar wind. *J. Geophys. Res.*, 111(A10):10109–+.

Retinò, A., Sundkvist, D., Vaivads, A., Mozer, F., André, M., and Owen, C. J. (2007). In situ evidence of magnetic reconnection in turbulent plasma. *Nature Physics*, 3(4):236–238.

Rezeau, L., Roux, A., and Russell, C. T. (1993). Characterization of small-scale structures at the magnetopause from ISEE measurements. *J. Geophys. Res.*, 98(.17):179–186.

Roberts, O. W., Alexandrova, O., Kajdič, P., Turc, L., Perrone, D., Escoubet, C. P., and Walsh, A. (2017). Variability of the Magnetic Field Power Spectrum in the Solar Wind at Electron Scales. *ApJ*, 850:120.

Roberts, O. W., Li, X., Alexandrova, O., and Li, B. (2016). Observation of an MHD Alfvén vortex in the slow solar wind. *Journal of Geophysical Research (Space Physics)*, 121:3870–3881.

Rudakov, L., Mithaiwala, M., Ganguli, G., and Crabtree, C. (2011). Linear and nonlinear Landau resonance of kinetic Alfvén waves: Consequences for electron distribution and wave spectrum in the solar wind. *Physics of plasmas*, 18(1):012307.

Sahraoui, F., Goldstein, M. L., Belmont, G., Canu, P., and Rezeau, L. (2010). Three Dimensional Anisotropic k Spectra of Turbulence at Subproton Scales in the Solar Wind. *Phys. Rev. Lett.*, 105:131101–+.

Sahraoui, F., Huang, S. Y., Belmont, G., Goldstein, M. L., Rétino, A., Robert, P., and De Patoul, J. (2013). Scaling of the Electron Dissipation Range of Solar Wind Turbulence. *ApJ*, 777:15.

Salem, C. (2000). *Ondes, turbulence et phenomenes dissipatifs dans le vent solaire a partir des observations de la sonde Wind*. PhD thesis. Thèse de doctorat dirigée par André Mangeney; Terre, océan, espace. Physique Paris 7 2000.

Salem, C., Mangeney, A., Bale, S. D., and Veltri, P. (2009). Solar Wind Magnetohydrodynamics Turbulence: Anomalous Scaling and Role of Intermittency. *ApJ*, 702:537–553.

Salem, C. S., Howes, G. G., Sundkvist, D., Bale, S. D., Chaston, C. C., Chen, C. H. K., and Mozer, F. S. (2012). Identification of Kinetic Alfvén Wave Turbulence in the Solar Wind. *ApJ*, 745:L9.

Saur, J., Neubauer, F. M., Connerney, J. E. P., Zarka, P., and Kivelson, M. G. (2004). *Plasma interaction of Io with its plasma torus*, volume 1, pages 537–560.

Schekochihin, A. A., Cowley, S. C., Dorland, W., Hammett, G. W., Howes, G. G., Quataert, E., and Tatsuno, T. (2009). Astrophysical Gyrokinetics: Kinetic and Fluid Turbulent Cascades in Magnetized Weakly Collisional Plasmas. *ApJS*, 182:310–377.

Schreiner, A. and Saur, J. (2017). A Model for Dissipation of Solar Wind Magnetic Turbulence by Kinetic Alfvén Waves at Electron Scales: Comparison with Observations. *ApJ*, 835:133.

Schwartz, S. J., Burgess, D., and Moses, J. J. (1996). Low-frequency waves in the Earth's magnetosheath: present status. *Annales Geophysicae*, 14(11):1134–1150.

Servidio, S., Carbone, V., Primavera, L., Veltri, P., and Stasiewicz, K. (2007). Compressible turbulence in Hall Magnetohydrodynamics. *Planet. Space Sci.*, 55:2239–2243.

Servidio, S., Matthaeus, W. H., Shay, M. A., Cassak, P. A., and Dmitruk, P. (2009). Magnetic Reconnection in Two-Dimensional Magnetohydrodynamic Turbulence. *Phys. Rev. Lett.*, 102(11):115003.

She, Z.-S., Jackson, E., and Orszag, S. A. (1990). Intermittent vortex structures in homogeneous isotropic turbulence. *Nature*, 344:226–228.

Smith, C. W., Hamilton, K., Vasquez, B. J., and Leamon, R. J. (2006). Dependence of the Dissipation Range Spectrum of Interplanetary Magnetic Fluctuationson the Rate of Energy Cascade. *ApJ*, 645:L85–L88.

Söding, A., Neubauer, F. M., Tsurutani, B. T., Ness, N. F., and Lepping, R. P. (2001). Radial and latitudinal dependencies of discontinuities in the solar wind between 0.3 and 19 AU and -80Å and +10Å. *Annales Geophysicae*, 19(7):681–686.

Sorriso-Valvo, L., Carbone, F., Perri, S., Greco, A., Marino, R., and Bruno, R. (2018a). On the Statistical Properties of Turbulent Energy Transfer Rate in the Inner Heliosphere. *Sol. Phys.*, 293(1):10.

Sorriso-Valvo, L., Carbone, V., Veltri, P., Consolini, G., and Bruno, R. (1999). Intermittency in the solar wind turbulence through probability distribution functions of fluctuations. *Geophys. Res. Lett.*, 26(13):1801–1804.

Sorriso-Valvo, L., Marino, R., Carbone, V., Noullez, A., Lepreti, F., Veltri, P., Bruno, R., Bavassano, B., and Pietropaolo, E. (2007). Observation of Inertial Energy Cascade in Interplanetary Space Plasma. *Physical Review Letters*, 99(11):115001.

Sorriso-Valvo, L., Perrone, D., Pezzi, O., Valentini, F., Servidio, S., Zouganelis, I., and Veltri, P. (2018b). Local energy transfer rate and kinetic processes: the fate of turbulent energy in two-dimensional hybrid Vlasov-Maxwell numerical simulations. *Journal of Plasma Physics*, 84(2):725840201.

Spangler, S. R. and Gwinn, C. R. (1990). Evidence for an inner scale to the density turbulence in the interstellar medium. *ApJ*, 353:L29–L32.

Stansby, D., Horbury, T. S., Chen, C. H. K., and Matteini, L. (2016). Experimental Determination of Whistler Wave Dispersion Relation in the Solar Wind. *ApJ*, 829(1):L16.

Stawarz, J. E., Eriksson, S., Wilder, F. D., Ergun, R. E., Schwartz, S. J., Pouquet, A., Burch, J. L., Giles, B. L., Khotyaintsev, Y., Le Contel, O., Lindqvist, P. A., Magnes, W., Pollock, C. J., Russell, C. T., Strangeway, R. J., Torbert, R. B., Avanov, L. A., Dorelli, J. C., Eastwood, J. P., Gershman, D. J., Goodrich, K. A., Malaspina, D. M., Marklund, G. T., Mirioni, L., and Sturner, A. P. (2016). Observations of turbulence in a Kelvin-Helmholtz event on 8 September 2015 by the Magnetospheric Multiscale mission. *Journal of Geophysical Research (Space Physics)*, 121(11):11,021–11,034.

Stawicki, O., Gary, S. P., and Li, H. (2001). Solar wind magnetic fluctuation spectra: Dispersion versus damping. *J. Geophys. Res.*, 106:8273–8282.

Strauss, H. R. (1976). Nonlinear, three-dimensional magnetohydrodynamics of noncircular tokamaks. *Physics of Fluids*, 19:134–140.

Štverák, Š., Trávníček, P., Maksimovic, M., Marsch, E., Fazakerley, A., and Scime, E. E. (2008). Electron temperature anisotropy constraints in the solar wind. *J. Geophys. Res.*, 113.

Sundberg, T., Burgess, D., and Haynes, C. T. (2015). Properties and origin of subproton-scale magnetic holes in the terrestrial plasma sheet. *Journal of Geophysical Research (Space Physics)*, 120:2600–2615.

Sundkvist, D., Retinò, A., Vaivads, A., and Bale, S. D. (2007). Dissipation in Turbulent Plasma due to Reconnection in Thin Current Sheets. *Phys. Rev. Lett.*, 99(2):025004.

Tong, Y., Vasko, I. Y., Artemyev, A. V., Bale, S. D., and Mozer, F. S. (2019a). Statistical Study of Whistler Waves in the Solar Wind at 1 au. *ApJ*, 878(1):41.

Tong, Y., Vasko, I. Y., Pulupa, M., Mozer, F. S., Bale, S. D., Artemyev, A. V., and Krasnoselskikh, V. (2019b). Whistler Wave Generation by Halo Electrons in the Solar Wind. *ApJ*, 870(1):L6.

Torrence, C. and Compo, G. P. (1998). A Practical Guide to Wavelet Analysis. *Bulletin of the American Meteorological Society*, 79:61–78.

Totten, T. L., Freeman, J. W., and Arya, S. (1995). An empirical determination of the polytropic index for the free-streaming solar wind using Helios 1 data. *J. Geophys. Res.*, 100(A1):13–18.

Tsurutani, B. T., Arballo, J. K., Mok, J., Smith, E. J., Mason, G. M., and Tan, L. C. (1994). Electromagnetic waves with frequencies near the local proton gyrofrequency: ISEE-3 1 AU observations. *Geophys. Res. Lett.*, 21(7):633–636.

Tsurutani, B. T., Lakhina, G. S., Verkhoglyadova, O. P., Echer, E., and Guarnieri, F. o. L. (2007). Comment on "Comment on the abundances of rotational and tangential discontinuities in the solar wind" by M. Neugebauer. *Journal of Geophysical Research (Space Physics)*, 112(A3):A03101.

Tsurutani, B. T., Lakhina, G. S., Verkhoglyadova, O. P., Echer, E., Guarnieri, F. o. L., Narita, Y., and Constantinescu, D. O. (2011a). Magnetosheath and heliosheath mirror mode structures, interplanetary magnetic decreases, and linear magnetic decreases: Differences and distinguishing features. *Journal of Geophysical Research (Space Physics)*, 116(A2):A02103.

Tsurutani, B. T., Lakhina, G. S., Verkhoglyadova, O. P., Gonzalez, W. D., Echer, E., and Guarnieri, F. L. (2011b). A review of interplanetary discontinuities and their geomagnetic effects. *Journal of Atmospheric and Solar-Terrestrial Physics*, 73(1):5–19.

Tu, C.-Y. and Marsch, E. (1995). MHD structures, waves and turbulence in the solar wind: Observations and theories. *Space Sci. Rev.*, 73:1–2.

Šafránková, J., Němeček, Z., Přech, L., and Zastenker, G. N. (2013). Ion Kinetic Scale in the Solar Wind Observed. *Phys. Rev. Lett.*, 110(2):025004.

Vasquez, B. J. and Hollweg, J. V. (1996). Formation of arc-shaped Alfvén waves and rotational discontinuities from oblique linearly polarized wave trains. *J. Geophys. Res.*, 101(A6):13527–13540.

Vasquez, B. J. and Hollweg, J. V. (2001). Evolution and dissipation of imbedded rotational discontinuities and Alfvén waves in nonuniform plasma and the resultant proton heating. *J. Geophys. Res.*, 106(A4):5661–5682.

Velli, M. (2003). MHD turbulence and the heating of astrophysical plasmas. *Plasma Physics and Controlled Fusion*, 45(12A):A205–A216.

Veltri, P. (1994). Low frequency turbulence and energy dissipation in the Solar Wind. *Space Sci. Rev.*, 68(1-4):63–74.

Veltri, P. (1999). MHD turbulence in the solar wind: self-similarity, intermittency and coherent structures. *Plasma Physics and Controlled Fusion*, 41:787.

Veltri, P. and Mangeney, A. (1999). Scaling laws and intermittent structures in solar wind mhd turbulence. In Habbal, S. R., Esser, R., Hollweg, J. V., and Isenberg, P. A., editors, *Solar Wind Nine*, volume 471 of *American Institute of Physics Conference Series*, page 543.

Verdini, A., Grappin, R., Alexandrova, O., Franci, L., Landi, S., Matteini, L., and Papini, E. (2019). Three-dimensional local anisotropy of velocity fluctuations in the solar wind. *MNRAS*, 486(3):3006–3018.

Verdini, A., Grappin, R., Alexandrova, O., and Lion, S. (2018). 3D Anisotropy of Solar Wind Turbulence, Tubes, or Ribbons? *ApJ*, 853:85.

Verdini, A., Grappin, R., Pinto, R., and Velli, M. (2012). On the Origin of the 1/f Spectrum in the Solar Wind Magnetic Field. *ApJ*, 750:L33.

Verkhoglyadova, O. P., Dasgupta, B., and Tsurutani, B. T. (2003). Model for vortex turbulence with discontinuities in the solar wind. *Nonlinear Processes in Geophysics*, 10:335–343.

von Papen, M., Saur, J., and Alexandrova, O. (2014). Turbulent magnetic field fluctuations in Saturn's magnetosphere. *Journal of Geophysical Research (Space Physics)*, 119:2797–2818.

Štverák, Š., Maksimovic, M., Trávníček, P. M., Marsch, E., Fazakerley, A. N., and Scime, E. E. (2009). Radial evolution of nonthermal electron populations in the low-latitude solar wind: Helios, Cluster, and Ulysses Observations. *Journal of Geophysical Research (Space Physics)*, 114(A5):A05104.

Štverák, Š., Trávníček, P., Maksimovic, M., Marsch, E., Fazakerley, A. N., and Scime, E. E. (2008). Electron temperature anisotropy constraints in the solar wind. *Journal of Geophysical Research (Space Physics)*, 113(A3):A03103.

Wang, T., Alexandrova, O., Perrone, D., Dunlop, M., Dong, X., Bingham, R., Khotyaintsev, Y. V., Russell, C. T., Giles, B. L., Torbert, R. B., Ergun, R. E., and Burch, J. L. (2019). Magnetospheric Multiscale Observation of Kinetic Signatures in the Alfvén Vortex. *ApJ*, 871(2):L22.

Wicks, R. T., Horbury, T. S., Chen, C. H. K., and Schekochihin, A. A. (2010). Power and spectral index anisotropy of the entire inertial range of turbulence in the fast solar wind. *MNRAS*, 407:L31–L35.

Wicks, R. T., Horbury, T. S., Chen, C. H. K., and Schekochihin, A. A. (2011). Anisotropy of imbalanced alfvénic turbulence in fast solar wind. *Phys. Rev. Lett.*, 106:045001.

Yang, Y., Wan, M., Matthaeus, W. H., Sorriso-Valvo, L., Parashar, T. N., Lu, Q., Shi, Y., and Chen, S. (2019). Scale dependence of energy transfer in turbulent plasma. *MNRAS*, 482(4):4933–4940.